The Baltic Sea Tracer Release Experiment
Mixing processes in the Gotland Basin

Dissertation
zur Erlangung des akademischen Grades
doctor rerum naturalium (Dr. rer. nat.)
der Mathematisch-Naturwissenschaftlichen Fakultät
der Universität Rostock

vorgelegt von
Peter Ludwig Holtermann
geb. am 10. September 1980 in Bremen
Rostock, 12. August 2011

urn:nbn:de:gbv:28-diss2012-0087-1

Gutachter/Reviewers:

Prof. Dr. Hans Burchard
Leibniz Institute for Baltic Sea Research Warnemünde, Germany

Prof. Dr. Anders Stigebrandt
University of Gothenborg, Sweden

Datum der Einreichung/Submission date: 12.08.2011
Datum der Verteidigung/Defence date: 09.03.2012

Abstract
Mixing processes in the deeper Gotland Basin were measured and analysed using the inert tracer CF_3SF_5, microstructure profiles as well as five permanent moorings yielding two years of in situ data. The tracer spreading showed that mixing rates in the deeper Gotland Basin are dominated by boundary mixing processes. The major mixing agent for the observed mixing rates is identified as sub-inertial topographic waves that are resonantly coupled to wind events. They thus explain the fast response of mixing rates to wind events, as it was observed from the mooring data. Internal mixing processes have a minor contribution to the basin-scale mixing rate.

Zusammenfassung
Die Vermischungsprozesse im tiefen Gotlandbecken wurden mit Hilfe des inerten Tracers CF_3SF_5, Mikrostrukturprofilen sowie von 5 Verankerungen über einen Zeitraum von etwa zwei Jahren untersucht. Die vertikale Ausbreitung des Tracers zeigt, dass die beckenweite Vermischung durch Randmischungsprozesse dominiert ist und interne Vermischung eine eher untergeordnete Rolle spielt. Die Verankerungsdaten zeigen, dass ein Großteil für die Mischung notwendige Energie durch sub-inertiale topographische Wellen geliefert wird und somit eine direkte Kopplung zwischen Windereignissen und Tiefenwasservermischung besteht.

Contents

1. Acknowledgements

The work of this thesis would not have been possible without the help, and the numerous different kinds of contributions, I was given. I would therefore like to thank all the people who supported me along the way. I especially thank Lars Umlauf, who supervised my work, and all his time for my weird and not so weird theories about vertical mixing and the underlying processes in the Gotland Basin as well as for his great ideas and hints to analyse the BaTRE dataset. In addition to Lars, I also want to thank Hans Burchard for his long-term support of both my master thesis and this PhD. Lars and Hans always supported and encouraged me to publish the work done, to attend international conferences as well as summer schools. I really appreciate their concept of and enthusiasm for student supervision and science in general. I would furthermore like to thank Charitha Pattiaratchi who organised, together with Hans Burchard, my one year long stay at the University of Western Australia in Perth, Australia and gave me the opportunity to attend field work in several marine systems along the coast of western and north-western Australia. I enjoyed working as a part of the BaTRE group and I thereby got an impression of tracer release experiments and marine science in the "deep blue ocean". This was mainly due to the communication with Toste Tanhua from the Leibniz Institute of Marine Sciences in Kiel. The whole BaTRE project depended on the accurate measurement of CF_3SF_5. This technically challenging task was done by the chemistry department of the IOW and I like to thank Oliver Schmale, Gregor Rehder, Joanna Waniek and Susanne Lage for the good collaboration. I also enjoyed the discussions with Jim Ledwell and like to thank him for giving us hints for the tracer analysis. I do especially like to thank Eefke van der Lee for correcting and improving the english of this work. I also like to thank Eberhard Hagen for the long-term mooring data of the NE mooring and Falk Pollehne for the C2 mooring data as well as Klaus Jürgens for ship time to recover the SW mooring. This work was funded by the German Research Foundation (DFG) under grants UM 79/3-1 and UM 79/4-1.

2. Introduction

2.1. Motivation

It is certainly justified to ask why one would want to study turbulent mixing and dispersion in the ocean and especially in the Baltic Sea. There are, of course, numerous good answers to that question. I choose to show a photograph depicting an ecological phenomenon in the Baltic Sea, which occurs, last but not least, due to turbulent mixing processes: Cyanobacterial blooms that emerge at irregular intervals during the early summer months, e.g. in July 2005 as shown in Fig. 2.1. These blooms, which dominate the whole central Baltic Sea, exist due to a process-chain of vertical mixing processes. It starts with the external forcing from the wind and ends in small turbulent billows with a size of 1 cm, which mix deeper nutrient-rich (especially phosphate-rich) water into the nutrient-poor, euphotic zone of the Baltic Sea. As a result of the mixing the surface water has a ratio of nitrogen (N) to phosphate (P), which is lower than the demand of phytoplankton (defined by the Redfield ratio of N:P=16:1). After the spring bloom and the depletion of dissolved nitrogen, an excess of phosphate remains in the euphotic zone. This phosphate is the basis of the atmospheric nitrogen fixating cyanobacteria which can cause under certain conditions summer blooms as shown in Fig. 2.1. The budget of the phosphate in the surface mixed layer is a balance between the uptake by autotrophic organisms, vertical transport and remineralisation of organic matter. The vertical transport into the mixed layer is via turbulent entrainment processes whereas the transport out of the mixed layer is mainly in the form of particulate matter. After the blooms the dead cyanobacteria sink as particulate organic matter into the deeper parts where they are remineralised. The demand for oxygen for the remineralisation is higher than the vertical transport of oxygen into deeper parts leading to a depletion of oxygen and finally to anoxic deep-water conditions (*Nausch et al.*, 2003; *Reissmann et al.*, 2009). The anoxic deep water favours an increase of phosphate concentrations by reducing iron-III-hydroxophosphate at the sediment surface by hydrogen sulphide into phosphate and iron(II) ions (Chap. 4.2.2). The increase of phosphate concentrations in the deep water and the subsequent turbulent mixing into the surface water completes the "vicious-circle". This self-sustaining cycle, the surface scum of the cyanobacterial bloom, their toxicity and the large input of nitrogen from the atmosphere into the water make the cyanobacteria important for the ecosystem and for society (*Vahtera et al.*, 2007). To understand the timing and the probability of these blooms, as well as the reaction of the Baltic Sea ecosystem to a change of the climate, is therefore directly related to the understanding of mixing processes and is one of our motivations to study mixing in the Baltic Sea.

2.2. The ocean

Leaving the Baltic Sea and looking at turbulent mixing from a global perspective, one arrives instantaneously at the work of *Munk* (1966). *Munk* assumed a balance between advection and diffusion of the ocean:

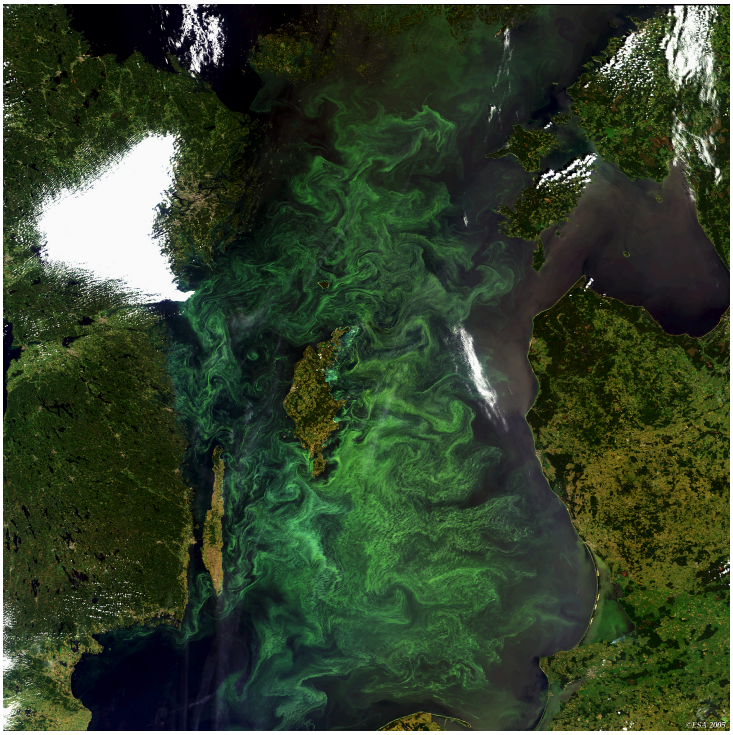

Figure 2.1.: Medium Resolution Imaging Spectrometer (MERIS), acquired on 13 July 2005 over the Baltic Sea, showing a large cyanobacterial bloom (green colour visible in centre image). Source ESA (2005), used with permission.

$$w\frac{\partial T}{\partial z} = \kappa\frac{\partial^2 T}{\partial z^2}\,, \tag{2.1}$$

where w is the vertical velocity, T the temperature and κ a turbulent diffusivity. The idea of the steady solution comes from the fact that dense water is formed near the poles, is advected into the deep ocean and in the direction of the equator where it then advects *upwards* at low and mid latitudes, tranporting cold water into intermediate depths of about 1500 m. From the approximation of deep water formation in the Antarctic of 25 Sv (25×10^6 m^3 s^{-1}, this estimate has been refined by *Munk and Wunsch* (1998) to 30 Sv) *Munk* estimated w to be 1.4×10^{-7} m s^{-1}. This implies that a renewal of the ocean with a mean depth of 4 km would take about 1000 years and "Without deep mixing the ocean would turn, within a few thousand years, into a stagnant pool of cold salty water with equilibrium maintained locally by near-surface mixing and with very weak convectively driven surface-intensified circulation" (*Munk and Wunsch*, 1998). Measurements show that the ocean is not a stagnant pool of cold water; warm water is mixed down considerably deeper than is possible by simple wind-induced turbulent mixing. The mean temperature profile in the Pacific Ocean has, for example, an approximately exponential decay of temperature with depth: $T = T_0 \exp(z/d)$ with the constant $d = 0.93$ km. Substituting the temperature profile into Eq. (2.1), T_0 can be choosen arbitrarily, gives $\kappa = wd$ and the average diffusivity of temperature in 1500 m depth is thus about 1.3×10^{-4} m^2 s^{-1} (the canonical value of ocean diffusivity). *Munk* (1966) verified this results using profiles of salinity and ^{14}C.

Since then numerous attempts to measure diffusivities and to find turbulent diffusivities

around the proposed canonical value have been made. A general conclusion of these experiments is that measured diffusivities are an order of magnitude below the canonical value for the interior ocean. A widely recognised experiment was the SF_6 injection in the eastern North Atlantic (*Ledwell et al.*, 1998). *Ledwell et al.* (1998) reports diffusivities between 1.2×10^{-5} and 1.7×10^{-5} m^2 s^{-1}. This means, that if the downwelling of the water is balanced by turbulent mixing, this mixing is not happening in the open ocean but must be located at mixing hot spots, such as at underwater mountains. Some evidence for enhanced mixing has been found over the rough topography in the Brazil Basin (*Ledwell et al.*, 2000). Another recent tracer release, the DIMES experiment showed that, turbulent dispersion in the Southern Ocean, a proposed mixing hot spot, is as well in the order of 1×10^{-5} m^2 s^{-1} ($0.07 - 1.3 \times 10^{-5}$ m^2 s^{-1}, *Ledwell et al.*, 2011). This, and former results, raised doubt about the ocean-scale canonical diffusivity. However, the question whether the diffusivity suggested by *Munk* (1966) is appropriate or whether the ocean is more adiabatically constrained than previously thought before remains unanswered. In the latter case the ocean-scale diffusivity would be more likely of the order of 1×10^{-5} m^2 s^{-1}.

Apart from the mixing rates deduced from the steady state solution, it is of special interest to understand the processes which lead to these basin-, or ocean-scale mixing rates. If the detailed processes of mixing would be known, the basin-scale mixing rate could be calculated by adding the contributions from all processes leading to mixing. Together with the ocean-scale diffusivity, *Munk* (1966) suggested several processes responsible for the observed mixing rates and supported internal wave breaking in the ocean interior as a likely process. *Armi* (1978) suggested that mixing occurs at the boundaries and that the well mixed-bottom boundary layers (BBL) detach and interleave into the ocean. Boundary mixing and the subsequent interleaving into the interior has been found as the dominant mechanism contributing to the basin-scale mixing rate in lakes (*Goudsmit et al.*, 1997) and ocean basins (*Ledwell and Hickey*, 1995; *Ledwell and Bratkovich*, 1995, and this thesis).

The observed abyssal ocean mixing rates require an energy input, which, for the ocean, comes from the tides and winds. The distribution between the wind-forced compared to the tidal-induced energy input is very similar: 1.2 TW (Tera Watt, 10^{12} W) supplied by wind and 0.9 TW due to tides (*Munk and Wunsch*, 1998). However, how this energy input cascades down to the smallest scales (the Kolmogorov scale is of the order of 1 cm and the time scale is a few seconds) where the molecular viscosity/diffusivity acts, is far from being understood thoroughly. It should also be noted that the uncertainties of the energy contributions are between factors of 2 and 10 (*Wunsch and Ferrari*, 2004).

The reason for these open questions is, last but not least, also the complexity of measuring turbulent mixing processes and the corresponding diffusivities. In the past, two main techniques have been widely used to derive the turbulent eddy diffusivities cited above: microstructure measurements of either velocity shear or temperature, as well as tracer dispersion measurements. Microstructure profilers measure the smallest scales of velocity shear/temperature and, with assumptions such as isotropic turbulence, the measured turbulence dissipation rates ε of turbulent kinetic energy can be derived. These dissipation rates can be used again to estimate the turbulent diffusivities. Tracer dispersion experiments are based on the release of a tracer and the subsequent observation of the change of the horizontal and vertical distribution over time. Nevertheless, both techniques are constrained by expensive ship time and it thus still holds that "In some regions, and in relation to some processes, knowledge of turbulence is as patchy as is turbulence itself in the stratified halocline" (*Thorpe*, 2005). There are recent advances in autonomous microstructure measurements, e.g. velocity shear probes attached to autonomous underwater gliders (*Thorpe et al.*, 2003; *Goodman et al.*, 2006), but this technique is still in its infancy and thus not yet widely used.

As seen above, wind energy contributes significantly to abyssal mixing and, from this point of view the Baltic Sea can be considered as an ideal laboratory for studying mixing processes without the influence of tides, since the shape of the Baltic Sea strongly damps tidal signals (*Reissmann et al.*, 2009). Mixing studies in the Baltic Sea can therefore concentrate first on wind-generated mixing and second on the contribution of boundary mixing processes compared with interior mixing, again without a tidal signal. These results can help to quantify mixing processes and to increase the accuracy of the quantification of the global energy budget required for mixing.

2.3. This thesis

Based on this background the Baltic Sea Tracer Release Experiment (BaTRE) project tries to shed some light on these questions. Since there are virtually no tides in the central Baltic Sea the search can be focussed on the wind-generated contribution to mixing. The concept of the project was based around the injection of the inert tracer CF_3SF_5, the observation of the spreading from the point injection to a basin filling concentration and the parallel measurement of turbulent mixing with velocity shear microstructure probes and several long term moorings deployed in the basin.

This thesis is based on BaTRE and is divided into the part introducing the tracer CF_3SF_5 used (Chap. 3.1), the theory of the microstructure measurements in Chap. 3.2, and the basin-scale budgets in Chap. 3.3. Internal waves and topographic waves, two processes, which are important for mixing in the Gotland Basin, are introduced in Chap. 3.4 and Chap. 3.5 respectively. An overview of the Baltic Sea and the Gotland Basin, the location of the injection, can be found in Chap. 4.1. So far the BaTRE results have been published in three articles: *Umlauf et al.* (2008), *Holtermann et al.* (2011) (Part I) and *Holtermann and Umlauf* (2011) (Part II) and the main results of this thesis are based on the results of Part I and Part II. The BaTRE project itself is introduced in Chap. 5.1 which is a culmination of the introductions of Part I and Part II. The design and the instrumentation of the project, including the available data, the timetables etc. are given in Chap. 5.2 and Chap. 5.3 and is a culmination of Part I and Part II. Chap. 5.4 reviews the hydrography of the Gotland Basin during the BaTRE project and is taken from Part II. The results seen from the tracer dispersion are in Chap. 6 and originate from Part I. Chap. 7 focusses on the processes responsible for the observed spreading (from Part II). A summary of the BaTRE project and an outlook based on the gained results are given in Chap. 8 and Chap. 9, respectively.

As mentioned above the results of the BaTRE project have been published in three articles and would not be possible in this form without the help and the contributions of the co-authors:

1. Umlauf, L., T. Tanhua, J. J. Waniek, O. Schmale, P. Holtermann, and G. Rehder (2008), Hunting a new tracer, *EOS, Transactions American Geophysical Union*, *89*(43), 419–419

gives a brief overview about the BaTRE project and is not part of this thesis. The two companion articles

2. *Holtermann et al.* (2011) (Part I): Holtermann, P., L. Umlauf, T. Tanhua, O. Schmale, G. Rehder, and J. Waniek (2011), The Baltic Sea Tracer Release Experiment. Part I. Mixing rates, *J. Geophys. Res.*, accepted

3. *Holtermann and Umlauf* (2011) (Part II): Holtermann, P., and L. Umlauf (2011), The Baltic Sea Tracer Release Experiment. Part II. Mixing processes, *J. Geophys. Res.*, submitted

are the basis of this thesis. The co-authors and their contributions to the publications are:

Hans Burchard Leibniz-Institute for Baltic Sea Research, Warnemünde, Germany (IOW), section physical oceanography. Initiation of the BaTRE project. Support and supervision of this thesis.

Lars Umlauf IOW, section physical oceanography. Text work and supervision of my data processing and analysis. Design of the BaTRE project. BaTRE project supervisor.

Toste Tanhua Leibniz-Institue for Marine Sciences, Kiel, Germany (IFM), section marine chemistry. CF_3SF_5 injection, sampling and measurement technology, main contributor to the tracer measurement section (Chap. 5.3.3). Revision of the submitted manuscript.

Oliver Schmale IOW, section marine chemistry. Design and building of the IOW technology for CF_3SF_5 measurement. Revision of the submitted manuscript.

Gregor Rehder IOW, section marine chemistry. CF_3SF_5 measurement. Design of the BaTRE project. Revision of the submitted manuscript.

Joanna Waniek IOW, section marine chemistry. Design of the BaTRE project. Revision of the submitted manuscript.

2.4. Notation

The symbols used in this thesis are explained at their first appearance. For vectors and matrices the index notation (Einstein notation) is used: The vector $\mathbf{x} = (x_1, x_2, x_3)$ has the components x_i where the index i is between 1 and 3. If an index appears twice in the same term it implies a sum over the index: $\partial u_i/\partial x_i = \partial u_1/\partial x_1 + \partial u_2/\partial x_2 + \partial u_3/\partial x_3$. The index α is between 1 and 2. Coordinates are such that the first two coordinates are generally oriented horizontally: $x_1 = x$, $x_2 = y$. $x_3 = z$ is oriented vertically and is positive in upward direction. Velocities u_i are also denoted as $u_1 = u$, $u_2 = v$, $u_3 = w$. In some cases indices are used differently, the definition is given at their appearance.

3. Measurement of mixing in the ocean and mixing processes

The term turbulence was used in the introduction but it has to be noted that it is not well defined. It is intuitively understood as irregular and unpredictable flow in billow-like structures as can be nicely seen in the satellite picture (Fig. 2.1). An important aspect of turbulence is its influence on mixing. This was shown with the tracer release experiment by Osborn Reynolds (*Reynolds*, 1883) who injected a streak of ink into a pipe with the diameter d in which water, with viscosity ν, was flowing with the speed U. "When the velocities were sufficiently low, the streak of colour extended in a beautiful straight line through the tube" (*Reynolds*, 1883) and has thus not been mixed very much with the surrounding water, Fig. 3.1a. If U increases and pushes the Reynolds number:

$$Re = \frac{Ud}{\nu}\,, \tag{3.1}$$

over the threshold of approximately 10000, the flow will develop eddies at a random point some distance from the intake. These eddies mix the ink over the full diameter of the tube (Fig. 3.1b), clearly showing the strong relation between mixing and turbulence. The physical process of mixing of a compound, may it be the momentum of the water, temperature or salinity, is due to diffusion. According to the Fickian Law, diffusion acts proportional to the gradient of the compound (e.g. salinity) $\partial S/\partial x_i$ and the molecular diffusivity κ_m: $F = \kappa_m \partial S/\partial x_i$, where F is the diffusive flux of the compound S and $\partial/\partial x_i$ the partial derivative with respect to x_i (index i is between 1 and 3). The flux F is always perpendicular to the isoscalar surfaces of the compound and the total flux is proportional to the isoscalar surface size (*Winters and D'Asaro*, 1996). If there are no gradients F becomes zero and the compound is well mixed. Since the molecular viscosity/diffusivity is almost constant in the ranges of velocity and temperature that we are interested in, the only way to increase the total flux is to increase the gradients or the area of the isoscalar surface. This is the effect of the eddies in the turbulent flow in the water volume: They increase the isoscalar surface and the gradients by shearing and straining the water volume and thus increase the tracer flux within this water volume. In an oceanographic context it is technically not possible to measure the smallest scales resolved good enough over the whole water volume of interest and to calculate the total flux of a compound. An approximation for the total flux is to define a turbulent diffusivity κ which is (analogous to Ficks Law) multiplied by a large scale gradient $\langle \partial S/\partial x_i \rangle$, where $\langle . \rangle$ defines an average, which was chosen according to the circumstances (e.g. a volumetric- or time-average). An example of this stirring and mixing

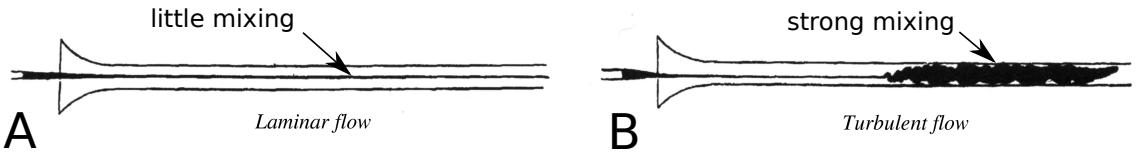

Figure 3.1.: Turbulence in a pipe, experiment from *Reynolds* (1883). Figure adapted. (a) laminar flow. (b) turbulent flow.

is the difference between salinity and temperature diffusivities in laminar flows: The molecular diffusivity for temperature is $\kappa_m(T) \approx 1 \times 10^{-7}$ m^2 s^{-1} and for salinity $\kappa_m(S) \approx 1 \times 10^{-9}$ m^2 s^{-1} (*Gill*, 1982), 100 times lower. However, in high Reynolds number flows, eddy diffusivities for salinity and temperature are similar, as it will be for example shown in this thesis for the Gotland Basin (Chap. 7).

3.1. Mixing and tracer release experiments

A perfect ocean tracer for tracer release experiments would be a substance which does not change any characteristics of water. Furthermore it should still be detectable in very low concentrations and it should be easy to measure and not interfere with any component of the seawater. And it should be cheap. In practice two different types of tracers have been used mainly for oceanographic tracer injection experiments: Dyes and the chlorofluorocarbons (CFCs) SF_6 and CF_3SF_5. Both types have some of the demands and lack others, their respective advantages/disadvantages are introduced below.

3.1.1. Dye tracers

The most widely used tracers are dye tracers. Their advantage is the possibility to measure them directly in the water. The technical principle of dye sensors is the emission of a light flash. This emitted light excites the fluorescent dyes, which will re-emit light at the fluorescence wavelength of the dye. The strength of the fluorescent light depends on the dye concentration in the water. Two very common dyes in oceanography are Rhodamin WT and Fluorescein. Rhodamin WT has an excitation wavelength of 500 nm and emits at 590 nm (red). Fluorescein is excited at 485 nm and emits 530 nm (green). Since Chlorophyll-a also has fluorescent properties, this technique is used to measure Chlorophyll-a concentration in the water as well (excitation wavelength 430 nm, emitting wavelength 685 nm). The detection limits for in situ measurements are 0.01 μg l^{-1} $= 1 \times 10^{-8}$ kg m^{-3} (all wavelengths and detection limits refer to the Chelsea Aquatracka III sensor) and do not differ between the different dyes. The main differences between Rhodamin and Fluorescein are the stability in sunlight and the price. Fluorescein degrades much faster and cannot be considered as a passive tracer in the euphotic zone. Exponential decay rates of the order of 0.1 h^{-1} in the water and direct sunlight have been reported (*Smart and Laidlaw*, 1977). The decay rate of Rhodamin WT is negligible for experiments of 5 days (*Ledwell and Duda*, 2004). Opinions about the tendency of dyes to be adsorbed on particles differ: *Ledwell and Duda* (2004) did not experience any adsorption in a year-long laboratory experiment exposing a dye solution to mud and organic particulates whereas *Smart and Laidlaw* (1977) report an adsorption onto organic particles. Despite this disagreement none of the dye experiments known to us explicitly describe a sinking or an adsorption on particles. Further advantages are the good solubility of the dyes and the non-toxicity, making the handling easy, except that clothes and hands might be stained with colour after contact with the dye. Release techniques are usually a pre-mixing of the dye in drums and an injection using standard material such as garden hoses and simple diffusers.

Several experiments analysing dispersion have been performed with dyes. *Okubo* (1971) summarised numerous horizontal dispersion experiments and developed an empirical formula of horizontal diffusivity versus the size of the dye patch. *Woods* (1968) photographed the breaking of internal wave billows in the Mediterranean thermocline near Malta. Vertical mixing experiments using dyes by *Schuert* (1970), *Kullenberg* (1977), *Vasholz and Crawford* (1985) and *Ledwell and Duda* (2004) show the long history of dye tracers for studying ocean mixing. Nevertheless the

detection limits and the stability properties of the dyes limit all experiments to scales of the order of tenths of kilometres and to several days. Taking e.g. the detection limit of dye shows that a dye release in the BaTRE project would not be a feasible option: Comparing the detection limits with the SF_6 and CF_3SF_5 tracers (see below) differences are of the order of 10^6, and a substitution of the 900 g of CF_3SF_5 with dye would be 4600 tonnes of dye. Handling this amount of dye is not a realistic option, starting from permission for the injection of several kilo-tonnes of a substance, to the diffuser technology. Dye tracers are therefore not a good choice for basin scale experiments.

3.1.2. SF_6 and CF_3SF_5

The artificially produced and not naturally occurring sulphur hexafluoride (SF_6) is a perfluorine gas at room temperature and becomes a liquid at pressures exceeding 20 bar. The fluid has a density of $\rho = 1880$ kg m^{-3}. SF_6 is commercially produced for use as a gaseous insulator in high voltage installations and its yearly production is estimated at 5×10^6 kg (*Ko et al.*, 1993). The atmospheric concentration in parts per trillion by volume (pptv) was 4.60 ± 0.03 pptv in October 2003 and increases with $(6.5\pm1.3)\%$ per year (*Burgess et al.*, 2004). The solubility of SF_6 is very low, the sea water surface concentration in equilibrium with the atmospheric concentration of about 4 pptv is of the order of 0.7 – 2 fmol kg^{-1} (*Watson and Ledwell*, 2000). Background concentrations in 800 m in the Santa Monica Basin are of the order of 1.5 fmol kg^{-1} (*Ledwell and Watson*, 1991). The total amount of SF_6 in the ocean is assessed to be around 3×10^4 kg, or 2×10^5 mol (*Ledwell et al.*, 1998). SF_6 is included into the Kyoto Protocol because, on a molecular basis, it is a powerful greenhouse gas with a long lifetime in the atmosphere (*Wanninkhof*, 1992), but, due to the small concentrations, it will remain an insignificant contributor to the anthropogenic greenhouse effect over the next 50 years (*Victor and MacDonald*, 1999). SF_6 is measured by electron capture gas chromatography and can be detected in sea water in concentrations down to 0.01 fmol kg^{-1} (*Watson and Ledwell*, 2000). This low detection limit, the non-toxicity, the low marine background concentration and the inertness makes SF_6 an almost ideal tracer. A disadvantage is the technical challenge of a controlled SF_6 release due to the low solubility. For amounts of a few moles, SF_6 can be dissolved in water drums on deck and then released at the desired depth (*Ledwell and Watson*, 1991). The Ocean Tracer Injection System (OTIS), designed at the Woods Hole Oceanographic Institute, overcame the technical challenges of a large-scale and high-precision SF_6 release, see Fig. 3.2 for the OTIS used in the BaTRE project. The OTIS sprays the tracer through orifices with a diameter of 50 μm into the water. The size of the sprayed droplets is small enough that despite the low solubility the tracer is dissolved shortly after the injection and does thus not sink down, a zoom on the OTIS orifices can be seen in Fig. 3.2b. Since the first injection in 1986, numerous experiments have used SF_6, the inertness and the low detection limit make it a perfect tracer for long-term vertical mixing studies in lakes (*Maiss et al.*, 1994), ocean basins (*Ledwell and Watson*, 1991; *Ledwell and Hickey*, 1995) and oceans (*Ledwell et al.*, 1998; *Ledwell et al.*, 2000; *Messias et al.*, 2008).

Estimating the water age (defined as the last contact with the atmosphere) can be done by measuring concentrations of tracers in the water that have a unique relationship to the atmospheric concentration with time. This may, for example, be a steady in- or decreasing concentration. The atmospheric concentrations of the substances CFC-11 and CFC-12, CFC-113 and CCl_4 increased until the early 1990s and were used in several studies as water age tracers (e.g. *Bullister and Weiss*, 1983; *Wisegarver and Gammon*, 1988; *Rhein*, 1991; *Krysell*, 1992; *Rhein et al.*, 2000; *Smethie and Fine*, 2001). Due to the global CFC ban, which was negotiated by virtually all countries worldwide in the 1990s, the concentrations of these tracers rose slower or even decreased. This limited their use as water age tracers dramatically. In contrast to that,

the atmospheric concentration of SF_6 increased steadily and nearly linearly over the past few decades and emerged as a new transient tracer for the investigation of the water age (*Law and Watson*, 2001; *Tanhua et al.*, 2004; *Bullister et al.*, 2006; *Tanhua et al.*, 2008). Previous large ocean tracer experiments injected amounts between 110 kg (*Ledwell et al.*, 2000), 140 kg *Ledwell et al.* (1998) and 220 kg (*Messias et al.*, 2008), adding up to roughly 500 kg, or 2% of the global SF_6 budget in the ocean. Further experiments will therefore certainly perturb the use of SF_6 as a transient tracer. A combination of the water age and a SF_6 release experiment has been done by *Olsson et al.* (2005a,b). An alternative to SF_6 is the CFC trifluoromethyl sulphur pentafluoride: CF_3SF_5. Chemical similarities, behaviour in water and techniques for injection, sampling and analysis allows CF_3SF_5 to be used in almost the same manner as SF_6. CF_3SF_5 is not used as an industrial product and only specialised companies can produce it, making it more expensive. This also means that the background concentration in the atmosphere and ocean is zero. There are differences in the solubility of SF_6 and CF_3SF_5; the latter is half as soluble as the former in freshwater. A lower solubility requires smaller orifices on the OTIS injection system. The OTIS system of the IFM Geomar in Kiel, Germany and the Leibniz Institute for Baltic Sea Research, Warnemünde, Germany for example has orifices with 25 μm diameter instead of the 50 μm used for SF_6. Furthermore, the solubility in 1-octanol at 20°C is 1000 and 150 times greater than in freshwater for CF_3SF_5 and SF_6 respectively. This suggests an enhanced tendency of CF_3SF_5 to adhere to organic particles. Systematic studies about the particle affinity of CF_3SF_5 are performed at the moment but no clear results have been published so far. Nevertheless, the tracer distributions during the BaTRE project did not show any sign of significant particle adsorption. The first release of CF_3SF_5 was done in the Santa Monica Basin in January 2005 (*Ho et al.*, 2008) where, almost twenty years ago, the pilot SF_6 injection was conducted (*Ledwell and Watson*, 1991). It was a mixture of 10.6 moles (1.4 kg) SF_6 and 10.0 moles (2 kg) CF_3SF_5 in 800 m depth injected using an orifice size of 50 μm. *Ho et al.* (2008) report, using a water sample size of 20 ml, a minimum detectable concentration level of 0.4 and 0.8 fmol kg^{-1} for SF_6 and CF_3SF_5 respectively. The profiles taken in the Santa Monica Basin showed almost identical distributions and proved that CF_3SF_5 is a viable replacement for SF_6 as an ocean tracer. Since then CF_3SF_5 injections have been done in the Baltic (this work, September 2007, 900 g), the equatorial Atlantic (Guinea Dome Tracer Release Experiment, GUTRE, May 2008, 92 kg, Toste Tanhua, pers. communication) and in the Southern Ocean, February 2009, 76 kg (*Ledwell et al.*, 2011).

Figure 3.2.: The Ocean Tracer Injection System, OTIS, (a) on board of the RV Poseidon September 2007. Zoom on the injection orificies (b).

3.2. Turbulence, microstructure and mixing

This section shows how the measurement of the dissipation rate of turbulent kinetic energy can be used to estimate turbulent diffusivities.

The scales of geophysical turbulent flows range between hundreds of kilometres (in our case the size of the Gotland Basin) down to the scales of millimetres. This means that it is virtually not possible to resolve all these scales in the ocean with e.g. a sensor. This holds also for a numerical model, which would require vast (and not available) amounts of computational power to calculate all these scales. Nevertheless, the general interest is typically not focussed on the smallest scales of the velocity, temperature or salinity fields, but on a mean distribution depicting the general flow of the system. This mean distribution is ideally calculated by an ensemble-average over many experiments with the same boundary conditions, or in oceanographic measurements as a time- or spatial-average or a combination of both. The evolution of the averaged quantities can be calculated by decomposing them into a mean (denoted by angle brackets) and a fluctuating part (denoted by apostrophe), this is called the Reynolds decomposition:

$$u_i = \langle u_i \rangle + u_i' \tag{3.2}$$

$$T = \langle T \rangle + T' \tag{3.3}$$

$$S = \langle S \rangle + S'. \tag{3.4}$$

Properties of the decomposed quantities are that the average of the fluctuating parts is zero (taking S as an example): $\langle S' \rangle = 0$. The sum of two variables to be averaged is the sum of the variables averaged alone: $\langle S_1 + S_2 \rangle = \langle S_1 \rangle + \langle S_2 \rangle$. Averaging an already averaged variable does not have an effect: $\langle \langle S \rangle \rangle = \langle S \rangle$. The average of a fluctuating times an average part is zero: $\langle S' \langle S \rangle \rangle = 0$. Using the Reynolds decomposition, the equations of motions of the velocity without rotation and the Boussinesq approximation

$$\frac{\partial u_i}{\partial t} + u_j \frac{\partial u_i}{\partial x_j} = -\frac{1}{\rho_0}\frac{\partial p}{\partial x_i} - g\rho\delta_{13} + \frac{\partial}{\partial x_j}\left(\nu \frac{\partial u_i}{\partial x_j}\right) , \tag{3.5}$$

can be decomposed into the the mean part

$$\frac{\partial \langle u_i \rangle}{\partial t} + \langle u_j \rangle \frac{\partial \langle u_i \rangle}{\partial x_j} = -\frac{1}{\rho_0}\frac{\partial \langle p \rangle}{\partial x_i} - g \langle \rho \rangle \delta_{13} + \frac{\partial}{\partial x_j}\left(\nu \frac{\partial \langle u_i \rangle}{\partial x_j} - \left\langle u_i' u_j' \right\rangle\right) , \tag{3.6}$$

and the fluctuating part (not shown here, but easy to derive from Eq. (3.5), see e.g. *Kundu and Cohen* (2008), Chapter 5). Comparing Eq. (3.5) and Eq. (3.6) shows that the equations look similar, with the velocity, pressure and density replaced by the averaged quantities, except for the last term in Eq. (3.6): $\langle u_i' u_j' \rangle$. This symmetric second order tensor acts as an additional stress on the mean velocity and is called (after a multiplication with the density ρ_0) the *Reynolds stress tensor*. The Reynolds stress tensor $\rho_0 \langle u_i' u_j' \rangle$ transports momentum in the j-direction along the i-axis. Due to the symmetry this is equal to the transport of momentum in the i-direction along the j-axis. A Reynolds decomposition of the kinetic energy per unit mass $E = u_i u_i$ yields the evolution of the kinetic energy of the mean flow $\overline{E} = \frac{1}{2}\langle u_i \rangle \langle u_i \rangle$ and the turbulent kinetic energy (TKE) $K = \frac{1}{2}\langle u_i' u_i' \rangle$:

$$\frac{\mathrm{D}\overline{E}}{\mathrm{D}t} + \frac{\partial \overline{T}_i}{\partial x_i} = -P - \bar{\varepsilon} - \frac{g}{\rho_0}\bar{\rho}\langle u_3 \rangle \tag{3.7}$$

$$\frac{\mathrm{D}K}{\mathrm{D}t} + \frac{\partial T_i'}{\partial x_i} = P - \varepsilon + B , \tag{3.8}$$

where $\overline{T}_i$, T_i' are transport terms, P the production term of the turbulent kinetic energy and $\bar{\varepsilon}$ and ε the dissipation rates of the mean kinetic energy and of the turbulent kinetic energy respectively. The production term P of TKE, which is at the same time a sink of $\overline{E}$, is defined as

$$P = -\langle u_i' u_j' \rangle \frac{\partial \langle u_i \rangle}{\partial x_j} , \tag{3.9}$$

while the dissipation of mean kinetic energy is given by:

$$\bar{\varepsilon} = 2\nu \langle s_{ij} \rangle \langle s_{ij} \rangle , \tag{3.10}$$

the dissipation of TKE by

$$\varepsilon = 2\nu \left\langle s_{ij}' s_{ij}' \right\rangle , \tag{3.11}$$

and the buoyancy production by

$$B = -\frac{g}{\rho_o} \left\langle w' \rho' \right\rangle . \tag{3.12}$$

Here ν is the molecular viscosity and s_{ij} are the shear tensors:

$$s_{ij}' = \frac{1}{2}\left(\frac{\partial u_i'}{\partial x_j} + \frac{\partial u_j'}{\partial x_i}\right) , \tag{3.13}$$

for the fluctuating velocities s'_{ij} and the average velocities $\langle s_{ij} \rangle$. The tensor $\langle u'_i u'_j \rangle$ in Eq. (3.9), which also appears in the Reynolds stress tensor, has an important role in the transfer of energy from the mean kinetic energy into the turbulent kinetic energy. Sinks of kinetic energy are the dissipations $\overline{\varepsilon}$ and ε, but, due to the much larger gradients at the small scales, ε can be treated as the only important term. Energy is thus transported from $\overline{E}$ via P into K. TKE is dissipated into heat via ε. The buoyancy flux term B can be of either sign. In unstable stratification and the resulting convection B is a source term for TKE, whereas in stable stratification TKE is converted into potential energy and B is the corresponding sink term. A derivation of Eq. (3.7) and Eq. (3.8) can be found in e.g. *Kundu and Cohen* (2008). If it is assumed that the TKE is produced and dissipated locally and in steady state, the transport term and time derivative can be neglected (*Osborn*, 1980); Eq. (3.8) becomes a balance between the local production of TKE, the local dissipation into heat and the buoyancy flux:

$$-P = -\varepsilon + B\,. \tag{3.14}$$

If the buoyancy flux would be larger than the production the TKE would not be in steady state and so it must hold in stable stratification that

$$\frac{-B}{P} \equiv R_f < 1\,, \tag{3.15}$$

where the flux Richardson number R_f was defined as the ratio of the buoyancy destruction $-B$ and the TKE production P. Using the definition of R_f Eq. 3.14 can be rewritten as

$$\begin{aligned} B &= -\varepsilon R_f + R_f B \\ &= -\varepsilon \frac{R_f}{1 - R_f} \\ &= -\gamma \varepsilon\,, \end{aligned} \tag{3.16}$$

where γ is the mixing efficiency and is commonly used in microstructure literature. The significance of Eq. (3.16) is the relation of the buoyancy flux with the dissipation rate of TKE via a properly defined mixing efficiency γ. This relation can be used to bring the increase of potential energy in relation to a mean dissipation rate (Chap. 6.5.1) and to derive a turbulent diffusivity κ: As argued in Chap. 3 in analogy to Ficks Law, the total flux of a compound is defined by the product of a turbulent diffusivity κ and a mean gradient. The physical interpretation is that the random Brownian molecule movements which result, after being averaged over a volume larger than the path-length of the molecule movement, to a flux proportional to the molecular diffusivity κ_m and the gradient of the compound. The chaotic turbulent eddies, averaged over a volume larger than the size of the eddies, act in a similar way to the Brownian molecule movement and thus proportional to the turbulent diffusivity κ and the gradient. In terms of density the buoyancy flux B can thus expressed by:

$$\begin{aligned} -B &= \frac{g \langle w' \rho' \rangle}{\rho_0} \\ &= -\kappa_\rho \frac{g}{\rho_0} \left\langle \frac{\partial \rho}{\partial z} \right\rangle \\ &= \kappa_\rho N^2\,. \end{aligned} \tag{3.17}$$

Where N^2 is the buoyancy frequency $N^2 \equiv -g\rho_0^{-1} \langle \partial\rho/\partial z \rangle$. When Eq. (3.17) and Eq. (3.16) are combined, the turbulent diffusivity can be expressed as a function of the dissipation rate ε and the mean stratification, the buoyancy frequency N^2:

$$\kappa_\rho = \gamma \frac{\varepsilon}{N^2} \,. \tag{3.18}$$

ε and N^2 can be measured by e.g. a microstructure profiler. The unknown variable in Eq. (3.18) is the mixing efficiency which can vary between practically 0 in e.g. well-mixed bottom boundary layers (*Shih et al.*, 2000; *Burchard et al.*, 2009), intermediate values of 0.1 in the equatorial ocean (*Rhein et al.*, 2010) and its maximum of 0.2 (*Osborn*, 1980).

Shear Microstructure

This section covers the velocity shear profiler used in the BaTRE project and the underlying assumptions. For a overview of the microstructure profiling technique and their principle refer to *Lueck et al.* (2002). As shown in Eq. (3.18) a measured dissipation rate ε can be used to estimate the vertical flux using an eddy diffusivity κ and a mean stratification. A way to measure ε is via the shear spectrum: If isotropic turbulence is assumed for dissipation scales, the average of the second order shear tensor squared $\langle s_{ij} s_{ij} \rangle$ becomes:

$$\begin{aligned} \varepsilon &= 2\nu \left\langle s'_{ij} s'_{ij} \right\rangle \\ &= \nu \left\langle \frac{\partial u'_i}{\partial x_j} \frac{\partial u'_j}{\partial x_i} \right\rangle \qquad (3.19) \\ &= C_{ij} \nu \left\langle \left(\frac{\partial u'_i}{\partial x_j} \right)^2 \right\rangle , \qquad (3.20) \end{aligned}$$

$C_{ij} = 15$ for $i = j$ and $15/2$ otherwise (no summation in Eq. (3.20)). A detailed derivation can be found in e.g. *Pope* (2000), Chapter 5.3. For a vertically falling profiler measuring horizontal velocities i equals 1 and j equals 3:

$$\varepsilon = \frac{15}{2} \nu \left\langle \left(\frac{\partial u'}{\partial z} \right)^2 \right\rangle . \tag{3.21}$$

Knowledge of the shear fluctuations therefore gives the dissipation ε of TKE. This fact is technically much easier to solve than it is to measure shear spectra in all three directions of space. A way to calculate the dissipation of TKE can be the integration of the shear power spectrum times the viscosity and the factor C_{ij}

$$\varepsilon = \int_0^\infty S(k)\, dk \,, \tag{3.22}$$

where k is a vertical wavenumber. In the turbulence energy spectra, the part of the spectrum where production of TKE occurs and the energy of the turbulence resides is clearly separated from a second part of the spectrum where the dissipation of TKE occurs. The intermediate part of the spectrum is called the inertial subrange and is unique in the spectrum due to its role of energy transfer from the large scale energy containing part into the small scale dissipative part of the spectrum. The dissipative part of the shear is between the wavenumbers $0.1 k_K$ and k_K ($k_K = (\varepsilon/\nu^3)^{0.25}$: Kolmogorov wavenumber, smallest size of eddies) and it therefore suffices to

measure the shear spectrum in this range. The integration limits of Eq. (3.22) can be reduced for the calculation of ε to:

$$\varepsilon = \int_2^{k_K} S(k)\, dk + \varepsilon_c\,. \tag{3.23}$$

The shape of the dissipative spectrum is known and is used to calculate the correction term ε_c due to the missing part of the spectrum (wavenumbers below 2 cpm (cycles per minute) and above k_K). Details of the correction are described in *Moum et al.* (1995).

Since the inertial subrange, as well as the smaller scale parts, are isotropic, the largest isotropic scales and thus the inertial subrange are bounded by the Ozmidov scale L_O, the scale at which eddies are influenced and deformed by the stratification and $10L_K$, ten times the Kolmogorov scale at which dissipation starts to remove energy from the eddy field (*Smyth and Moum*, 2000a). In a low turbulence situation with an ε of $O(10^{-9})$ and a typical stratification in the Gotland Basin, the Ozmidov wavenumber even falls into the beginning of the dissipative range, Fig. 3.3. The stratification thus violates the isotropy assumption which was used to simplify the shear tensors to calculate the dissipation ε in Eq. (3.21). Criteria whether the isotropy spectra can be used, are tested by *Gargett et al.* (1984) and *Smyth and Moum* (2000b) based on the intermittency factor I or the buoyancy Reynolds Number Re_b,

$$\begin{aligned} I &= \frac{L_O}{L_K} \\ &= \frac{(\varepsilon/N^2)^{1/2}}{(\nu^3/\varepsilon)^{1/4}} \\ &= \left(\frac{\varepsilon}{\nu N^2}\right)^{\frac{3}{4}} \\ &= (Re_b)^{\frac{3}{4}}\,, \end{aligned} \tag{3.24}$$

the ratio between the Ozmidov and the Kolmogorov scales. If Re_b exceeds 200 the turbulence in the dissipative subrange is certainly isotropic. If Re_b is below 2.45 turbulence produces no significant buoyancy flux. The range in between these two extremes is less well-defined, but *Denman and Gargett* (1988) state that ε measurements in anisotropic turbulence can be overestimated by about a factor of 3. Direct numerical simulations of stratified shear flow do not necessarily show this overestimation. *Smyth and Moum* (2000b) simulated a Kelvin-Helmholtz instability and the subsequent breaking. The shear was defined to be in x-direction: $\langle \partial u/\partial z \rangle \neq 0$, $\langle \partial v/\partial z \rangle = 0$. Dissipation rates for different buoyancy Reynolds numbers calculated by $\left\langle (\partial u'/\partial z)^2 \right\rangle$ overestimated ε by the above mentioned factor of 3, whereas measuring the vertical shear of the v velocities: $\left\langle (\partial v'/\partial z)^2 \right\rangle$ resulted in correct or much lower ε. This shows that in the experiment made by *Smyth and Moum* (2000b) not even horizontally homogeneous turbulence can be assumed. With free falling microstructure devices such as the MSS (Microstructure Sonde, ISW), shear is measured at a single position. According to Eq. (3.21) and Eq. (3.22) shear autocorrelation data over the wavenumber space k is needed whereas a descending profiler measures the spectrum in time and at different positions. The conversion from a time spectrum to wavenumber spectrum is done by assuming that during the falling of the MSS the measured turbulence is "frozen", meaning that it does not change its properties during the measuring time of the MSS. A signal over time can thus be replaced by a signal over space. This assumption is called Taylors frozen turbulence hypothesis. The smallest resolvable wavenumber is then obtained by dividing the sampling frequency f_s by the falling speed of the profiler w_f: $k = 2\pi f_s/w_f$. It is further-

more assumed that the turbulence is isotropic; a necessary requisite since otherwise Eq. (3.21) does not hold. Fig. 3.3 gives an example of a shear spectrum measured in the central Gotland Basin in approx. 190 m depth. For comparison Nasmyth spectra for ε acquired by applying Eq. (3.23) and for $\varepsilon = 1 \times 10^{-10}$ W kg^{-1} are shown. A comparison of the shear spectra with the Ozmidov scales Eq. (B.2), Tab. B.1 and Fig. 3.3 for typical stratifications in the Gotland Basin reveals the limitations of TKE dissipation measurements using shear profilers in the Baltic Sea: For $\varepsilon = 1 \times 10^{-9}$ W kg^{-1} and lower a significant part of the dissipative spectrum lies within the Ozmidov scales. Turbulence in this wavenumber region is influenced by stratification and isotropy cannot be assumed anymore, see also Fig. 4.5. For reference Kolmogorov and Ozmidov lengths for typical dissipations rates and stratifications found in the Gotland Basin during the BaTRE project are given in table B.1.

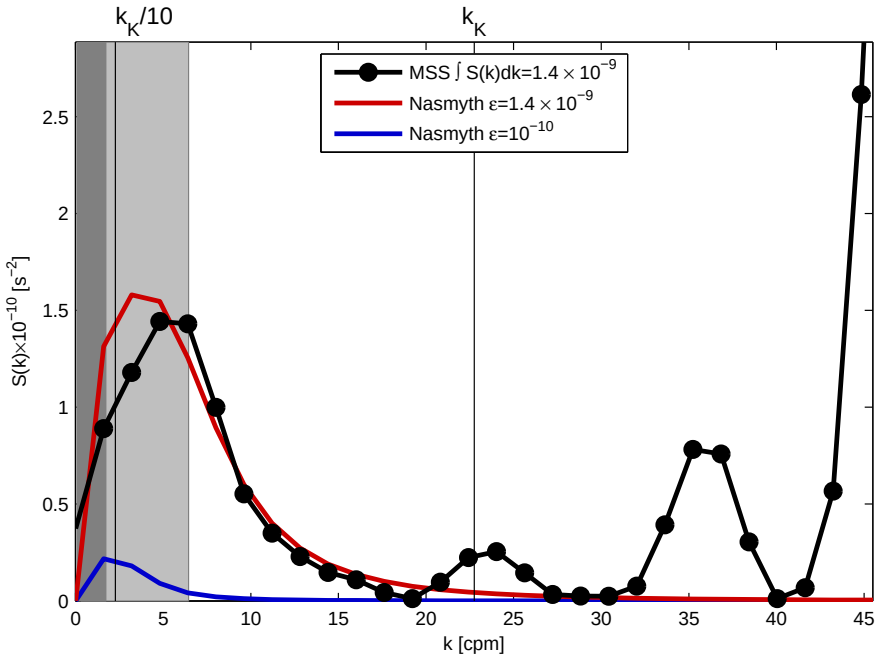

Figure 3.3.: MSS shear spectrum $S(k)$ measured in 190 m in the central Gotland Basin, black, theoretical Nasmyth spectrum for $\varepsilon = \int S(k)$, red and a Nasmyth spectrum for $\varepsilon = 1 \times 10^{-10}$ W kg^{-1}, blue. The Kolmogorov wavelength k_K and $k_K/10$ are indicated by black lines. A range of Ozmidov wavelengths k_O for stratifications ranging from $N^2 = 0.5 \times 10^{-6}$ to 3×10^{-5} s^{-2} is shaded in grey for $\varepsilon = 1.4 \times 10^{-9}$ m^2 s^{-1} ($Re_b = 31.1$) and in light grey for $\varepsilon = 1 \times 10^{-10}$ m^2 s^{-1} ($Re_b = 2.2$). Buoyancy Reynolds number Re_b are for calculated with N$^2 = 3 \times 10^{-5}$ s^{-2}.

3.3. Basin-scale budgets

The long-term variability observed in the hydrographic quantities can be used to draw some conclusions about the variability of the most important mixing parameters by constructing basin-scale budgets for these quantities (*Gloor et al.*, 2000; *Axell*, 1998; *Ledwell and Hickey*, 1995). Considering a fixed control volume V that is bounded by the bottom from below, and from above by a horizontal surface with area A at vertical position z_t, the budget method exploits the fact that the integral rate of change of any conserved quantity inside the control volume must

be balanced by the sum of advective and turbulent fluxes across the upper boundary (sediment fluxes are ignored).

3.3.1. Salinity and heat budgets

Taking salinity as an example, a relation can be found between the average turbulent diffusivity, $\bar{\kappa}_S$ at z_t and the decay rate of the average salinity in the control volume:

$$\bar{\kappa}_S = \frac{V}{A}\frac{1}{\partial\bar{S}/\partial z}\frac{\mathrm{d}\langle \mathrm{S}\rangle_\mathrm{V}}{\mathrm{d}t}\,, \tag{3.25}$$

where t is time, $\langle\cdots\rangle_V$ denotes the spatial average over the control volume, and the bar the area average over the upper bounding surface (*Gloor et al.*, 2000; *Ledwell and Hickey*, 1995). We have assumed that the turbulent flux of salinity is related to the turbulent diffusivity according to $\bar{F}_S = -\bar{\kappa}_S\partial\bar{S}/\partial z$, and ignored the advective flux of salinity through the upper boundary of the control volume. The latter assumption is justified by the facts that (a) advection due to haline intrusions into the deep water are negligible during the stagnation period considered here, and (b) short-term advective fluxes caused e.g. by internal wave motions cancel if the time derivative appearing on the right hand side of Eq. (3.25) is understood as a representation of the *long-term* variability in the deep water salinity. An analogous relation may be derived for the diffusivity of heat, $\bar{\kappa}_T$. It is worth noting that in situations where the advective fluxes across the top of the control volume are not negligible, the expression in Eq. (3.25) can be shown to provide a lower bound for the diffusivity of salt (and, analogously, for the diffusivity of heat) if the net advective inflow is salty and warm as in the case considered here (*Wieczorek et al.*, 2008; *Ledwell and Hickey*, 1995).

3.3.2. Budget of potential energy

In a stratified fluid, mixing is associated with a conversion of turbulent kinetic energy into potential energy due to molecular destruction of small-scale density gradients (*Winters et al.*, 1995). Conversely, this implies that observations of the change of potential energy may be used to draw conclusions about the energetics of mixing.

To exploit this fact, we start from the definition of the potential energy with respect to the density ρ_r for a Boussinesq fluid,

$$E_p = \frac{g}{\rho_0}\int_V \sigma_\theta \tilde{z}\,\mathrm{d}V\,, \tag{3.26}$$

where $\sigma_\theta = \rho - \rho_r$ and we integrate over a control volume bounded by the bottom and a horizontal surface at z_t (E_p is referenced with respect to the upper boundary of the control volume: $\tilde{z} = z - z_t$). Using this definition, it can be shown that the temporal evolution of E_p is only a result of the internal advective and turbulent buoyancy fluxes:

$$\frac{\mathrm{d}E_p}{\mathrm{d}t} = \frac{g}{\rho_0}\int_V w\sigma_\theta\,\mathrm{d}V - \int_V B\,\mathrm{d}V\,, \tag{3.27}$$

where B denotes the vertical turbulent buoyancy flux, and w the Reynolds-averaged vertical velocity (see *Hughes et al.*, 2009). A detailed derivation of Eq. (3.27) can be found in Chap. A of the Appendix.

Short-term fluctuations in E_p caused by high-frequency reversible motions inside the control volume (e.g. due to internal and topographic waves) are likely to cancel out on the long-term average. Since changes of deep-water potential energy due to dense water inflows can be excluded

as well during the stagnation period considered here, it is reasonable to expect that

$$\left\langle \frac{\mathrm{d}E_p}{\mathrm{d}t} \right\rangle_T \approx -\left\langle \int_V B \,\mathrm{d}V \right\rangle_T , \tag{3.28}$$

where $\langle \cdots \rangle_T$ denotes a suitably chosen long-term time average. Since the turbulent buoyancy flux B is generally negative in a stably stratified fluid, we expect a long-term increase of potential energy due to mixing.

Expressing the integrated buoyancy flux as the product of a (not necessarily constant) mixing efficiency γ and the integrated dissipation rate, Eq. (3.28) can be re-written as

$$\left\langle \frac{\mathrm{d}E_p}{\mathrm{d}t} \right\rangle_T \approx \gamma V \langle \langle \varepsilon \rangle_V \rangle_T , \tag{3.29}$$

which provides a useful relation for estimating the average deep-water dissipation rate $\langle \varepsilon \rangle_V$ from hydrographic measurements.

The canonical value $\gamma = 0.2$ is appropriate for mixing remote from boundaries (*Hughes et al.*, 2009; *Shih et al.*, 2005; *Osborn*, 1980), noting that mixing inside the bottom boundary layer is expected to be much less efficient due to lower stratification and higher turbulence energy levels (*Garrett et al.*, 1993; *Umlauf and Burchard*, 2011). Thus, if the bottom boundary layer contributes substantially to total mixing, dissipation rates computed from Eq. (3.29) are likely to be overestimated. This will be discussed in Chap. 7.

3.4. Internal waves

If and how much internal waves contribute to the deep water mixing in the Gotland Basin has been addressed by *Axell* (1998, 2002), but with lacking observational proof. During the BaTRE project clear evidence of internal wave spectra has been found. An attempt to quantify the energy transport due to internal waves has been made by applying linear internal wave theory. This section shows the theoretical background for the internal wave analysis done in Chap. 7.1.5.

3.4.1. WKB, dispersion, phase velocity, group velocity

The theory here is based on linear, free internal wave theory in stratified and rotating fluids with the Wentzel-Kramers-Brillouin (WKB) approximation. For details of the derivation refer to e.g. *Kundu and Cohen* (2008).

The energy flux of an internal wave is

$$\mathbf{F} = E\mathbf{c_g} , \tag{3.30}$$

with E the energy (kinetic E_k + potential E_p) and the group velocity of the wave $\mathbf{c_g}$. The central BaTRE (C1) mooring measured the density in six depths and the velocities over a depth interval of approx. 24 m. This data can be analysed to yield the kinetic energy E_k, the frequency of the wave ω and the stratification N^2. The inertial frequency f is defined by the latitude of the mooring. As we will show, this data, together with the dispersion relation, is sufficient to calculate the vertical group speed c_{g_z}: The frequency of the internal wave can either be measured directly or calculated by the relation between the potential and kinetic energy

$$R = \frac{\omega^2 - f^2}{(f^2 + \omega^2(1 - 2f^2/N^2))} . \tag{3.31}$$

The dispersion relation of internal wave rays with the WKB approximation is

$$\omega^2 = \frac{N^2k^2 + f^2m^2}{K^2}, \tag{3.32}$$

with the wavenumber vector

$$\mathbf{K} = (k, l, m) \tag{3.33}$$

and $K^2 = k^2 + l^2 + m^2$. Note that the coordinate system has been rotated such that the x-coordinate is in the direction of propagation and therefore the wavenumber l is in y-direction $l = 0$. The angle Θ between the horizontal wavenumber k and the wavenumber $\mathbf{K}$ gives

$$\tan\Theta = \frac{m}{k}, \tag{3.34}$$

and can be calculated by the dispersion relation

$$\tan\Theta = \frac{m}{k} = \sqrt{\frac{N^2 - \omega^2}{\omega^2 - f^2}}. \tag{3.35}$$

Experimental evidence for the dispersion relation has been found by *Görtler* (1943) and *Mowbray and Rarity* (1967). An interesting consequence of this relation is that the angle is solely defined by the stratification, the wave frequency and the latitude, meaning that the angle of reflection is also constrained by these parameters. This leads to the so called "critical angles" at the ocean bottom or on continental shelfs, where internal waves can be generated or dissipated due to amplification and wave breaking (e.g. *Wunsch and Hendry*, 1972; *Duda and Rainville*, 2008) or reflected and amplified in semi-enclosed basins (*Maas and Lam*, 1995).

As shown in Chap. 7.1.2 and Chap. 7.1.5, the vertically-resolved velocity measurements show a phase shift Δt over a vertical distance Δz. This can be used to calculate the vertical phase velocity $c_z = \Delta z/\Delta t$. Fig. 3.4 gives an example of how an upward-propagating wave results in phase lines tilted to the right in ADCP measurements.

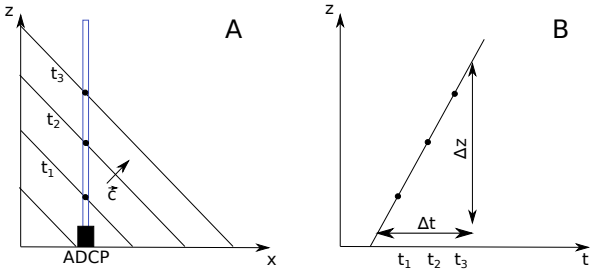

Figure 3.4.: An, in x-z space with the phase speed **c**, upward travelling wave (a) is seen in an z-t resolving ADCP as a phase line tilted to the right (b). By measuring the time Δt of the phase travelling the distance Δz the vertical phase speed $c_z = \Delta z/\Delta t$ can be determined.

Since $c_z = \omega/m$ the vertical wavenumber is m

$$m = \frac{\omega}{c_z} = \sqrt{\frac{N^2k^2 + f^2m^2}{c_z^2(k^2 + m^2)}} = \sqrt{\frac{N^2(\tan\Theta)^{-2} + f^2}{c_z^2((\tan\Theta)^{-2} + 1)}}\,, \tag{3.36}$$

and the horizontal wavenumber k is

$$k = \frac{m}{\tan\Theta}\,. \tag{3.37}$$

The group velocity vector, which is defined as

$$\mathbf{c}_g = \left(\frac{\partial\omega}{\partial k}, \frac{\partial\omega}{\partial m}\right)\,, \tag{3.38}$$

becomes in combination with the dispersion relation Eq. (3.32):

$$c_{g_x} = \frac{(N^2 - f^2)m^2 k}{\omega K^4}\,. \tag{3.39}$$

Analogously in the z-direction with $\dfrac{\partial\omega}{\partial m}$ so that

$$\begin{aligned}\mathbf{c}_g &= \left(\frac{\partial\omega}{\partial k}, \frac{\partial\omega}{\partial m}\right)\\ \mathbf{c}_g &= \frac{(N^2 - f^2)mk}{\omega K^4}(m, -k).\end{aligned} \tag{3.40}$$

The vertical group velocity can thus be expressed by the phase shift, the frequency of the internal wave, the inertial frequency and the stratification as

$$c_{g_z} = f_g(\omega, f, N)c_z\,, \tag{3.41}$$

or

$$f_g(\omega, f, N) = \frac{c_{g_z}}{c_z}\,. \tag{3.42}$$

A general property of the internal wave energy flux can be deduced from Eq. (3.42). $f_g(\omega, f, N)$ for a typical stratification in the Gotland Basin, $N^2 = 2.4\times10^{-5}\ \mathrm{s}^{-2}$, with the inertial frequency at 57°N is shown in Fig. 3.5a. The group velocity goes from zero at the inertial frequency (inertial oscillations do not have a vertical velocity component and thus no vertical phase speed) to the maximum negative group velocity at a frequency of approximately 6 times the inertial frequency. This result should be emphasised, since it means that the fastest group velocities are in frequency ranges in which the internal waves can be considered hydrostatic. Implications are that numerical models with a hydrostatic approximation are principally capable (depending strongly on the horizontal and vertical resolution) to model an important part of the internal wave spectrum.

An alternative approach often used for the quantification of internal wave energy fluxes, is via the covariance of the pressure and velocity variations

$$\mathbf{F} = \left\langle \mathbf{u}' p' \right\rangle_\Phi\,. \tag{3.43}$$

where $\langle\cdot\rangle_\Phi$ denotes an average over a wave phase. Horizontal velocities u', v' are large enough

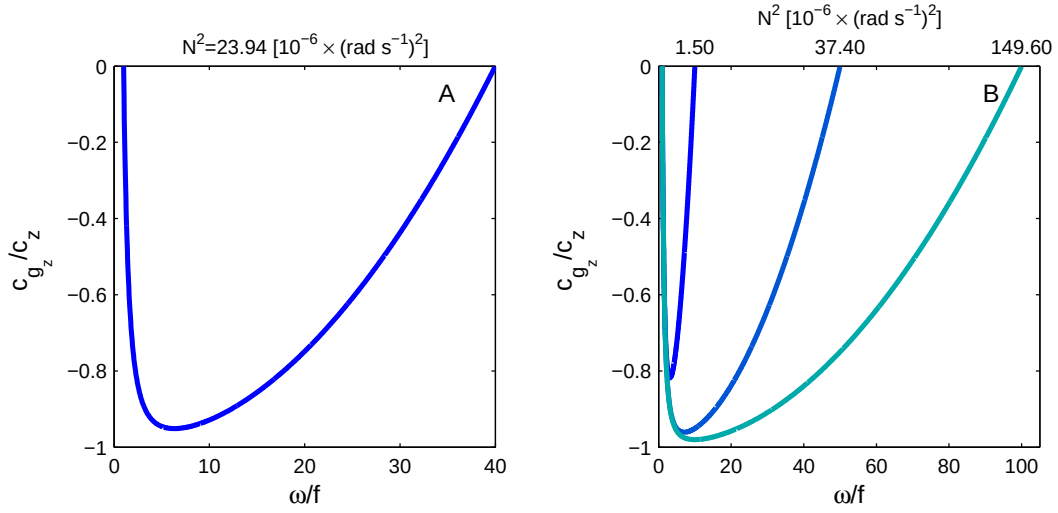

Figure 3.5.: Function $f_g(\omega, f, N)$ (Eq. (3.41)) correlating the vertical phase speed of linear internal waves with the vertical group velocity. (a) $f_g(\omega, f, N)$ for $N^2 = 2.4{\times}10^{-5}$ s^{-2} (b) $f_g(\omega, f, N)$ for $N^2 = 1.5{\times}10^{-6}$ s^{-2}; $N^2 = 3.7{\times}10^{-5}$ s^{-2}, $N^2 = 1.5{\times}10^{-4}$ s^{-2}. See X-axis on top.

in magnitude to be directly measured by a velocity-meter and the horizontal energy fluxes are

$$F_x = \langle u'p' \rangle_\Phi \tag{3.44}$$

$$F_y = \langle v'p' \rangle_\Phi \,. \tag{3.45}$$

Vertical velocities are smaller in magnitude and harder to measure. However, in the near-inertial and hydrostatic frequency range isopycnal displacements ζ can be derived from the linearised density equation in which the incompressibility equation $D\rho/Dt = 0$ becomes

$$\begin{aligned} \frac{\partial \rho'}{\partial t} - \frac{N^2 \rho_0}{g} w &= 0 \\ \frac{\partial b'}{\partial t} + N^2 w &= 0 \,, \end{aligned} \tag{3.46}$$

where the second line is expressed in buoyancy ($b = -g\rho_0^{-1}\rho'$) instead of density. A more intuitive quantity is the vertical displacement ζ of an isopycnal from the average isopycnal depth $\langle z(\sigma_\theta) \rangle$ caused by the internal wave:

$$\zeta = N^{-2} \Delta b. \tag{3.47}$$

This means from an experimental point of view that a continuous measurement of the density profile over many inertial periods can be used to derive the vertical energy flux of internal waves.

The pressure and the corresponding anomaly at a depth z in Eq. (3.43) can, under hydrostatic conditions, be calculated by measuring the density ρ of the water column above z up to the surface ζ and integrate it vertically:

$$p(z) = \int_z^\zeta \rho(z) g \, dz \, . \tag{3.48}$$

Internal-wave energy fluxes based on CTD profiles and velocity measurements or numerical model results were analysed with this approach by e.g. *Holloway* (1996); *Kunze et al.* (2002, 2006); *Nash et al.* (2007); *Palmer et al.* (2008).

3.4.2. Internal wave modes

Here we solve the eigenvalue problem (*Kundu and Cohen*, 2008) for hydrostatic motions in a basin with a flat bottom:

$$\frac{\mathrm{d}}{\mathrm{d}z}\left(\frac{1}{N^2}\frac{\mathrm{d}\Psi_n}{\mathrm{d}z}\right) + \frac{1}{c_n^2}\Psi_n = 0 \, . \tag{3.49}$$

$\Psi_n(z)$ denotes the vertical structure of the horizontal velocities for mode n, and c_n the corresponding "mode speed". The "mode speed" differs from the phase speed if rotation plays a role (*LeBlond and Mysak*, 1978). With the rigid lid boundary condition at the surface and $\mathrm{d}\Psi/\mathrm{d}z = 0$ at the bottom ($z = -H$) and at the surface ($z = 0$), Eq. (3.49) can be solved numerically, yielding the horizontal modes $\Psi_n(z)$ as the eigenfunctions and the speed c_n as the eigenvalues. The advantage of the modal decomposition is that the stratification is allowed to change in comparison with the vertical wavelengths and that the boundary conditions of a bottom and a surface are incorporated. This is probably a more appropriate description of the near-inertial internal wave motions in the Gotland Basin. Examples of internal wave modes are shown in Fig. 7.9.

3.5. Topographic waves

Topographic waves or topographic Rossby waves are a type of wave in which the barotropic potential vorticity is conserved (*Stocker and Hutter*, 1992):

$$\frac{\mathrm{D}}{\mathrm{D}t}\left(\frac{\eta + f}{\zeta + H}\right) = 0 \, , \tag{3.50}$$

where $\eta = \partial v/\partial x - \partial u/\partial y$ is the vorticity, f the Coriolis parameter, H the water depth and ζ the surface elevation such that the total water depth equals $H + \zeta$. D/Dt denotes the material derivative. To derive an evolution equation for topographic waves the mass transport stream function Φ is introduced

$$\frac{\partial \Phi}{\partial y} = -Hu \ , \ \frac{\partial \Phi}{\partial x} = Hv \, . \tag{3.51}$$

Incorporating the stream function the vorticity η reads:

$$\eta = \frac{\partial v}{\partial x} - \frac{\partial u}{\partial y} = \frac{\partial}{\partial x_\alpha}\left(\frac{1}{H}\frac{\partial \Phi}{\partial x_\alpha}\right) \, . \tag{3.52}$$

Φ conserves the vertically integrated mass continuity equation if the rigid lid and the shallow water assumptions are made. The shallow water assumption does also simplifies the conservation

of potential vorticity Eq. (3.50) to:

$$\frac{\mathrm{D}}{\mathrm{D}t}\left(\frac{\eta+f}{H}\right)=0\,. \tag{3.53}$$

Using Eq. (3.52) to rewrite Eq. (3.53) we get:

$$\frac{1}{H}\frac{\partial}{\partial t}\left(\frac{\partial}{\partial x_\alpha}\left(\frac{1}{H}\frac{\partial\Phi}{\partial x_\alpha}\right)\right)-\frac{1}{H}\frac{\partial\Phi}{\partial y}\frac{\partial}{\partial x}\left(\frac{f}{H}\right)+\frac{1}{H}\frac{\partial\Phi}{\partial x}\frac{\partial}{\partial y}\left(\frac{f}{H}\right)=0\,. \tag{3.54}$$

This is the general form of the conservation of the potential vorticity expressed with the stream function Φ. The restoring force is the change of bathymetry or the Coriolis force. Depending on the spatial gradients of the Coriolis force and the bathymetry $\partial f/\partial x_\alpha$, $\partial H/\partial x_\alpha$ several wave types can be derived from Eq. (3.54):

$\partial f/\partial x_\alpha$	$\partial H/\partial x_\alpha$	f	Name
$\neq 0$	$=0$		Planetary Rossby waves
$\neq 0$	$=0$	$=0$	Equatorial planetary Rossby waves
$\neq 0$	$\neq 0$	$\neq 0$	Planetary topographic Rossby waves
$\neq 0$	$\neq 0$	$=0$	Equatorial topographic planetary Rossby waves
$=0$	$\neq 0$	$\neq 0$	Topographic Rossby waves/Topographic waves

Table 3.1.: Wave types of Eq. (3.54).

The last type in Tab. 3.1, the topographic Rossby waves, must be distant from the equator and the north-south size L of the basin should be small enough so that $\partial f/\partial x_\alpha = 0$, or $(\partial f/\partial x_\alpha)L \ll f$. This inequality holds if $L \leq 500$ km. Comparing L with the size of the Baltic Sea shows that the Baltic Proper meets this criterion and the Gotland Basin in particular as well (north-south extent of the Gotland Basin is approx. 100 km). Taking the total north-south extent of the Baltic Sea with (approx. 1600 km) yields in a significant change of f and planetary topographic Rossby waves are thus physically possible as well, but might be strongly damped due to the shape of the Baltic Sea, for example at the beginning of the Gulf of Bothnia. *Fennel and Lass* (1982) assumed that the Baltic Sea can be considered as an infinitely long channel, due to the damping at the northern and southern boundaries. The periods, calculated analytically, of the topographic waves in the channel are estimated between 5 and 7 days, agreeing with recorded spectra. Except for the mentioned infinitely long channel a couple of analytical solutions exist for the topographic wave type of Eq. (3.54) for special cases. *Stocker and Hutter* (1992) review the known analytical solutions including elliptical basins and long channels. Topographic waves have been measured in several lakes and ocean basins, for example in Lake Michigan (*Saylor et al.*, 1980), the Gulf of Riga (*Raudsepp et al.*, 2003) and the Santa Monica Basin (*Hickey*, 1991), which is in size (but not depth) similar to the Gotland Basin. *Shilo et al.* (2007, 2008) investigate the response of wind forcing and wind curl on topographic wave generation.

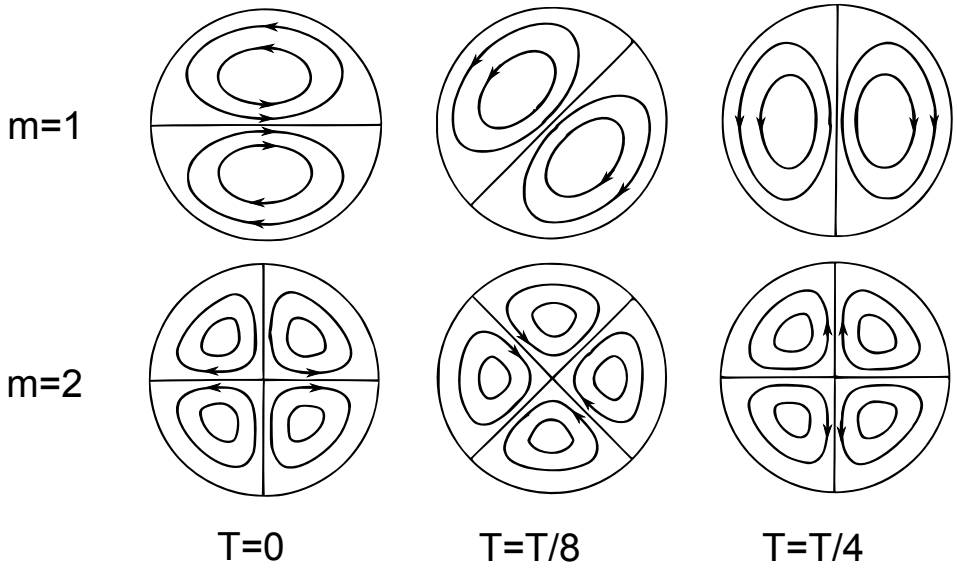

Figure 3.6.: Transport stream function Φ in a spherical basin for the first (upper row) and the second mode (lower mode). Redrawn from *Stocker and Hutter* (1992).

To depict the general properties of topographic waves in a basin, the analytical solution of a spherical basin with a bathymetry as

$$H = H_0 \left(1 - \left(\frac{r}{a}\right)^q\right) , \tag{3.55}$$

is shown here. H_0 is the maximum depth at the centre, a the basin radius and $q > 0$ a parameter characterising the topography profile. The solutions are divided into different modes (m) circulating counter-clockwise around the basin see Fig. 3.6. *Saylor et al.* (1980) deduced for this type of basins the frequency relation

$$\frac{f}{\omega} = \frac{3m + 2q}{m} . \tag{3.56}$$

Note that the period is independent of the size of the basin and is always larger than the inertial period, making topographic waves sub-inertial but depending on the Coriolis parameter f. The period T at the latitude of the Gotland Basin $f = 2\pi/14.3$ h^{-1} for the lowest mode and $q = 1$ is $T = 5f/(2\pi) = 70$ h but is very sensitive to the topography of the basin (*Saylor et al.*, 1980). An interesting phenomenon do show the velocities as well as the integrated velocities at a certain position (pseudo-trajectories). If the location is inside the radius

$$r_c = a \left(\frac{m}{2q + m}\right)^{1/q} , \tag{3.57}$$

$0 < r < r_c$ the velocities rotate counter-clockwise whereas in the region $r_c < r < a$ velocities rotate clockwise (*Saylor et al.*, 1980). An example of the radius r_c and for pseudo-trajectories at 5 locations is given in Fig. 3.7. To derive velocities from the transport stream function Φ (Eq. (3.51)), the spatial derivative of Φ has to be divided by the depth H. This means that a Φ as e.g. shown in Fig. 3.6 in combination with the topography of the basin yields larger velocities at the basin rim, see also the velocity vectors in Fig. 3.7. Larger velocities in shallower water gives a higher frictional resistance, which will damp the oscillation.

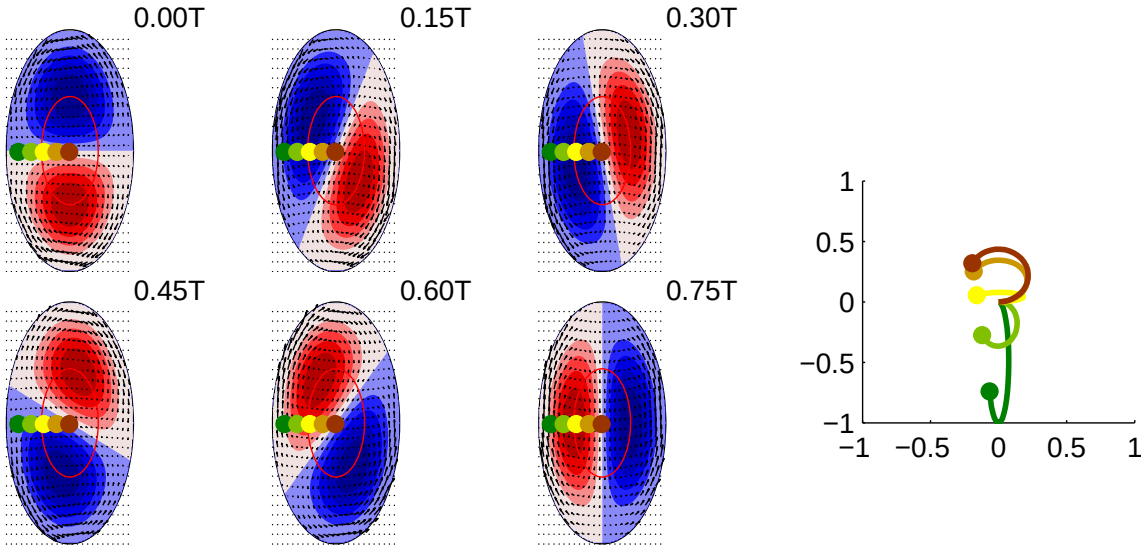

Figure 3.7.: Normalised transport stream function Φ in a spherical basin for a topography with q=1 (colour coded, red positive, blue negative), velocities (arrows) and the locations for the pseudo trajectories calculated shown in the right panel. Times in fractions of one period T are indicated in the upper right. In red the radius r_c. Right plot: Normalised pseudo trajectories. Points indicate the end of the trajectory.

In the context of the Gotland Basin rim current (Chap. 4.2 and Chap. 5.4) it is worth to mention the zeroth mode, which is a steady single circulation cell occupying the whole basin. It can be speculated that the observed basin rim current might be a mode zero topographic wave. As depicted in Fig. 3.8 the velocities strongly depend on the basin topography, a linearly shaped topography ($q = 1$) yields same velocity magnitudes over the whole basin whereas topography with $q > 1$ show an increase of the velocities at the basin boundaries. The topography of the Gotland Basin below 160 m depth can be roughly approximated with $q = 2$ and the basin rim currents shows a decrease towards the basin centre (not shown) as well. A detailed analysis of topographic waves in the Gotland Basin has not been done yet, but, in relation to the rim-current and the spectra of the mooring data, it seems worthwhile to investigate this more. An adequate tool for the analysis would be a numerical model, since some of the assumptions made to derive Eq. (3.54), such as for example a barotropic ocean can be relaxed here and the influence of e.g. stratification can be investigated as well.

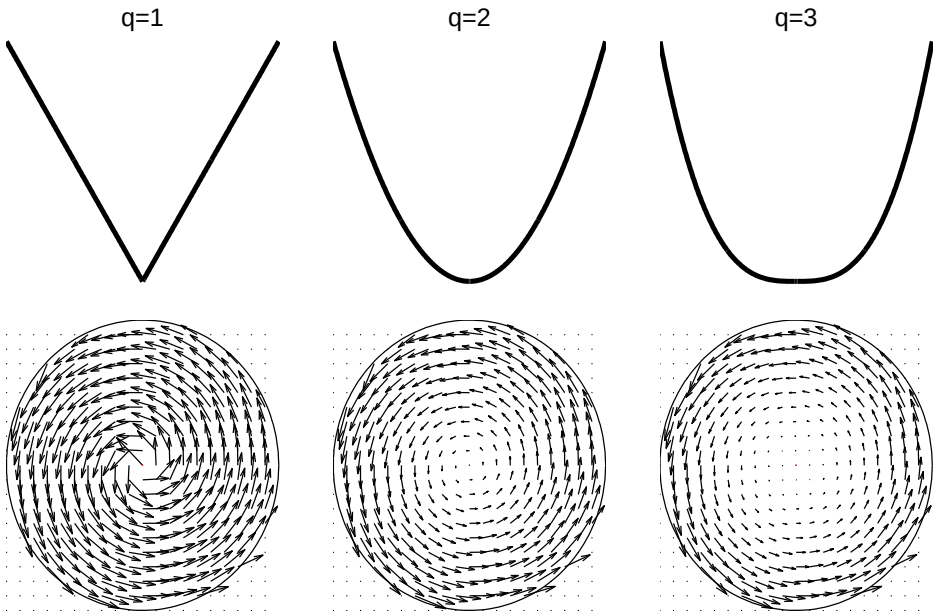

Figure 3.8.: Velocities of the zeroth mode of the topographic transport stream function Φ. Upper row indicates the topography of the circular basin with q varying between 1 and 3 (Eq. (3.55)). Lower row shows the velocities $u = -H^{-1}\partial\Phi/\partial y$, $v = H^{-1}\partial\Phi/\partial x$.

4. The Baltic Sea and the Gotland Basin

4.1. The Baltic Sea

4.1.1. Introduction

The semi-enclosed Baltic Sea is defined by a strong horizontal salinity gradient ranging from 25 g kg^{-1} in the Danish Belts to freshwater conditions in the Gulf of Bothnia. The water balance of the Baltic Sea is positive and consists of 436 km^3 of river input, 224 km^3 precipitation and 184 km^3 evaporation per year. Estuarine circulation as well as inflows, import another 500 km^3 of saline North Sea water into the Baltic Sea. This sums up to 976 km^3 discharging per year into the North Sea (*Reissmann et al.*, 2009). The higher density of the inflowing water and the slow vertical mixing lead to a two layered Baltic Sea, divided by the halocline into the saltier and denser lower part and fresher surface layer. The depth of the halocline differs from basin to basin, the typical depth in the Arkona Basin is 35–40 m and reaches down to 70–90 m in the Gotland Basin. During summer a thermocline in 10–30 m develops and protects the halocline from further erosion. In terms of vertical mixing, the Baltic Sea can be principally divided into two parts: The shallow western Baltic Sea and the deeper basins starting with the Bornholm Basin. The western part can, during strong winds, be vertically mixed down to the bottom, whereas the deeper basins are somewhat decoupled from the winds at the surface with the permanent halocline as the interface between the wind-influenced top and the dense deep water. The bathymetry of the Baltic Sea is dominated by a basin-sill structure (Fig. 4.1). These sills, especially the Darss Sill and the Drodgen Sill hamper the estuarine circulation, but, under certain meteorological situations, significant amounts of salty North Sea water can intrude as inflows into the Baltic Sea. These Baltic Sea inflow events are differentiated between (*Reissmann et al.*, 2009)

Barotropic Inflows are triggered by persistent westerly gales (mostly autumn, winter, spring) which develop a sea level difference between the Kattegat and the western Baltic Sea. This sea level difference is balanced by the inflowing water. The amount of imported salt is typically about 2 Gt in 200 km^3 of water. The imported water is typically oxygen-saturated with a total amount of 1 Mt O_2.

Baroclinic Inflows are driven by horizontal pressure gradients due to the salinity gradients. These happen during calm wind situations (mostly summer) and are less oxygen-saturated. Nevertheless they ventilate the Baltic basins due to entrainment with surrounding water. Since the inflows occur mostly during summer, temperatures of the water are generally higher and a saline but warm inflow can be measured. The inflow directly before the BaTRE project in March 2007 was an example of such an inflow.

Depending on the strength of these inflows, water can reach the deep central Baltic Sea to ventilate and replace the old stagnant water. Such strong inflows are called major Baltic inflows (MBI).

Due to these irregular inflows the study of mixing in the Baltic Sea has two major interests: (i) The mixing and entraining processes during the inflow events themselves. Understanding these

processes is the key to quantify entraining volumes, the amount of oxygen reaching the deeper basins and in which depth levels (defined by the density) the inflowing water will finally level out at. Process studies have been made by e.g. *Umlauf and Arneborg* (2009a,b) to understand entraining in shallow rotating channels. The interaction, the pathways and interleaving of the dense waters with the basin water by *Lass et al.* (2005) and *Burchard et al.* (2009). The second motivation is to be able to assess the environmental impact of man-made structures, like offshore wind parks or bridges, which might be built in the pathway of the inflows (*Lass et al.*, 2008; *Burchard et al.*, 2009).

(ii) Stagnation periods can last up to decades, meaning that the communication between the deeper and the surface water during these periods is solely due to turbulent mixing. This mixing influences nutrient concentrations in the surface water, the transition depth from water with oxygen to water with hydrogen sulphide (redoxcline) and thus has a major impact on the Baltic Sea ecology. A quantification of the mixing rates in terms of a turbulent basin-scale eddy diffusivity, see Chap. 6.5.1 for the equations, has been made for the whole Baltic Sea (e.g. *Matthäus*, 1990; *Reissmann et al.*, 2009) or for single basins (Arkona-, Bornholm-, Gotland-, Fårö-, Landsort-Basin *Matthäus*, 1977), (Gotland Basin and the Landsort Deep *Axell*, 1998). These long-term averages are reasonably well-known but since events such as cyanobacterial blooms occur on shorter time scales, the focus has been shifted to process studies and the quantification of single processes and their contribution to the long-term budget. Process studies for the investigation of basin-scale mixing mechanisms for the deeper basins have been done by e.g. *Lass et al.* (2003) in the Gotland Basin, *Reissmann* (2005) counted the number of Baltic Sea Eddies (Beddies) in several basins and *van der Lee and Umlauf* (2011) investigated near-inertial internal waves and their contribution to mixing in the interior of the Bornholm Basin. A good review about the state of the knowledge in Baltic Sea mixing can be found in *Reissmann et al.* (2009).

4.1.2. Dispersion and mixing experiments using tracers

A number of Rhodamin dye and radar tracing experiments were done in the late 1960s and early 1970s to estimate horizontal and vertical mixing properties. An overview of the locations of the tracer injections is shown in Fig. 4.2 and Tab. 4.1 summarises the Baltic Sea tracer experiments known to the author.

The "Institut für Meereskunde, Warnemünde", the ancestor of the IOW in the former GDR, performed a number of tracer experiments in the south-western Baltic Sea. In summer 1968 several Rhodamin patches were injected into the surface layer and, during the next couple of hours, the horizontal and vertical spreading was measured using a fluorometer. *Brosin* (1972) calculates variances of the measured dye concentration and reported horizontal diffusivities at the surface based on the increase of variance with time. *Brosin et al.* (1972) uses the same database but with a refined analysis and reports horizontal and vertical diffusivities. A different way of studying horizontal diffusivities was used by *Brosin* (1974) who radar-tracked drifters in the south-western Baltic in the surface waters. *Kullenberg* (1972) gives a review of the Rhodamin dye experiments done between 1965–1969 in fjords, coastal and open seas in the Baltic Sea. All experiments mentioned above are constrained to depths not deeper than 30 m and thus the majority of the experiments injected the dye into the surface waters. An analysis of horizontal dispersion of dye, in combination with velocity measurements, was done by *Schott and Quadfasel* (1979) with the attempt to correlate the Lagrangian and the Eulerian time scales which turned out to be similar in the turbulent surface layer but not in depths of 45 m based on data from *Kullenberg* (1977). An argument for the different time scales is the existence of internal waves with much longer correlation times.

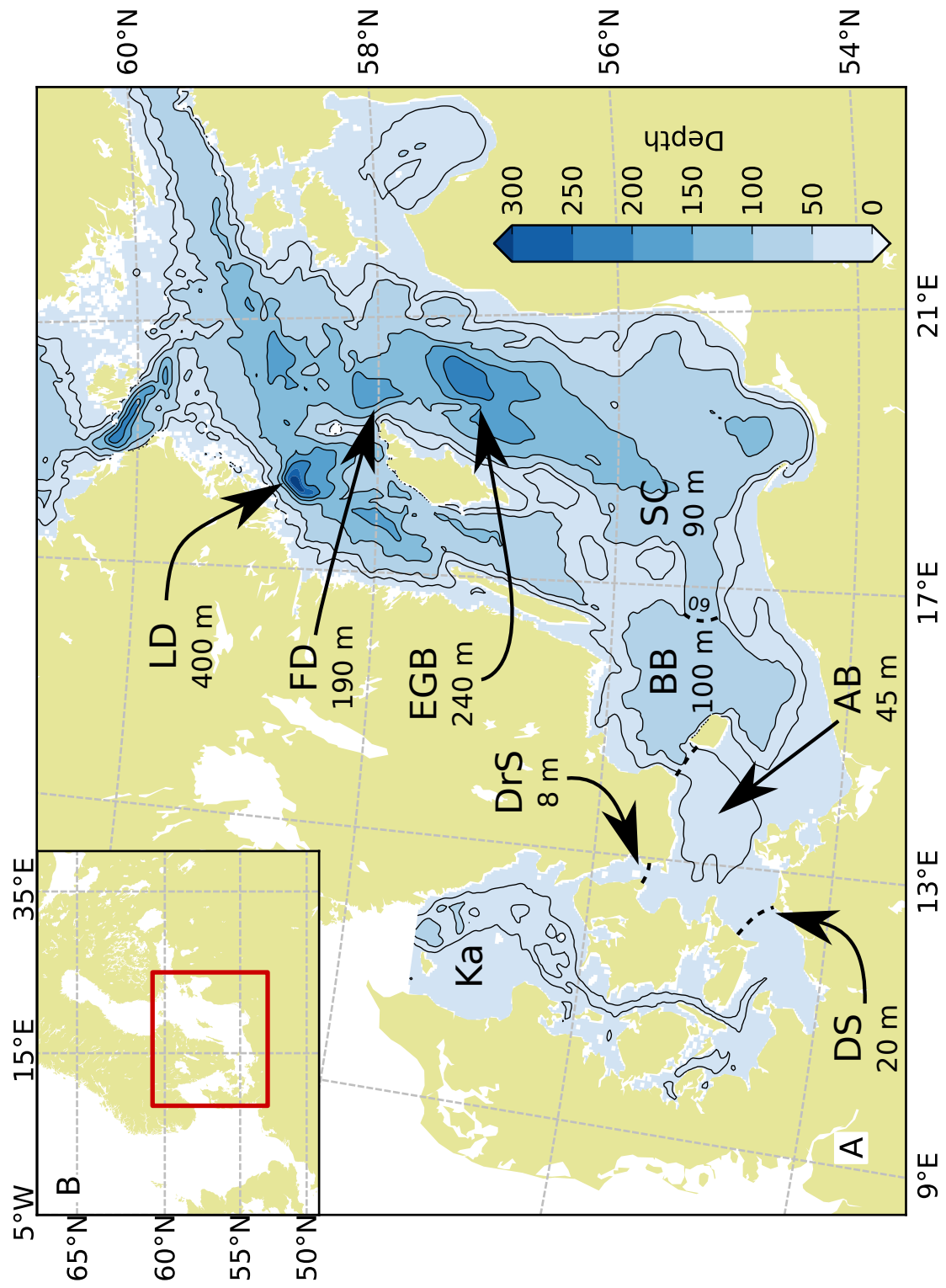

Figure 4.1.: Bathymetry of the western and central Baltic Sea (a), location shown in (b). Names and depth of the Kattegat (Ka), Arkona Basin (AB), Bornholm Basin (BB), Słupsk Channel (SC), (Eastern) Gotland Basin (EGB), Fårö Deep (FD), Landsort Deep (LD). Names and depths of the inflow-constraining sills Darss Sill (DS), Drodgen Sill (DrS).

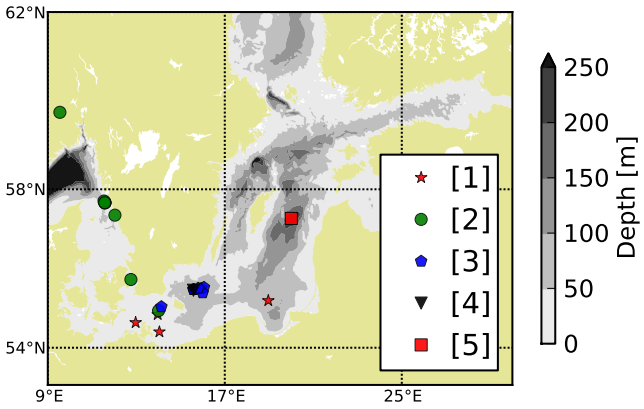

Figure 4.2: Map of tracer injections in the Baltic Sea documented in [1]: *Brosin* (1972), [2]: *Kullenberg* (1972), [3]: *Kullenberg* (1977), [4]: *Schott and Quadfasel* (1979), [5]: BaTRE.

Publication	Duration [h]	Depth [m]	Tracer	Comment
Astok and Ozmidov (1972)	3.5	0	Rhodamin	Permanent Injection Statistics of turbulence
Brosin (1972)	5–9	0	Rhodamin	Horizontal
Brosin et al. (1972)	5–9	0	Rhodamin	Horizontal + Vertical
Brosin (1974)	4–5	0	Drifters/Radar	Horizontal
Schott and Quadfasel (1979)	5–8	0–5	Rhodamin	Horizontal
Kullenberg (1972)	4–17	9–28	Rhodamin	Horizontal
Kullenberg (1977)	8–42	40–55	Rhodamin	Horizontal + Vertical
BaTRE	17500	190	CF_3SF_5	Horizontal + Vertical

Table 4.1.: Overview of published tracer studies in the Baltic Sea. The scope of the experiments is named Horizontal, if horizontal mixing was studied or Vertical, for vertical mixing.

Dye tracer experiments with an emphasis on vertical mixing coefficients were done in the halocline and thermocline of the western Baltic Sea in the years 1969, 1970 and 1977 (*Kullenberg*, 1977). Dye was injected as deep as 80 m, which is also the deepest dye injection known to the author in the Baltic Sea. The BaTRE project is thus the first tracer injection in the Baltic Sea with depths below the halocline.

A different setup was used by *Astok and Ozmidov* (1972) who continuously injected Rhodamin dye in quantities of about 0.2 g s^{-1} into shallow waters near the Peninsula of Zingst and measured the concentration 150 m away from the injection. *Astok and Ozmidov* calculated turbulent spectra and found spectral shapes typical for turbelent flows of concentrations versus wavenumber.

4.2. The Gotland Basin

The study area for all measurements conducted in the framework of BaTRE is the Eastern Gotland Basin (EGB, or Gotland Basin), the largest of the deep basins of the Baltic Sea (Fig. 4.1). Located in the center of the Baltic Proper, the Gotland Basin has a maximum depth of

approximately 240 m, and a lateral scale of the order of 100 km. It is an elliptically-shaped basin in depths below 170 m. The 150 m isobath includes both the Gotland Basin and the shallower south-western side basin (SB), connected via a sill at 165 m depth. Even shallower is a sill at approximately 130 m depth, connecting the Gotland Basin with the Fårö Deep to the north (Fig. 4.3a).

The hydrographic parameters measured on 24 September 2007 represent typical late-summer conditions in the Gotland Basin (Fig. 4.3c). Below the seasonal thermocline at approximately 30 m depth, the stability of the water column is almost exclusively determined by vertical salinity gradients with a particularly stable halocline located around 80 m depth. The slightly increasing temperatures towards the bottom indicate a weak deep-water inflow that occurred in March 2007, approximately six months before the tracer injection (Chap. 5.4). The deep-water stratification and the depth of the permanent halocline are determined by the long-term balance between downward advection of dense (saline) waters by entraining gravity currents during intermittent "inflow events", subsequent interleaving, and vertical mixing (*Reissmann et al.*, 2009). It is worth noting that this conceptual picture is completely analogous to some recent ideas about the evolution of stratification in large-scale ocean basins (*Wåhlin and Cenedese*, 2006) such that the Baltic Sea may be considered a natural laboratory in which these processes can be conveniently investigated.

4.2.1. Review of mixing in the deeper Gotland Basin

The key constraint for vertical transport processes in natural waters, and thus also in the deeper Gotland Basin, is the stratification. Water renewal of the deep bottom water happens only during dense water inflows occurring in intervals of years to decades (*Kouts and Omstedt*, 1993; *Zhurbas and Paka*, 1997; *Feistel et al.*, 2003b, 2006) but with the frequency decreasing (*Feistel et al.*, 2003a). The time between the inflows, the "stagnation period", is characterised by a steady decrease of the bottom water density caused by turbulent vertical fluxes of salinity into the upper water column. Fluxes of oxygen point into the deeper basin due to the oxygen demand for the remineralisation of particulate organic matter. This demand, which is larger than the input from the turbulent fluxes, eventually leads to anoxic deep water conditions. Chap. 4.2.2 gives a small review of the biological and ecosystem aspects of vertical mixing. Based on 50 years of hydrographic data measured in the Gotland Basin and the Landsort Deep *Axell* (1998) could correlate the magnitude of deep water mixing to different seasons. This was already assumed by other authors e.g. *Matthäus* (1977); *Rahm* (1985) and *Matthäus* (1990) since wind is the main energy source for mixing in the Baltic and has a strong seasonal variability, but *Axell* was the first to show this for the deeper Gotland Basin. Turbulent fluxes and diffusivities on the long-term average (>months) have been measured by either budgets of temperature, salinity or density (Chap. 6.5.1) or by measuring the local dissipation rates and applying Eq. (3.21), Chap. 3.2. Several publications about the diffusive fluxes at the top of the Gotland Basin (150 m depth) and within the halocline have been published and it can be stated that the order of magnitude is well-known, see Fig. 4.4 for a depth resolved summary of reported diffusivities in the Gotland Basin. Two general remarks about diffusivities derived from dissipation rates measured with microstructure profilers should be mentioned. (i): It can be simply understood that a point measurement of turbulence might not yield a diffusivity representable for the whole system. This is especially true if boundary mixing processes and a subsequent isopycnal homogenization are important, as it is the case in the deeper Gotland Basin. It is furthermore known that turbulence in the interior occurs in patches of high turbulence and increased mixing rates. This needs a long enough measurement over time to average a certain amount of these mixing events. (ii): The good agreement of the diffusivities of e.g. *Lass*

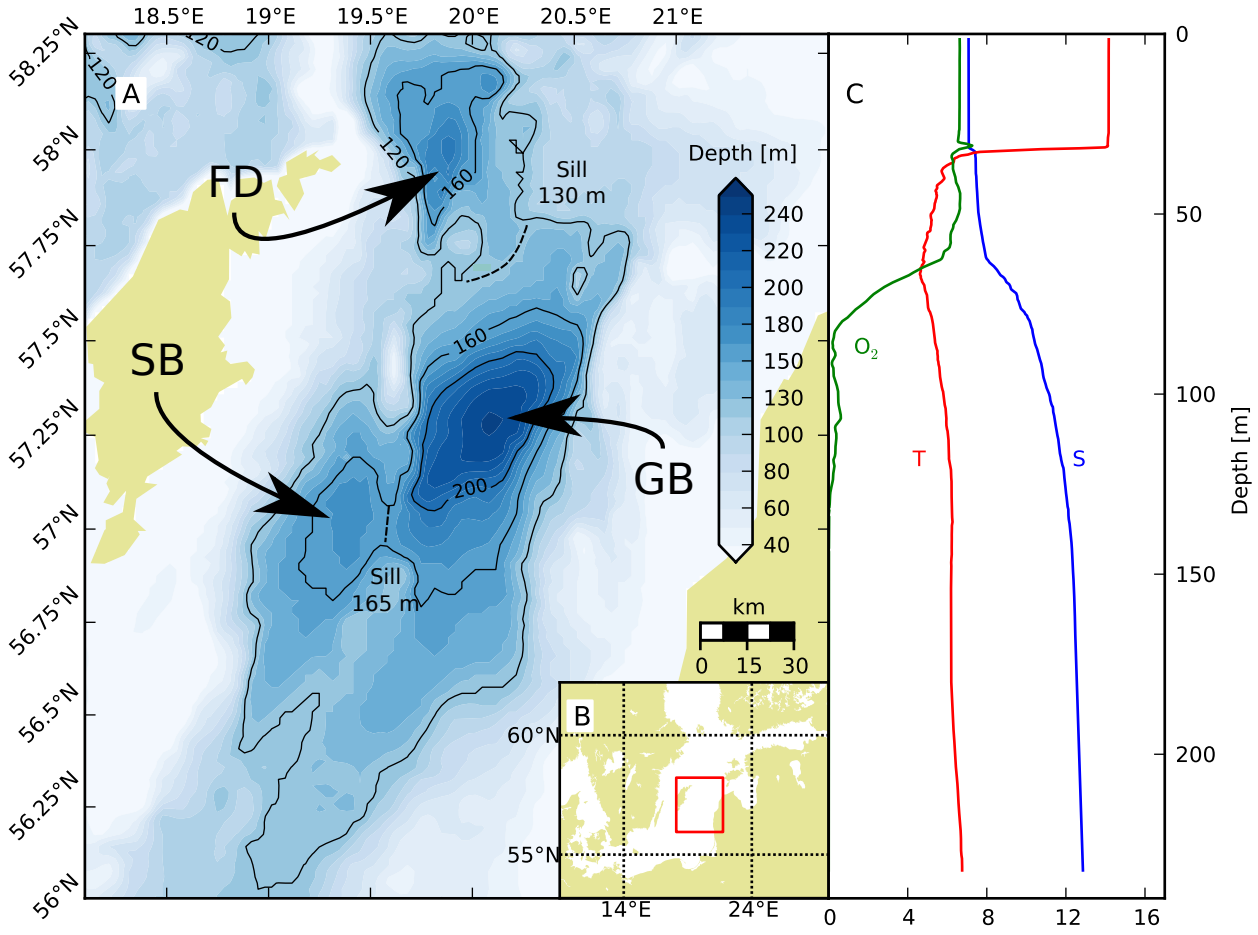

Figure 4.3.: (a) Map of the of the Gotland Basin (GB). Also indicated are the Gotland Side Basin (SB) and the Fårö Deep (FD). Depth intervals of isobaths are 10 m. Location of zoom shown in (b). Note the sill depths GB–SB and GB–FD. Typical summer profiles of temperature [°C] (red), salinity [g kg^{-1}] (blue) and oxygen [ml/l] (green).

et al. (2003) and the budget of *Reissmann et al.* (2009) shown in 70 m, Fig. 4.4, should be interpreted with care. As pointed out in Chap. 3.2 dissipation rates calculated with Eq. (3.21) in anisotropic turbulence can lead to an overestimation of up to a factor of 3 (see also *Thorpe*, 2005). *Gargett et al.* (1984) suggested values of the buoyancy Reynolds number $Re_b = 2.5$, under which turbulence does not produce any buoyancy flux and diffusivities are at the molecular level, in addition to the threshold $Re_b > 200$. These two buoyancy Reynolds numbers are calculated for a typical stratification in the basin centre and are compared to the simultaneously measured dissipation rates ε (Fig. 4.5). Values of Re_b between 2.5 and 200 are called intermediate. As depicted in Fig. 4.5 the dissipation rates in the deeper Gotland Basin are in the intermediate range where anisotropy could be important. Mixing events in e.g. 170 m, the BBL zone as well as the surface layer can be considered isotropic. Having these results in mind it is good to ask whether the measured "background" dissipation rates of $\approx 1 \times 10^{-9}$ W kg^{-1} of the MSS90L profiler might be a consequence of the anisotropy. Using e.g. the reported overestimation factor of up to 3 yields a dissipation rate of 3×10^{-10} W kg^{-1} or a diffusivity of $\kappa = 2 \times 10^{-6}$ m^2 s^{-1} if a typical stratification of $N^2 = 3 \times 10^{-5}$ s^{-2} is assumed. This agrees with the interior diffusivity seen from CF_3SF_5 spreading (Chap. 6). The similarity might be coincidental of course but since it is not known how much the anisotropy influences the dissipation rates and since it has the potential to cause an dissipation rate overestimation, it should at least be considered as a source for the measured background dissipation rates of the coastal MSS profiler in the strongly stratified Baltic Sea. Furthermore, if anisotropy really does contributes significantly to the background level it would not make sense to design better shear sensors since the instrument would still be influenced by the anisotropy. A more promising way would be then to develop anisotropy correction terms. One should keep also in mind, that mixing in the interior occurs during the mixing events in which the buoyancy Reynolds number are at least in the intermediate range and the time average might nevertheless dominated by the dissipation rates of these mixing events.

Since the measured turbulent diffusivities incorporate numerous mixing processes and the processes differ from system to system, the reported diffusivities alone are not more than a database of mixing rates of a certain basin under some condition. Without the comprehension of the underlying mixing processes not much about mixing can be predicted if e.g. weather changes due to climate change. It is therefore crucial to identify the mixing processes. In the virtual absence of internal tides, one of the primary mechanisms for mixing in the ocean is lacking (*Reissmann et al.*, 2009). Internal waves of other types have nevertheless been postulated as an important energy supply for deep-water mixing: *Axell* (1998) speculated that the vertical energy flux of internal waves delivers the energy needed for the observed vertical mixing in the deeper basin. *Axell* (2002) modelled several stagnation periods within the Gotland Basin using a 1-D model coupled with a K–ε turbulence model, where the lack of TKE production below the wind-influenced surface layer was compensated by assuming an additional source of TKE due to internal waves. Nevertheless, he stated that the energy source is not known and other sources might be important as well. The parametrisation of additional TKE was indeed in a quite general form and was simply named the internal wave energy production term. It is shown in this work (Chap. 7) that sub-inertial motions are very likely to have a similar or even more important role in mixing than internal waves. Independent of the origin of the energy source, *Axell* (2002) could achieve reasonable results by adding an additional source of TKE in the upper part due to Langmuir circulation and more important for the deeper layer, a source of TKE distributed over the whole water column. Distorting the deeper basin results is the lack of the hypsography in the 1-D model. To be mentioned is also an assessment of baroclinic inflows based on *Stigebrandt* (1987) originating in the Bornholm Basin with an volume flux of

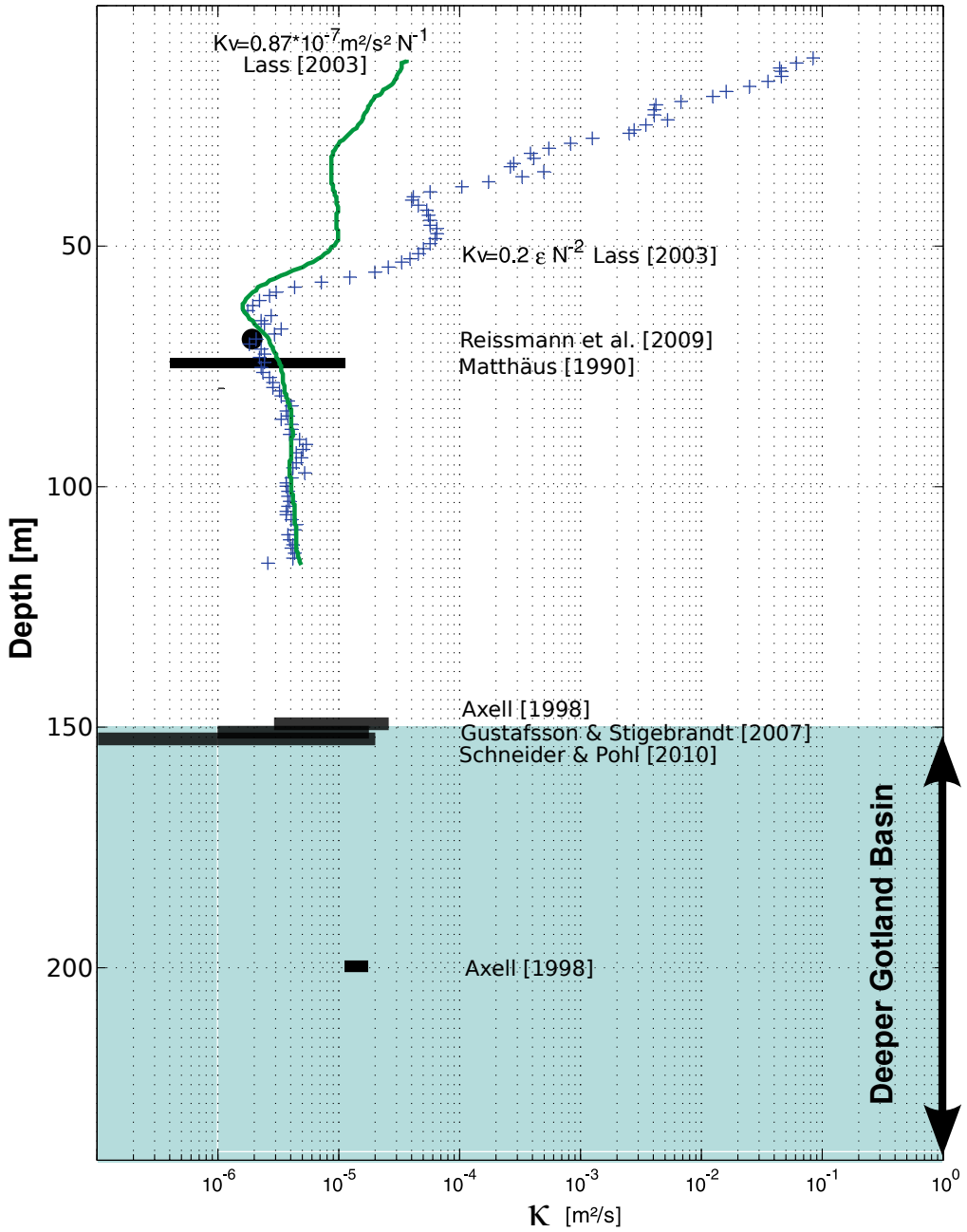

Figure 4.4.: Summary of turbulent diffusivity (κ) publications in the Eastern Gotland Basin. Black symbols indicate values derived from budgets of density, salt or temperature, blue pluses are diffusivities according to Eq. (3.18) derived from microstructure measurements, and the green line represents the fitted function $\kappa = a_0/N$ with $a_0 = 0.87$.

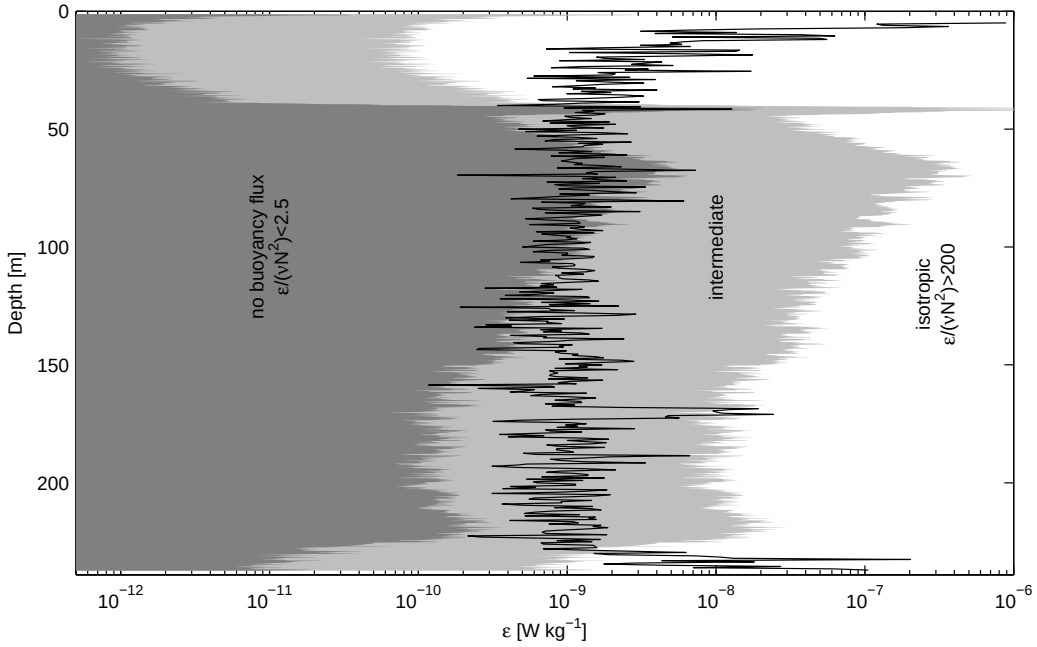

Figure 4.5.: Dissipation rates ε and buoyancy Reynolds number $Re_b = \varepsilon(\nu N^2)^{-1}$ at a central Gotland Basin station measured with a shear microstructure profiler (MSS-90L). Dark gray shaded area indicate an Buoyancy Reynolds number 2.5. White area show an isotropy index above 200. In black measured dissipation rates.

$\approx$ 130000 m^3 s^{-1}. Stressing again that, regardless of the origin, additional energy is required, these results emphasise an energy pathway different from a simple wind-stress produced mean shear transporting TKE into the deepest part of the Gotland Basin. The following processes are known to happen in the Gotland Basin:

Deep rim current The measurements of the NE mooring (*Hagen and Plüschke*, 2009), spanning more a decade, revealed a permanent current of $O(10^{-2})$ m s^{-1} along the isobaths of the basin. This basin "rim current" which accelerates during winter periods (Chap. 7) and during inflows (*Hagen and Feistel*, 2007) probably has a minor contribution to basin scale mixing rates if seen from the bottom stress point of view due to the low current speeds. Due to its permanency it can induce an Ekman transport producing unstable water columns, as it was investigated by *Moum et al.* (2004) on the Oregon continental shelf. Indications for that are reported in Chap. 7.2.2.

Internal waves (IWs) Measurements in the upper 130 m of the Gotland Basin (*Lass et al.*, 2003) clearly indicate near-inertial and internal wave motions and could show upward phase propagation. Energy spectra of the NE mooring in 200 m depth show near-inertial and internal wave oscillations as well (*Hagen and Feistel*, 2004). Despite these measurements, research focus has not been on IWs in the deeper Gotland Basin. IWs probably have a significant contribution to the interior mixing rates. A recent mixing study by *van der Lee and Umlauf* (2011) has explicitly demonstrated the importance of near-inertial waves for mixing in the strongly stratified interior of the Bornholm Basin, outside the turbulent BBLs. The local diffusivities inferred were of the order 10^{-7}–10^{-6} m^2 s^{-1}, too small to explain the basin-scale diffusivities but having the right order of magnitude to explain

the interior mixing rates inferred from CF_3SF_5 spreading. The internal-wave induced BBL mixing is also not quantified, a shoaling of internal waves and possible breaking is reported in *Ozmidov* (1995) but a detailed analysis is missing.

Topographic waves (TWs) TWs in the Baltic Sea have been predicted by *Fennel and Lass* (1982) based on the shape of the Baltic Sea basin. A successful measurement and modelling of TWs was done by *Raudsepp et al.* (2003) in the Gulf of Riga. *Hagen and Feistel* (2004, 2007) report wind-forced barotropic motions with periods of 2 to 5 days and about 10 days and interpreted them as TWs. Whether the motions measured from *Hagen and Feistel* are due to the basin shape of the central Baltic (see *Fennel and Lass*, 1982) or due the to local bathymetry in the Gotland Basin itself (as it was e.g. measured in the Santa Monica Basin by *Hickey*, 1991) is not clear. The high correlation and small phase lag between the moorings in the Gotland Basin point to the larger scale topographic waves.

Double diffusion The baroclinic inflow in 2007 has replaced the deepest water with warmer and saltier water. Colder and fresher over Warmer and saltier water has the potential of double diffusion. As pointed out out in *Wieczorek et al.* (2008) double diffusive contribution on basin scale mixing is probably of second order importance.

Beddies *Reissmann* (2005) quantified the total volume of Baltic Sea Eddies (Beddies) in quasi-synoptic density measurements of several Baltic Sea basins. He concluded that about 12% of the water volume in the Gotland Basin was occupied by Beddies. A crude estimation of the relevance of Beddies for mixing showed that if the salinity contained in the Beddies would be mixed up during their lifetime, Beddies alone could explain the salinity flux through the halocline. Furthermore it was stated that these processes would have to occur at the slopes were the Beddies interact with the boundary. Beddy-mixing would thus be a boundary process. Contrary to *Reissmann*, *Axell* (2002) comes to the conclusion that Beddies are probably of minor importance. A quantification of mixing due to Beddies is still missing but might be investigated in the next years due to the current work on mesoscale numerical models of the Baltic Sea. These models resolve the internal Rossby radius and are therefore capable of simulating Beddies (Ulf Gräwe, pers. communication).

4.2.2. Biological aspects of turbulent mixing

As outlined in the introduction, vertical mixing in the central Baltic Sea has important ecological consequences. Despite the fact that the scope of this work is physical mixing, this section will give a short review of two ecologically important compounds: oxygen and phosphate. The fate of these compounds is directly coupled to vertical mixing, hence the vertical fluxes need to be understood in order to comprehend the ecosystem. A thorough summary of the present knowledge can be found in *Reissmann et al.* (2009); *Feistel et al.* (2008) and *Nausch et al.* (2008a).

It is well known that during stagnation periods the water of the deeper Gotland Basin becomes anoxic. The particular organic matter (POM) produced at the surface sinks into the deeper basin and is remineralised there. The remineralisation depletes the oxygen reservoir in the deeper basin, or, if the oxygen concentration is zero, transforms sulphate into hydrogen sulphide. The discrepancy between the oxygen demand for remineralisation and the supply by turbulent fluxes is used by *Gustafsson and Stigebrandt* (2007) to calculate remineralisation rates of particulate organic matter based on oxygen depletion or hydrogen sulphide increase during 14 stagnation periods between 1950 and 2006. *Schneider et al.* (2002, 2010) used the temporal evolution of CO_2 for the same task. The high oxygen demand of the remineralisation process will thus cause

the Gotland Basin to become anoxic. The only way to re-oxidise the basin is via major Baltic inflows, since, due to its origin in the North Sea, the inflowing water is generally saturated with oxygen. This is especially true for barotropic inflows as e.g. the 2003 major Baltic Sea inflow, but also for the baroclinic summer inflows.

The phosphate concentration in the deeper Gotland Basin is directly related to inflow events and stagnation periods. In the presence of oxygen, phosphate is bound in the form of an iron-III-hydroxophosphate complex on the sediment. Under anoxic conditions this complex is reduced by hydrogen sulphide to phosphate and iron(II) ions. This process increases the phosphate concentration in the deeper Gotland Basin. *Gustafsson and Stigebrandt* (2007) and *Schneider et al.* (2010) calculated a budget of phosphate and could show that, during anoxic conditions, the Gotland Basin becomes a source of phosphate. This phosphate is mixed into the surface layers and can lead, after the depletion of the nitrate pools during the spring blooms, to an excess of phosphate, which favours nitrogen-fixating cyanobacteria and can cause massive blooms as shown in Fig. 2.1 (*Wasmund et al.*, 2001; *Nausch et al.*, 2008b).

5. The Baltic Sea Tracer Release Experiment

5.1. Introduction

Here, the results from the Baltic Sea Tracer Release Experiment (BaTRE) during which deep-water mixing in the Baltic Proper was studied, are reported. Mixing in this part of the Baltic Sea is known to determine the vertical transport of nutrients and dissolved tracer metals from the deep, usually anoxic layers, therefore constituting an essential component of the basin-scale nutrient cycle with considerable implications for ecosystem functioning (*Feistel et al.*, 2008; *Reissmann et al.*, 2009). Previous studies have shown that some information about the effective basin-scale diffusivities may be inferred from the construction of deep-water budgets for heat and salt (e.g. *Axell*, 1998), for O_2, PO_4 and NH_4 (*Gustafsson and Stigebrandt*, 2007), and for CO_2 (*Schneider et al.*, 2010). These methods, however, involve large uncertainties introduced by the implicit assumption that deep-water renewal due to advective effects ("inflow events") is negligible, or by additional model assumptions associated with the non-conservative properties of some of the tracers.

Besides the problem of a precise quantification of the deep-water mixing rates, approaches based on the construction of volume-averaged deep-water budgets are, by their nature, not a useful tool for identifying mixing processes and flux pathways of matter. In spite of numerous suggestions, see Chap. 4.2.1 for a review of processes discussed in the literature, these processes are at the moment only poorly understood.

The BaTRE project was therefore designed such that the mixing rates in the Gotland Basin could be measured using different techniques and to identify key mixing processes. This does of course include the "classical" budget method but only as one of the methods. A major part of the BaTRE project is centred around the release of CF_3SF_5 and BaTRE stays therefore in the tradition of Tracer Release Experiments (TREs) conducted with the long-term stable compounds SF_6, and more recently CF_3SF_5, which have evolved over the last two decades as an interesting alternative technique for quantifying the integral effect of mixing in the ocean and in lakes (*Watson and Ledwell*, 2000; *Ho et al.*, 2008; *Ledwell et al.*, 2011). Beyond the diapycnal and isopyncal mixing rates that can be inferred from the spreading behaviour of the tracer, in many cases TREs have also helped identifying the physical key processes responsible for mixing. Examples are the TREs conducted in stratified ocean basins (*Ledwell and Bratkovich*, 1995; *Ledwell and Hickey*, 1995) and lakes (*Goudsmit et al.*, 1997) that have shown strong, although indirect, evidence for the importance of boundary mixing processes. The turbulent mixing in the energetic bottom boundary layers (BBLs) on sloping topography is believed to be one of the primary vertical transport mechanisms in stratified lakes and ocean basins (*Wüest and Lorke*, 2003; *Thorpe*, 2005). The physical processes responsible for boundary mixing have been shown to be largely different, depending on the size of the basin and other factors. While in oceanic basins the near-critical reflection of internal tides (e.g., *Rudnick et al.*, 2003; *Nash et al.*, 2007) and the shoaling and breaking of solitary waves (e.g., *Pingree et al.*, 1986; *Moum et al.*, 2003) are assumed to be two of the key processes, studies in lakes suggest that standing internal waves (internal seiches) are one of the main energy sources of mixing in the BBL (*Goudsmit et al.*, 1997; *Wüest et al.*, 2000; *Becherer and Umlauf*, 2011).

The analysis of the BaTRE dataset is split into two parts, of which the first (Chap. 6) contains mainly the results of the tracer experiment, and the analysis of the basin-scale mixing rates. The physical processes responsible for the observed mixing rates are analysed in the second part, Chap. 7. A brief description of the tracer injection may be found in *Umlauf et al.* (2008).

The general concepts of the design outline of BaTRE are given in Chap. 5.2 including mooring locations and tracer survey dates. Chap. 5.3 gives a resume of the instrumentation used for tracer sampling, dissipation rates measurements and the mooring instruments used in the project.

5.2. Design of the BaTRE project

The three main questions raised in the BaTRE project are

1. How large is the diapycnal mixing?
2. Where does diapycnal mixing occur?
3. What are the processes of diapycnal mixing?

With regard to the results found from experiments in lakes (e.g. *Goudsmit et al.*, 1997) and ocean basins (e.g. *Ledwell and Watson*, 1991), where it could be shown that the mixing rates in the interior of the water volume differ significantly from the mixing rates at the boundaries, the location of the tracer injection was chosen to be in the centre of the basin and in the middle of the deeper basin, at approx. 200 m depth, which is 40 m above the bottom and 30 m below the sill to the Gotland Side Basin. This ensured that the water masses marked by the tracer would first be affected by interior mixing processes and later in the experiment additionally by boundary processes. The requirements of the BaTRE projects are that at a certain point in time the tracer is dispersed in the whole deeper Gotland Basin basin. The minimal amount of CF_3SF_5 to be injected can then be calculated by taking the volume of the Gotland Basin below 150 m ($\approx 150 \times 10^9$ m^3) and multiplying it with the detectable concentration reported by *Ho et al.* (2008): $8.0 \times 10^{-13} \cdot 150 \times 10^9 = 0.12$ mol (24 g) CF_3SF_5. Taking into account (i) vertical mixing processes and (ii) the, before this study unknown response of CF_3SF_5 to anoxic conditions it was decided to inject 900 g. This was a trade-off between having an always easily detectable concentration in the deeper Gotland Basin and keeping the concentration low enough as to not disturb future tracer releases with the "old" BaTRE tracer.

The mooring locations were based on previous research, suggesting the presence of a persistent cyclonic boundary current (*Hagen and Feistel* (2007)), 3 moorings referred to as NE, NW, and SE in the following were therefore located on the 220 m isobath along the perimeter of the basin, Fig. 5.1. In the counterclockwise direction the current would encounter them, they are referred to as the NorthEast (NE), NorthWest (NW), and SouthWest (SW) moorings. These boundary stations were complemented by 2 central moorings, C1 and C2, located near the deepest point of the basin. For the detection of possible dense water inflows, the A1 mooring upstream of the Gotland Basin was deployed. All mooring locations and deployment times are summarised in Tab. 5.1.

To take the different seasons of mixing activity into account tracer surveys were planned such that winter and summer conditions were sampled and the maximum time difference between two cruises did not exceed 6 months (see Tab. 5.2 for date of surveys). An overview of the available mooring, tracer and microstructure data can be found on the timeline of the BaTRE project, Fig. 5.2.

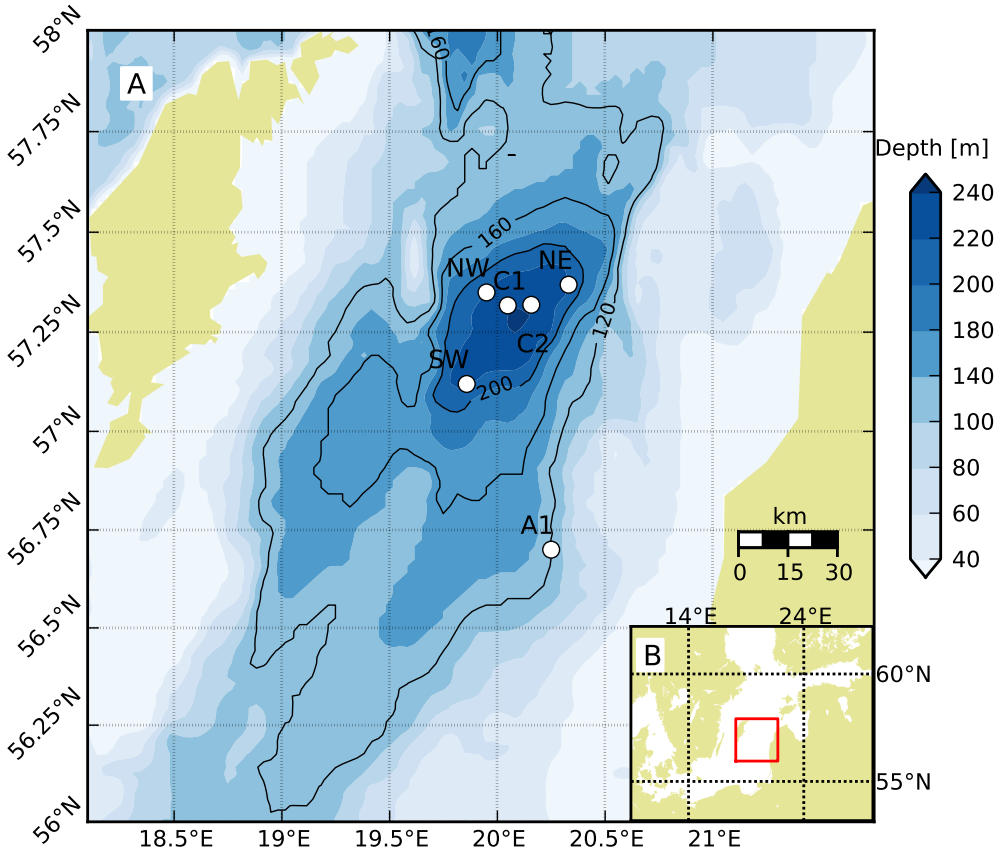

Figure 5.1.: Map of the mooring locations deployed during the BaTRE project.

	A1	C1	C2	SW	NW	NE
Lat [°N]	56.700	57.317	57.319	57.120	57.350	57.369
Lon [°E]	20.251	20.050	20.159	19.859	19.951	20.332
Depth [m]	128	237	233	220	220	220
Start	11 Sep 2007	11 Sep 2007	01 Nov 2005	11 Sep 2007	11 Sep 2007	27 Sep 2006
End u,v	30 Jul 2008	08 Feb 2008	31 Oct 2007	18 Aug 2008	20 Nov 2008	22 Oct 2009
End T,S	29 Mar 2011	26 Jun 2008	-	18 Aug 2008	16 Feb 2009	-
Rec. days u,v	325	150	729	342	436	1121
Rec. days T,S	1297	289	-	342	524	-

Table 5.1.: Locations, deployment depths and record lengths of the moorings.

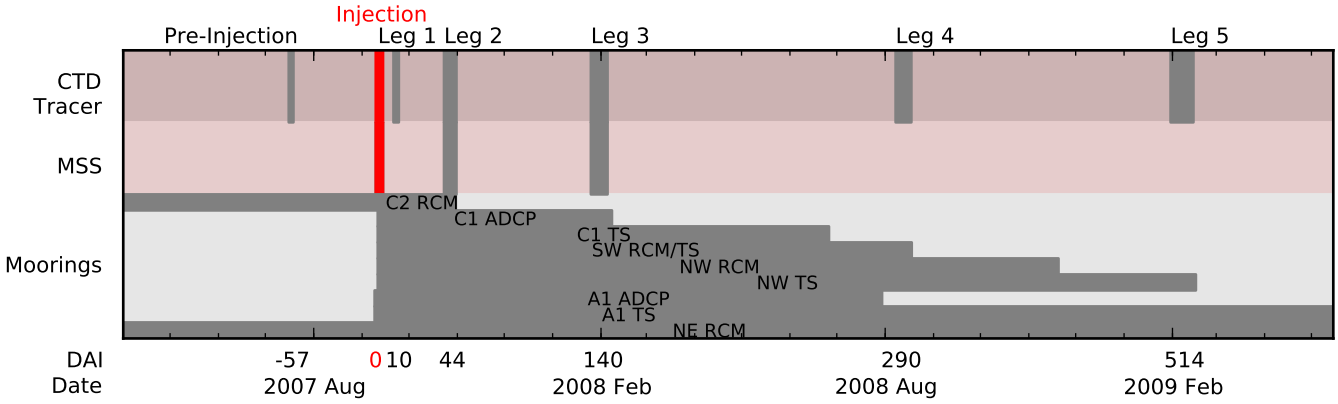

Figure 5.2.: Timeline of the BaTRE cruises with the type of measured data as well as the available data of the moorings listed in Tab. 5.1. Days after injection (DAI), are days after 11 Sep 2007 and the first CTD measurement within the Gotland Basin, respectively. A summary of the tracer surveys is given in Tab. 5.2.

Survey	Cruise	Vessel	Date	CTD	CF_3SF_5	MSS
Pre-Injection	P353	RV Poseidon	16 Jul – 19 Jul 2007	4	39	–
Injection	P357A	RV Poseidon	09 Sep – 14 Sep 2007	40	1	226
Leg 1	P357B	RV Poseidon	21 Sep – 24 Sep 2007	PCTD	PCTD	–
Leg 2	PE0725	RV A. Penck	25 Oct – 31 Oct 2007	64	363	234
Leg 3	AL312	RV Alkor	28 Jan – 05 Feb 2008	32	429	97
Leg 4/1	MSM0803	RV Merian	27 Jun 2008	5	22	–
Leg 4/2	P370	RV Poseidon	09 Aug – 15 Aug 2008	3	22	–
Leg 5	AL331	RV Alkor	05 Feb – 09 Feb 2009	33	242	–

Table 5.2.: Summary of the BaTRE cruises. Dates include only the duration of actual measurements in the Gotland Basin. Last three columns indicate the number of CTD stations, tracer samples, and microstructure casts with the MSS profiler, respectively.

5.3. Oceanographic Instrumentation

5.3.1. Ship-based Instrumentation

On all cruises, except for the first tracer survey, tracer samples were taken with 10 l free-flow bottles from Hydrobios, attached to a standard CTD rosette. O-rings were removed from the bottles, cleaned in isopropanol, and degassed in a vacuum-oven prior to use due to a possible affinity of the tracer for rubber materials. Hydrographic variables were obtained using a Seabird SBE-911plus CTD package, which, on all but the one cruise, was equipped with freshly-calibrated double sensors for temperature and conductivity, except for the injection cruise where only single C, T sensors were available. The accuracy of the sensors is 0.001 °C for temperature and 0.001 g kg^{-1} for salinity.

During the first tracer survey, when the tracer distribution was still very streaky, we used a Pump-CTD system for the tracer sampling. The Pump-CTD consist of a small CTD frame (without rosette), equipped with double SBE-911plus sensors from Seabird, and a high-pressure pump connected to the on-board wet lab via a nylon hose embedded in a multi-function cable; details in *Strady et al.* (2008). This instrument was towed behind the ship at a specified density level, thus providing a continuous stream of water samples representing the isopycnal distribution of the tracer. In combination with the equilibrator system for online tracer analysis described in Chap. 5.3.3, this turned out to be a useful tool for the detection of intermittent tracer patches during the initial stages of the experiment.

Dissipation rates and other mixing parameters were estimated from shear microstructure profiles obtained with a free-falling (sinking speed: 0.5-0.7 m s^{-1}) MSS-90L microstructure profiler from In Situ Wassertechnik (ISW, Germany). In addition to two PNS06 airfoil shear probes, the MSS-90L is equipped with precision CTD sensors from Sea & Sun Technology (SST, Germany), and a FP07 fast thermistor. All sensors were sampled at 1024 Hz, digitised with 16 bit resolution, and transferred online to the computer. After despiking, all data were averaged to 256 Hz resolution for noise reduction, and temperature and conductivity data were corrected for different sensor response times. A sensor protection cage allowed us to sample turbulence also inside the turbulent bottom boundary layer (BBL) down to approximately 0.1 m above the sediment. Dissipation rates were obtained by integrating vertical shear spectra over half-overlapping 256-point Hanning windows (corresponding to 1-s segment length in time, or 0.5–0.7 m in depth), assuming local isotropy in the dissipative subrange. The upper wave number for integration was found iteratively as a function of the Kolmogorov wavenumber with a correction for lost variance due to unresolved scales (see e.g. *Moum et al.*, 1995). Dissipation rates estimated with this method from both shear probes were averaged into non-overlapping bins of 0.5 m thickness. The noise level of this coastal profiler is of the order of 10^{-9} W kg^{-1}, which is sufficient to resolve turbulence in the BBL but often too large to obtain reliable estimates in the quiescent interior. The implications of this will be discussed in more detail below.

5.3.2. Tracer sampling technology

Tracer and injection system

The tracer used in BaTRE is trifluoromethyl sulphur pentafluoride (CF_3SF_5), a compound selected as a replacement for SF_6 that has traditionally been used in ocean tracer injection experiments (*Ho et al.*, 2008). The main motivation for the use of CF_3SF_5 in tracer release experiments is to avoid contaminating the ocean with deliberately released SF_6 to ensure that this tracer can still serve as an oceanic transient tracer in the future, with the atmosphere as

the only source (in Chap. 3.1, Page 11 the total amount of SF_6 dissolved in the world oceans is listed). The physical and chemical properties of CF_3SF_5 are summarised in *Ho et al.* (2008).

In a pilot study in the Santa Monica Basin off the Californian coast recently described by *Ho et al.* (2008), a mixture of SF_6 and CF_3SF_5 was injected. Nearly identical spreading rates of the two tracers were observed, suggesting CF_3SF_5 as a viable alternative to SF_6 in oceanic tracer experiments. Moreover, in the absence of any significant natural and industrial sources, or any previous tracer experiments with CF_3SF_5, we expect that before BaTRE the background concentrations of CF_3SF_5 were below the detection limit everywhere in the Baltic Sea. We have explicitly verified this by measurements of profiles from 3 stations in the Gotland Basin sampled on 16-18 July 2007, i.e. about 2 months prior to the injection of the tracer. None of the samples from the pre-injection survey showed any trace of CF_3SF_5.

For the tracer injection, we used a towed Ocean Tracer Injection System (OTIS), similar to the instruments described for previous tracer studies (*Ledwell and Bratkovich*, 1995; *Ledwell et al.*, 1998; *Ho et al.*, 2008; *Ledwell et al.*, 2011). With the help of OTIS, the tracer was sprayed in the form of liquid droplets through 25 μm orifices into the water column, while the instrument frame was towed behind the ship at approximately 1 knot. Online transmission of data from Seabird CTD loggers allowed us to keep the instrument inside a narrow pre-defined density range. Outside of this range, e.g. during the descend to the target density, an inert primer fluid (Vertrel XF) was slowly flushed through the orifices in order to avoid clogging.

5.3.3. Analytical systems for tracer analysis

The tracer measurements were generally performed on the ship by up to 3 purge and trap gas chromatographic measurement systems similar to the one described in *Bullister and Weiss* (1988) but modified in the following way to optimise the analysis of CF_3SF_5. Due to the presence of H_2S in the water column, we used a column filled with Ascarite after the desiccant to scrub the H_2S out of the gas flow, which would otherwise obscure the tracer peaks in the chromatogram. For trapping we used a 12 cm long 1/8" SS tube packed with Heysep D cooled to -30°C, followed by desorption at 120°C onto a 30 cm long Porasil C 1/8" pre-column. The CF_3SF_5 and CFC-12 were passed on to the main column; 180 cm Carbograph 1AC (60-80 mesh) followed by 20 cm Molsieve 5A. Detection was performed on an Electron Capture Detector. Standardisation was done by injection of gaseous standards calibrated using a commercial standard (accuracy claimed by the company is 10 percent). The CFC-12 data were used to check for incorrectly closed Niskin bottles or other analytical problems; large deviations of the CFC-12 concentration from the bulk of the samples normally indicated a problem, and the CF_3SF_5 values were flagged accordingly. During the surveys where we brought the instruments to sea (Legs 1, 2, 3 and 5) water samples were collected, using ground-glass syringes, either from the free-flow Niskin bottles or from the continuous flow of the Pump-CTD. For the pre-injection survey and surveys 4/1 and 4/2 approximately 120 ml samples were collected in 150 ml glass ampoules that were flame sealed on the ship and later measured in the institutes' labs. For Leg 1 we additionally used a shower head equilibrator connected to the continuous flow from the Pump-CTD from which a flow rate of approximately 2 l/min was maintained through the equilibrator. Every 6 minutes a 12 ml sample of the circulating air was drawn from the equilibrator, which was trapped, desorbed and analysed as a normal standard on the gas chromatograph. The equilibrator proved to be an excellent indicator for the presence of tracer in the waters along the cruise-track. However, due to the large carry-over effect of the equilibrator, this set-up was a poor indicator for when we left the tracer patch. During Leg 1, the equilibrator was complemented by two analytical systems to measure discrete samples each with a 12 minutes interval. This meant that we were able to get a measurement roughly every 6 minutes along the cruise track. During survey 2 and 5 we

	C1	C2	SW	NW	NE	A1
RCM 7/9	-	-	170	170	170	-
(u,v,T)	-	189	189	189	-	-
	-	-	200	200	200	-
	-	-	210	210	-	-
	-	-	215	215	215	-
MC/SC	147	-	-	-	-	126
(T,S)	167	-	-	-	-	-
	187	-	189	190	-	-
	207	-	211	211	-	-
	227	-	-	-	-	-
	236	-	-	-	-	-
ADCP	185.5	-	-	-	-	102
(u,v)	187.5	-	-	-	-	...
	...	-	-	-	-	126
	221.5	-	-	-	-	128

Table 5.3: Mounting depths [m] of the instrumentation used in the moorings listed in Tab. 5.1. MC and SC corresponds to MicroCat and SeaCat CTD loggers from Seabird, respectively.

used 1 analytical system on-board, and during survey 3 we had 3 analytical systems on-board.

5.3.4. Mooring Instrumentation

The two boundary moorings NW and SW were equipped with 5 RCM-7 current meters from Aanderaa, recording vector-averaged currents and temperature every 60 minutes, and two Seabird MicroCats (SBE-37) recording temperature and salinity every 10 minutes. Mooring NE was part of the institute's long-term monitoring program with a nearly continuous data record since 1999 (*Hagen and Plüschke*, 2009). Measurements include vector-averaged currents and temperatures every 60 minutes with Aanderaa RCM-9 current meters at three different depths (Tab. 5.3).

The central mooring (C1) with the highest vertical resolution, but shortest time series, was equipped with 6 Seabird SeaCat (SBE-16) loggers, recording conductivity and temperature every 10 minutes at regularly spaced levels between the bottom and 145 m water depth (Tab. 5.3). The currents in the lower water column at C1 were recorded every 30 minutes from the average of 150 sub-pings in 2-m bins with a downward-looking 600-kHz ADCP (RDI Workshorse) mounted in 185 m water depth. Due to the weak target strength, reliable velocity estimates could be obtained only between 189 and 220 m depth. Future research may profit from our finding that, for the typical deep-water distribution of acoustic scatterers in this region, high-frequency ADCPs are required to obtain acceptable noise levels (for this reason, the full-depth velocity estimates from a 75-kHz long-range ADCP located nearby turned out to be unusable).

Temperature and vector-averaged velocities were recorded every 30 minutes at a second central mooring, C2, in 178 m using an Aanderaa RCM-7 current meter attached below a sediment trap. This mooring provides a long-term dataset that will be used in the following to illustrate the timing of warm-water intrusions in the months before the tracer release. Unfortunately, however, this current meter flooded just a month after the tracer was injected.

The A1 mooring consisted of a SBE-37 MicroCat and an upward looking 600-kHz RDI Workhorse ADCP measuring water velocities every 30 minutes in 2-m bins.

5.4. Hydrography

The stratification in the Gotland Basin during BaTRE was dominated by a permanent halocline located between 60 and 70 m depth, and a seasonally evolving thermocline of variable depth as illustrated in Fig. 5.3. Two processes of the cycle between advective inflows and subsequent turbulent mixing (Chap. 4.2) are immediately evident from the salinity and temperature profiles displayed in Fig. 5.3. The deeper location of the halocline in March 2007 compared to September (Fig. 5.3a) is a result of enhanced entrainment at the mixed-layer base during the winter months (*Reissmann et al.*, 2009), whereas the slight increases of salinity, temperature, and density in the near-bottom layer indicates the presence of a deep-water inflow event in the period between March and September 2007 that may have lifted the halocline. In a more detailed view, Figs. 5.4a,b illustrate an increase in salinity of approximately 0.3 g kg^{-1}, and a temperature increase of up to 0.8 °C. The latter leads to an inversion of the deep-water temperature gradient that is, however, neither sufficient to destabilise the water column (Figs. 5.4c,d), nor to result in any significant double-diffusive processes (diffusive convection) since the ratio of the density gradients caused by temperature and salinity is vanishingly small (see *Wieczorek et al.*, 2008).

As a measure for vertical stratification, we computed the squared buoyancy frequency, $N^2 = -g/\rho_0\, \partial\sigma_\theta/\partial z$, from vertically filtered profiles of the potential density σ_θ, where g and ρ_0 denote the acceleration of gravity and a constant reference density, respectively, and z is the vertical coordinate (positive upward). Mean values below 190 m increase from $N^2 = 1.25 \times 10^{-5}$ s^{-2} before the inflow event to $N^2 = 3.2 \times 10^{-5}$ s^{-2} directly afterwards, the latter value corresponding to a buoyancy period of approximately 18 minutes below which no internal wave motions are expected (Fig. 5.4d). Routine observations in the Western Baltic (*Nausch et al.*, 2008a) suggest that the water arriving in the deep Gotland Basin in April 2007 had its origin in the warm bottom waters in the prelocated (western) basins which were uplifted by a near-bottom intrusion of warm North Sea waters entering the Western Baltic in summer 2006.

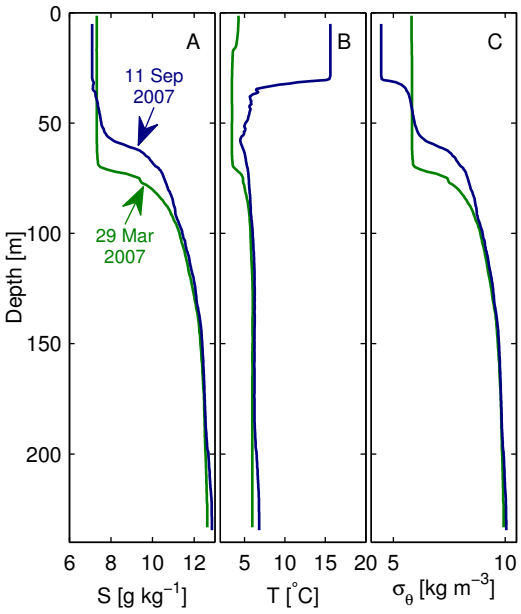

Figure 5.3.: Vertical profiles of (a) salinity, (b) temperature, and (c) potential density. All profiles are taken at station C1 (see Fig. 5.1a) at the dates indicated in the figure.

A more precise determination of the arrival time of the inflow is obtained from the temperature record in 215 m depth at mooring NE displayed in Fig. 5.5a. In April 2007, a strong temperature increase from 5.8 °C to up to 7.0 °C is observed, indicating an important change in the deep-water properties associated with the inflow event. During a period of nearly 2 years following this event, no comparable increase in temperature is observed, and both temperature and its variance slowly decrease until the end of the deployment in February 2009 (Fig. 5.5a). A similar decay is observed at mooring NW, deployed during the tracer injection in September 2007 (Fig. 5.5a), and mooring SW (not shown for clarity). Thus, by lucky coincidence, the tracer injection on 11 September 2007 and the subsequent spreading of the tracer cloud described in Chap. 6 occurred

under ideal conditions during a stagnation period directly following a strong inflow event.

From the physics of rotating bottom gravity currents (*Wåhlin and Cenedese*, 2006; *MacCready*, 1994) it is expected that dense fluid entering the Gotland Basin from the south moves cyclonically along the topographic slope with a small descent rate depending on the relative importance of friction and rotation. Dense bottom waters will therefore be detected first at the boundary moorings NE, NW, and SW (in this order) before they detach from the boundary and intrude into the central part of the basin at their equilibrium depth. This is consistent with the observation that the temperature increase at the central station C2 is delayed with respect to the boundary station NE (Fig. 5.5a,b), and with the sporadic occurrence of temperature spikes at C2 that can be interpreted as manifestations of small-scale intrusions that have detached from the bottom gravity current, and pass the mooring site.

Deep-water warming at C2 stopped in August 2007, suggesting that at that time the last remnants of the inflow reached the centre of the basin and the stagnation period started. It is thus tempting to interpret the continuous decrease of temperature fluctuations observed over the following 18 months at both the central and the boundary stations (Figs. 5.5a,b) as an indication for the decay of some "unrest" in the temperature field generated by the inflow event. A closer examination, however, reveals that the observed temperature fluctuations are almost exclusively related to vertical isopycnal displacements that follow a clear seasonal pattern (see below) rather than being triggered by the inflow event. The reason why these displacements are mirrored less and less in temperature fluctuations is the gradual vanishing of the temperature gradient between 178 and 208 m (Fig. 5.5b).

Due to the lack of moored conductivity sensors in the period before the tracer injection, the evolution of the deep-water salinity during the inflow event is not well-resolved in time. However, consistent with temperature records at station C2 in the centre of the basin (Fig. 5.5b), CTD measurements suggest that the inflow event terminated by the end of August 2007 when maximum salinities around 12.8 g kg^{-1} were reached (Fig. 5.5d). CTD loggers at the boundary stations NW and SW, and the central station C1, available in the period following the tracer injection in September 2007, illustrate the long-term decrease of the averaged deep-water salinities (and thus densities) due to mixing. Clear indications for reduced decay rates during the summer months, visible in all records, provide a first hint towards a seasonality of mixing (Fig. 5.5c,d). The longest available record at station NW (Fig. 5.5c), illustrates a renewed increase

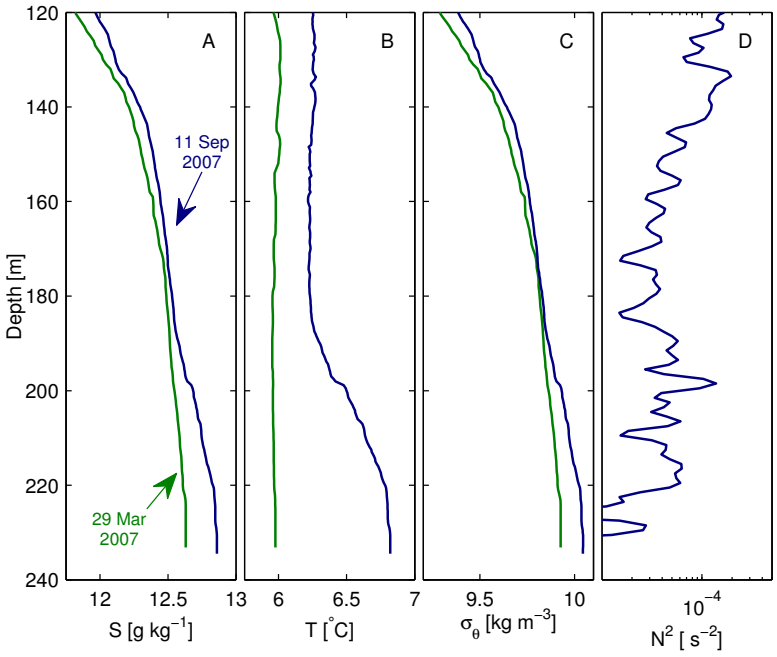

Figure 5.4.: Enlarged view of the deepest half of the vertical profiles shown in Fig. 5.3. Panel (d) shows the square of the buoyancy frequency (4-m low-pass filtered) for the profile from 11 September 2007.

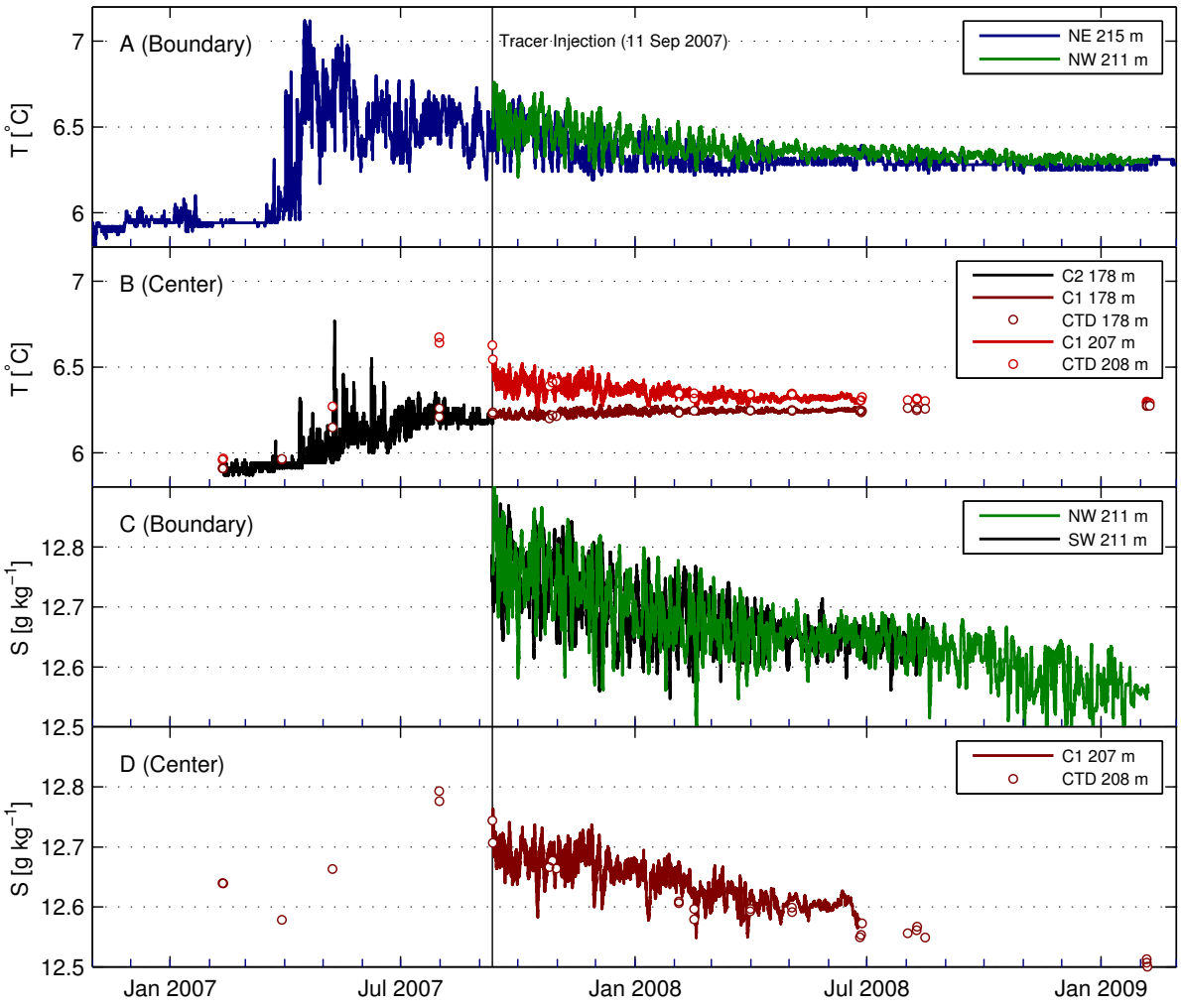

Figure 5.5.: Time series of temperature (a, b) and salinity (c, d) obtained at the mooring positions shown in Fig. 5.1 (depth levels as indicated). Circles in (b) and (d) correspond to data obtained from individual CTD casts. The vertical line marks the time of the tracer injection in approximately 200 m depth.

of salinity variance and decay rates in the following fall/winter season.

The triggering mechanism for these seasonal patterns is most likely related to the strong seasonal variation in the surface momentum flux that is proportional to the square of the local wind speed, $|\mathbf{U}_W|^2$, displayed in Fig. 5.6a. The 30-day low-pass filtered $\langle \mathbf{u} \rangle_T$, which was rotated parallel to the isobaths $\langle u_{||} \rangle$, reveals that the cyclonic rim current described by *Hagen and Feistel* (2007) follows the seasonal variability of the wind field with significantly reduced speeds during the summer months (Fig. 5.6b). This is in agreement with previous investigations that have shown that the variability of the rim current is not necessarily related to deep-water intrusions although it may be strongly influenced by them during inflow events (*Reissmann et al.*, 2009). The connection between wind forcing and deep-water dynamics is further corroborated by the temporal evolution of the kinetic energy, $|\tilde{\mathbf{u}}|^2$, residing in the associated velocity fluctuations, $\tilde{\mathbf{u}} = \mathbf{u} - \langle \mathbf{u} \rangle_T$, that are seen to be strongly correlated with the wind forcing on time scales down to the duration of individual storm periods (Fig. 5.6c,d).

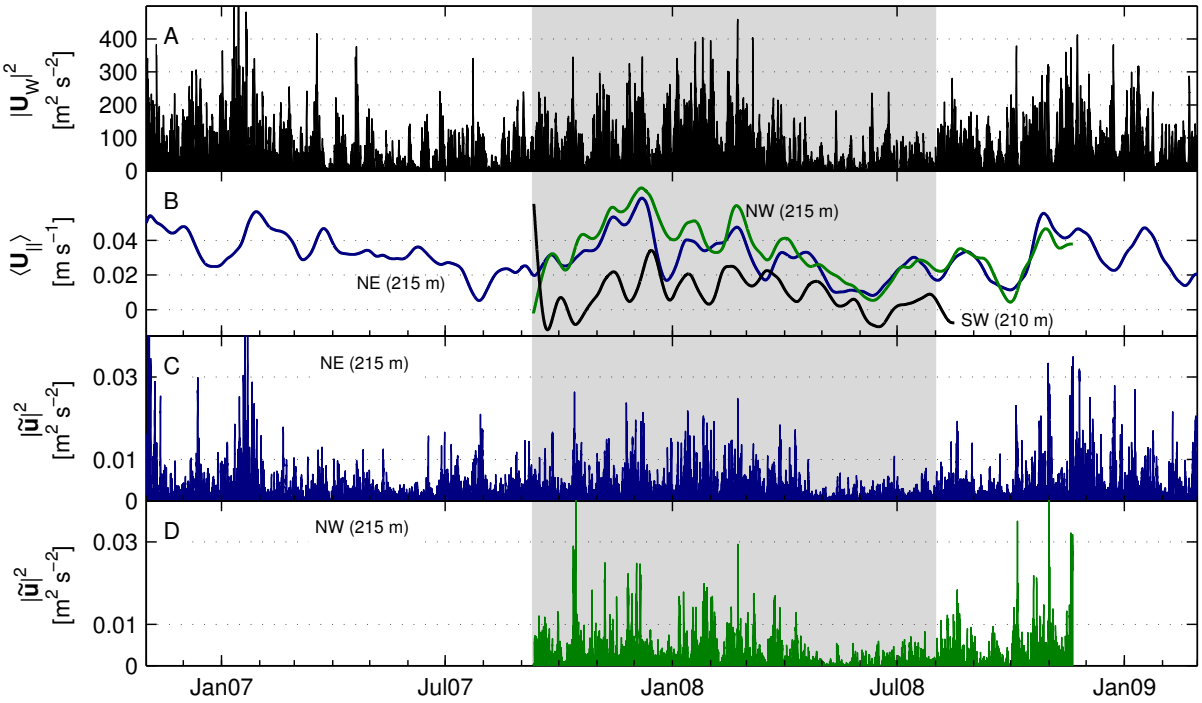

Figure 5.6.: Time series of (a) square of the wind speed, (b) 30-day low-pass filtered velocity (along-slope component, positive in anti-clockwise direction), and fluctuating kinetic energy $|\tilde{\boldsymbol{u}}|^2$ based on high-pass filtered velocities (see text) at (c) position NE, and (d) position NW. Gray-shaded areas indicate the time interval displayed in Fig. 7.1 below.

6. BaTRE Part I: Tracer

6.1. Tracer injection

The tracer injection took place on 11 September 2007 at the central position I in the Eastern Gotland Basin during a cruise with RV Poseidon (Fig. 6.1). The amount of 0.9 kg (4.6 mol) of CF_3SF_5 was injected as a single streak of approximately 1 km length (Fig. 6.2a) inside a small density interval around the target isopycnal (potential density: 9.9 kg m^{-3}) as verified by the two independent CTD loggers mounted on the instrument frame. The small uncertainty in the injection density corresponds to less than 1 m vertical variability around the injection level at approximately 200 m depth, Fig. 6.2b. As in other experiments of this type, it is likely that the finite time required for the full dissolution of the tracer droplets results in a small amount of tracer sinking, and that the turbulent wake behind the injection system leads to some vertical mixing of the tracer plume. These effects are hard to quantify but the results from the first tracer survey described below suggest that neither had a strong impact on the vertical tracer dispersion on longer time scales.

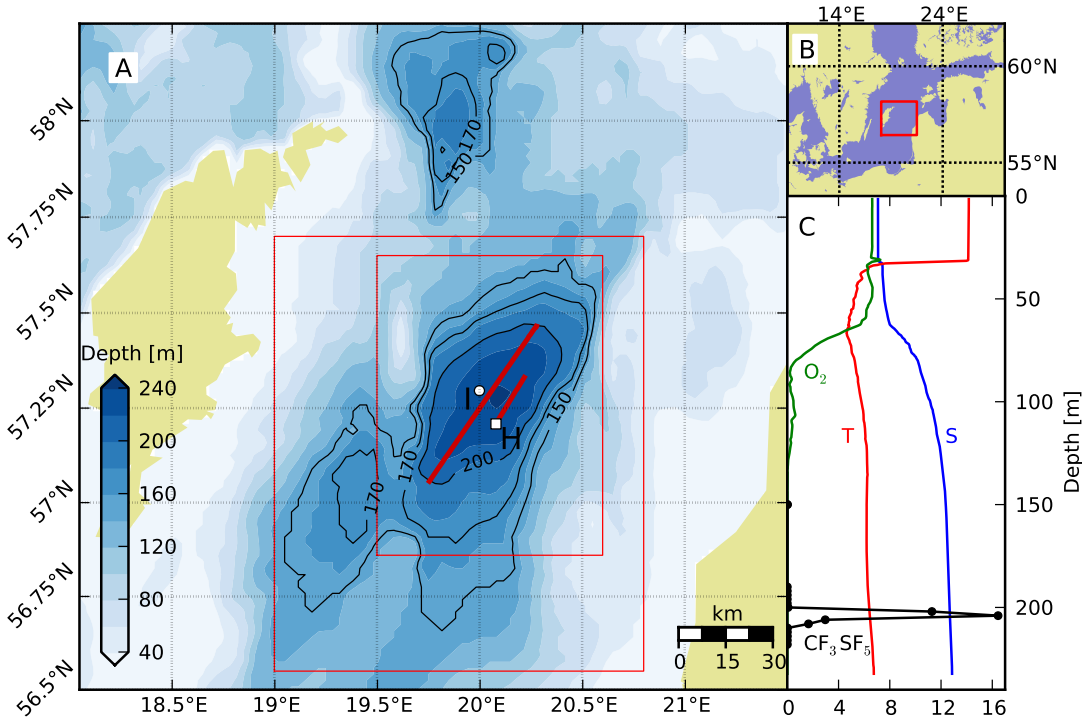

Figure 6.1.: (a) Gotland Basin with red rectangles marking sub-areas shown in later figures. "I" indicates the tracer injection, "H" the position where tracer was first detected. Pump-CTD tracks are shown as red lines; (b) overview map with study area marked in red; (c) CTD profile taken on 24 Sep 2007 at position H with salinity [g kg^{-1}], temperature [^{o}C], oxygen [ml l^{-1}], and the tracer concentration [10 pmol kg^{-1}].

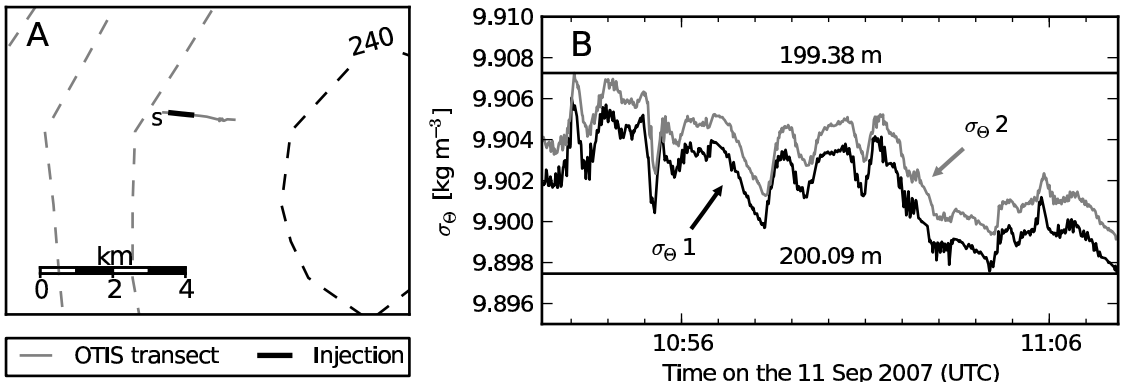

Figure 6.2.: (a) Injection track near position I (see Fig. 6.1), and (b) potential density variation during the injection with data from two simultaneously operated CTD systems on the OTIS.

6.2. Tracer surveys

After the injection cruise in September 2007, the spreading of the tracer was observed during six tracer surveys conducted between September 2007 and February 2009 with some of these cruises also including turbulence microstructure measurements as described in Chap. 5.2 (Tab. 5.2, Fig. 5.2). Here and in the following, DAI (days after injection) denotes the number of days elapsed between the tracer injection (11 September 2007) and the first tracer profile obtained during the tracer surveys, respectively. All times are reported in UTC.

6.2.1. Leg 1

Approximately 2 weeks after the injection, RV Poseidon returned to the Gotland Basin for first tracer survey (Leg 1) starting on 21 September 2007. In view of the anticipated streakiness of the tracer at this early stage of the experiment, we used a special strategy for the search of the tracer patch. Continuous water samples taken from the Pump-CTD were instantaneously analysed with the equilibrator system described above, while the CTD-frame was slowly towed along the target isopycnal, following two cross-basin transects inside the 200 m isobath (Fig. 6.1a). No significant tracer signals were found until 24 September 2007, when the tracer patch was first detected near position H. Subsequent vertical tracer profiling with the Pump-CTD at this position revealed a narrow tracer distribution with peak concentrations above 160 pmol kg^{-1} at a density of approximately $\sigma_\theta = 9.92$ kg m^{-3}, i.e. slightly higher than the injection density (Fig. 6.1c). This points at a small amount of sinking, probably during the injection as outlined above. A cast, taken immediately after the recovery of the Pump-CTD with the CTD Rosette system, did not hit the tracer patch again. Limited by available ship time, the tracer survey had to be discontinued but the results from Leg 1 were sufficient to draw the following important conclusions: (a) the tracer was injected at the intended target isopycnal, (b) tracer sinking and tracer mixing in the wake of the OTIS were small, and turned out to be insignificant compared to the spreading rates observed during later surveys, (c) advection has transported the tracer patch at least 10 km to the south-east within 11 days, and (d) the tracer distribution on the target isopycnal was found to be extremely inhomogeneous.

6.2.2. Legs 2-5

Leg 1 was followed by 5 additional tracer surveys that were, except for Leg 4 discussed below, carried out following a similar pattern. Tab. 5.2 includes a complete listing of the hydrographic cruises; Fig. 5.2 shows the time-line of the experiment, and Figs. 6.3 and 6.4 illustrate the station grid. For Legs 2, 3, and 5, the region of interest was covered with a regular station grid, on which bottle samples were taken with the CTD Rosette system. Samples were analysed on-board within approximately 60 minutes, using the purge and trap system described in Section 5.3.3. This waiting time was often used for microstructure measurements at the same location, yielding 4 or 5 full-depth profiles per tracer station as described in more detail in Chap. 7. The two cruises in summer 2008 with RV Merian (Leg 4/1) and RV Poseidon (Leg 4/2) were mostly dedicated to other research projects, and only a few tracer profiles, and no turbulence profiles, were obtained. Since no analytical system was on board, tracer samples were sealed into glass ampoules, and later analysed in the institute's laboratory. Due to the low mixing rates in summer and the small temporal separation between the two surveys, tracer profiles in the centre of the basin were found to have nearly identical shapes (see below), and we decided to discuss them jointly as Leg 4.

6.3. Conversion between potential density and depth

An important step in the analysis of vertical mixing with the help of an isopycnically averaged transport equation for the tracer concentration is the introduction of a representative mapping between potential density and depth. In the presence of bounding topography and a strong variability of isopycnal surfaces (Chap. 7) this is not a trivial task. *Winters et al.* (1995) showed that isopycnal displacements due to reversible (e.g., internal-wave) motions can be separated from irreversible changes due to mixing by adiabatically sorting the instantaneous density field into a state of minimum ("background") potential energy. While this method has frequently been applied for the interpretation of model data, a direct application to field data is complicated by the fact that synoptic data with sufficient resolution are rarely available.

Here, we have investigated three different approaches, each with relative merits and disadvantages, in order to separate reversible from irreversible isopycnal motions by approximating the vertical distribution of the density in the sorted background state. The most obvious approach is based on the assumption that the density profile in the deepest part of the basin represents the background state. By definition, this method has the advantage that the full depth range is included in the conversion between depth and density. However, the maximum density is often not observed at the deepest point of the basin, implying that tracer samples taken at higher densities are not included in the analysis. This problem can be overcome by interpreting the *densest* profile as the profile representing the sorted state. However, as illustrated in Fig. 6.6 showing all available density profiles for Legs 1-5, with this approach the lowest part of the water column is not included. In some cases (e.g., for Leg 3), this loss of data corresponds to a substantial fraction of the lower water column.

As a useful alternative, here we suggest the following approximation for the background density field that, as the original method of *Winters et al.* (1995), is based on sorting. Potential density profiles taken at the lateral positions $\boldsymbol{x}_j$ are interpolated onto a set of standard depths z_i with vertical spacing $\Delta z = 1$ m. We assign the volume $\Delta V_j = \Delta z \, \Delta A_j$ to each point in this grid, where ΔA_j corresponds to the horizontal area represented by the CTD profile taken at position $\boldsymbol{x}_j$. Practically, we identify ΔA_j with the area of Voronoi cells found from a so-called Voronoi decomposition of the CTD grid. The mathematical method is described in *Barber et al.* (1996);

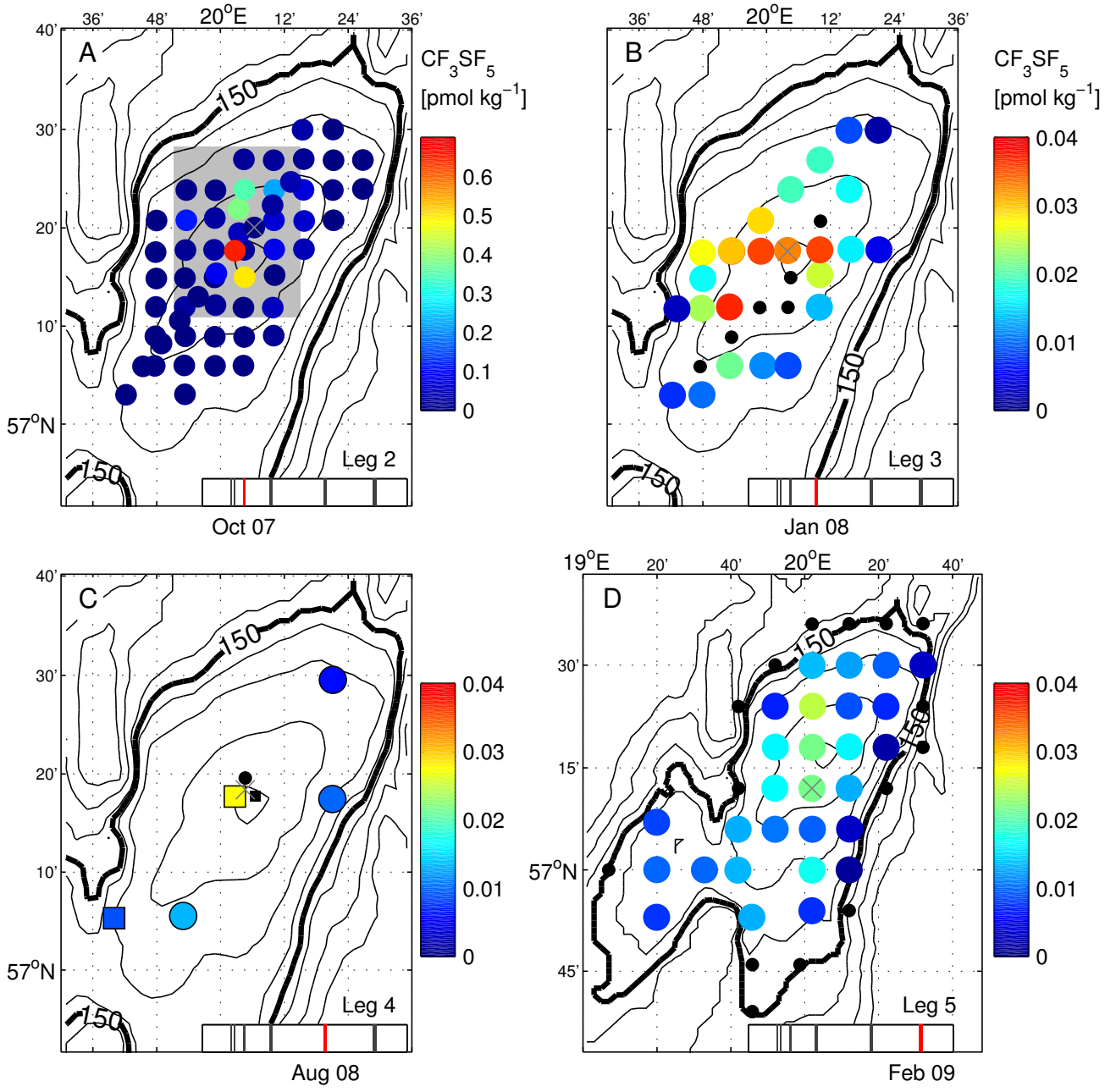

Figure 6.3.: Spatial distribution of tracer concentrations averaged between the bottom and 150 m depth (cruise dates are schematically indicated in the lower right of each panel). Note the different scale in (a) and map area in (d). Crosses indicate positions of the densest profiles; black markers show profiles not covering the entire averaging range. Measurements at the central station in (c) have been slightly shifted for better visibility. The grey rectangle in (a) indicates the area shown in Fig. 6.13.

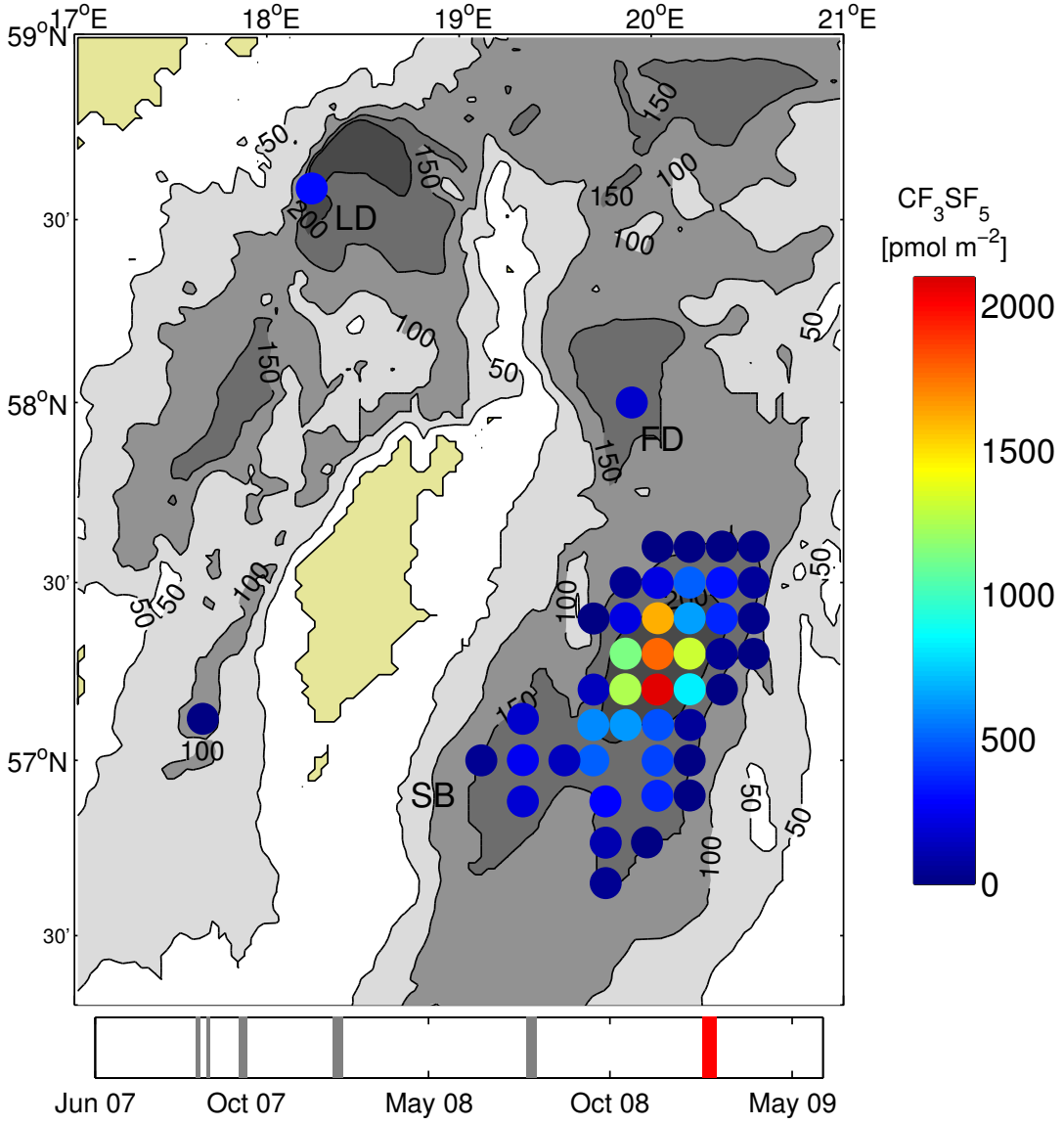

Figure 6.4.: Vertically integrated tracer concentrations for Leg 5 (cruise date is indicated in the legend). All available measurements are shown, including those from the south-western side basin (SB), from the Fårö Deep (FD), and from the Landsort Deep (LD).

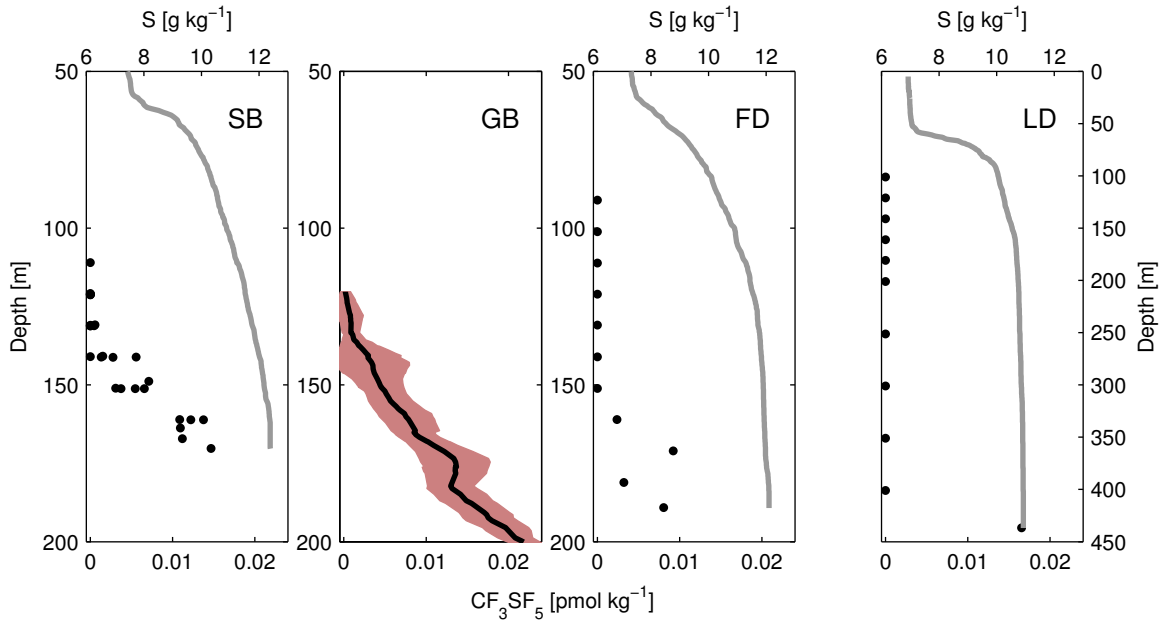

Figure 6.5.: Tracer samples (black dots) and salinity profiles (grey) in the south-western Side Basin (SB), the Gotland Basin (GB), the Fårö Deep (FD), and the Landsort Deep (LD) for Leg 5 (514 DAI). The second panel shows the average tracer profile (black line, uncertainty in red) in the Gotland Basin.

some examples for Voronoi decompositions of Leg 2 and Leg 3 are shown in Fig. 6.7.

Using the hypsographic area $A(z)$ of the basin, the background density field is found by monotonically sorting the measured densities along the new vertical coordinate z^*. Using this method, each original density estimate obtained at lateral position $\boldsymbol{x}_j$ and depth z_i is assigned a new (sorted) vertical position z^*_{ij}. The original volumes ΔV_j (and hence the total volume) are retained, provided the vertical depth interval Δz^*_{ij} in the sorted state obeys the relation $\Delta z^*_{ij} A(z^*_{ij}) = \Delta z \, \Delta A_j$.

Clearly, this method is only an option if a sufficient number of CTD profiles is available, and if it is assumed that ship surveys represent a synoptic picture of the density field, which is only satisfied in an approximate sense here. Sorted density profiles for all cruises are shown in Fig. 6.6, together with the original density profiles on which the sorting was based. In spite of the practical imperfections outlined above, it is evident that the sorting approach retains two important properties of the original method by *Winters et al.* (1995): it includes both the full depth range and the full density range, different from the two simple approaches outlined above. For these reasons, the mapping of depth on potential density discussed in the following will be based on sorting, unless otherwise noted.

6.4. Observation of tracer spreading

All tracer samples obtained during Legs 2-5 are summarised in Figs. 6.8-6.11 as functions of potential density, and, using the algorithm described above, as functions of depth. Isopycnal averages were evaluated in discrete form as the average of the tracer concentrations in a volume of fluid bounded by two isopycnal surfaces with potential densities σ_θ and $\sigma_\theta + \Delta\sigma_\theta$, respectively, where we used a constant spacing of $\Delta\sigma_\theta = 0.01$ kg m^{-3} in density space.

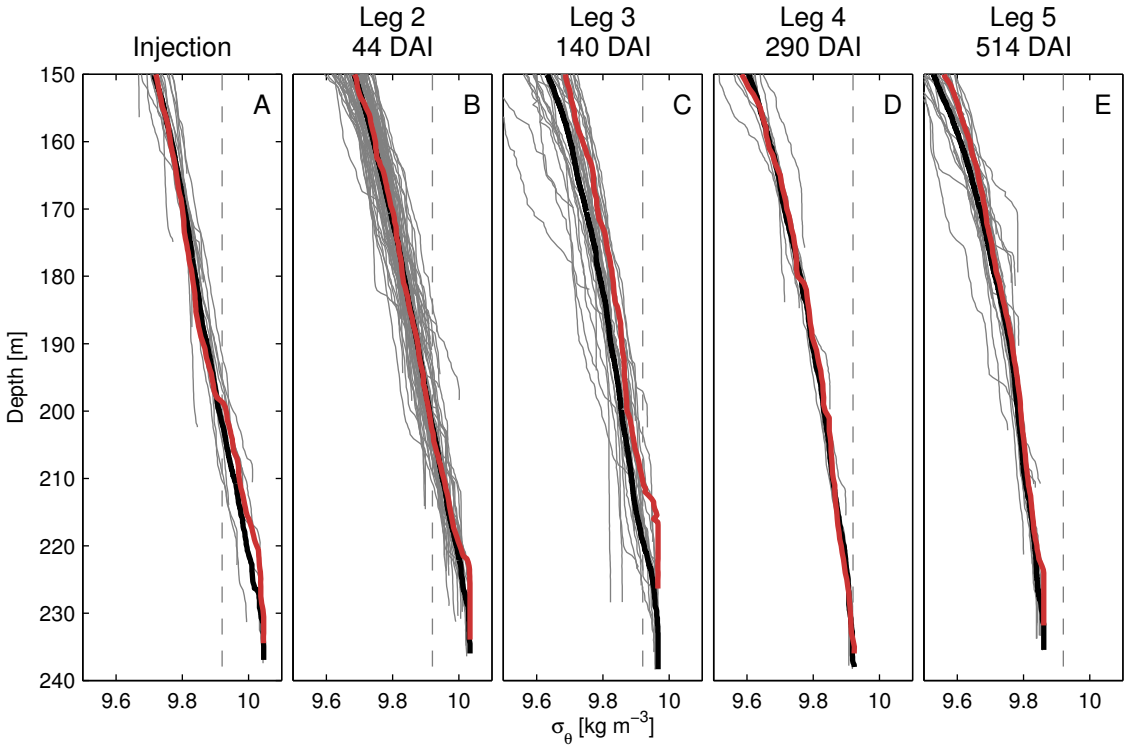

Figure 6.6.: Potential density observed during the injection and the tracer surveys (Legs 2-5). Gray: all available profiles. Red: densest profile. Black: sorted profile (see Section 6.3). Dashed grey line is target density of injection.

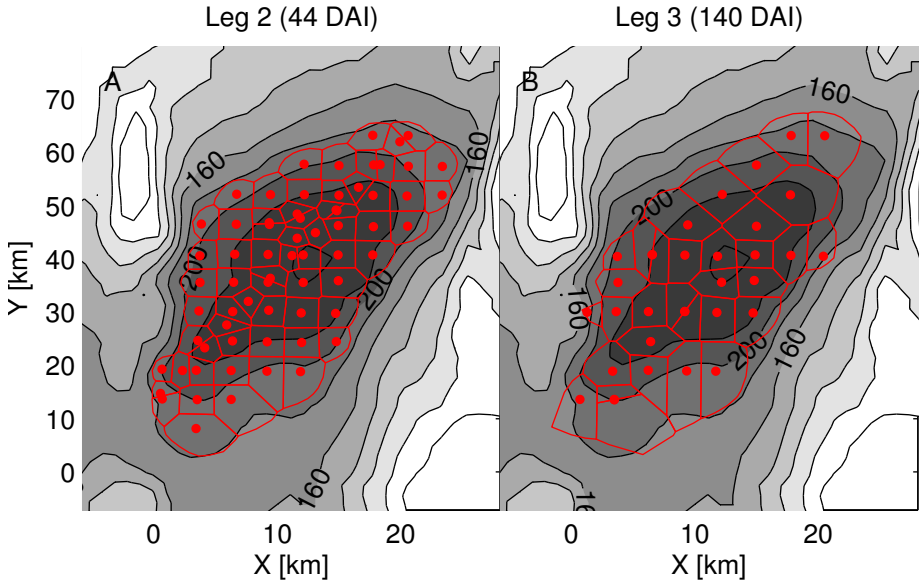

Figure 6.7.: Locations of CTD casts (red dots) for (a) Leg 2, and (b) Leg 3, and corresponding Voronoi cells used for the density sorting algorithm described in Section 6.3.

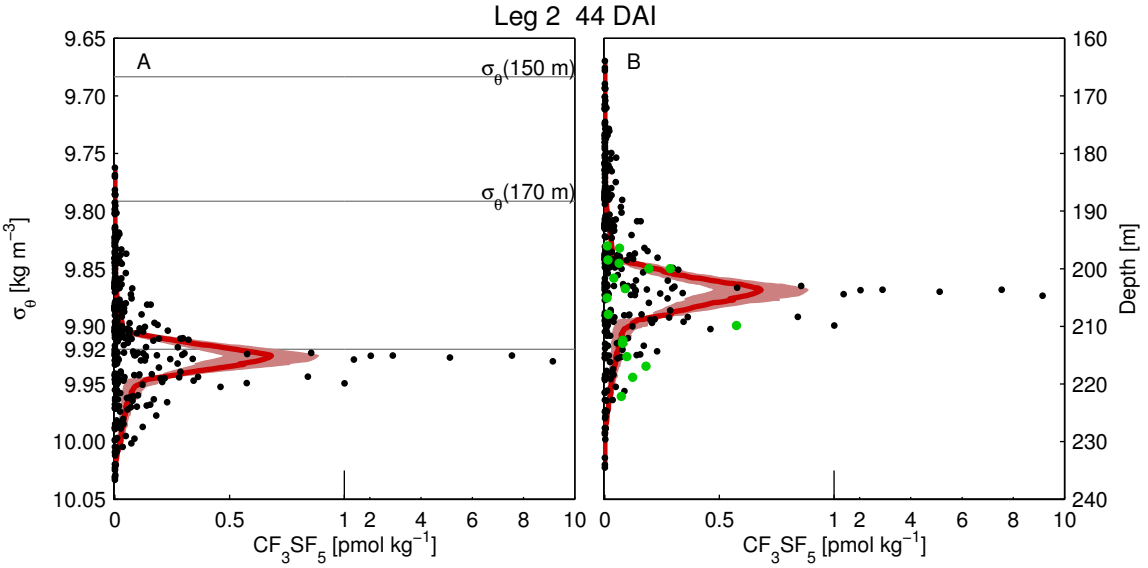

Figure 6.8.: Tracer distribution for Leg 2 plotted (a) versus potential density, and (b) versus depth in the sorted reference state (see Section 6.3). Note the change of scale at 1 pmol kg^{-1}. Average profile in red, uncertainty in light red. Horizontal lines in (a) mark selected depth levels discussed in the text. Green dots in (b) denote near-bottom non-zero tracer samples (taken within 2 m distance from the bottom).

Due to the small number of tracer profiles this approach was not applicable to Leg 4; instead, for this data set, we used the weighted averaging method described in *Ledwell and Bratkovich* (1995). An overview over the lateral distribution of the tracer during Legs 2-5 is given in Fig. 6.3, showing the average tracer concentration below the 150 m isobath that encloses the basin and its south-western appendix (Fig. 6.1). The isopycnal distribution of the tracer for Legs 2-5 is illustrated in Fig. 6.12, where, as an example, isopycnals located in the vicinity of the injection level (approximately 200 m depth) have been chosen.

6.4.1. Tracer spreading in the Gotland Basin

Figs. 6.3a and 6.12a illustrate that during Leg 2 (44 DAI) the lateral tracer distribution was still extremely inhomogeneous, which is also evident in the isopycnal scatter shown in Fig. 6.8. Nearly all of the tracer profiles peak at 9.92 kg m^{-3}, suggesting that no further tracer sinking had occurred after Leg 1. Tracer concentrations above 170 m depth are negligible, and we expect that no tracer has left the central Gotland Basin at this early stage of the experiment. Moreover, Figs. 6.3a and 6.12a suggest that the tracer patches have not been in intense contact with the lateral slopes of the basin, which will be important for the distinction between interior and boundary mixing processes discussed below. Nevertheless, in some of the near-bottom samples (green markers in Fig. 6.8b) small amounts of tracer were found, pointing at a starting influence of boundary mixing. We will come back to this point below.

In view of the observed patchiness, it is not unlikely that advection of small-scale tracer patches has resulted in double-counting of the same tracer at different grid points during the survey. To investigate this aspect more closely, the exact sampling dates as well as the pseudo-trajectories computed from the current records at moorings C1 and NW are summarised in Fig. 6.13. These data let us suspect that, indeed, some tracer patches were measured twice. For

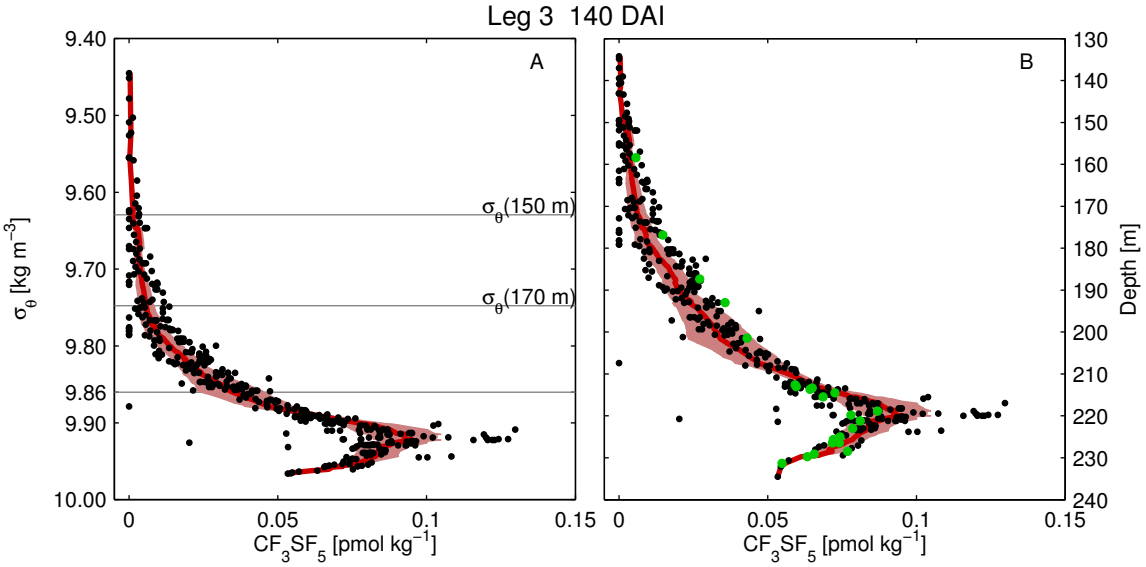

Figure 6.9.: As Fig. 6.8 but now for Leg 3.

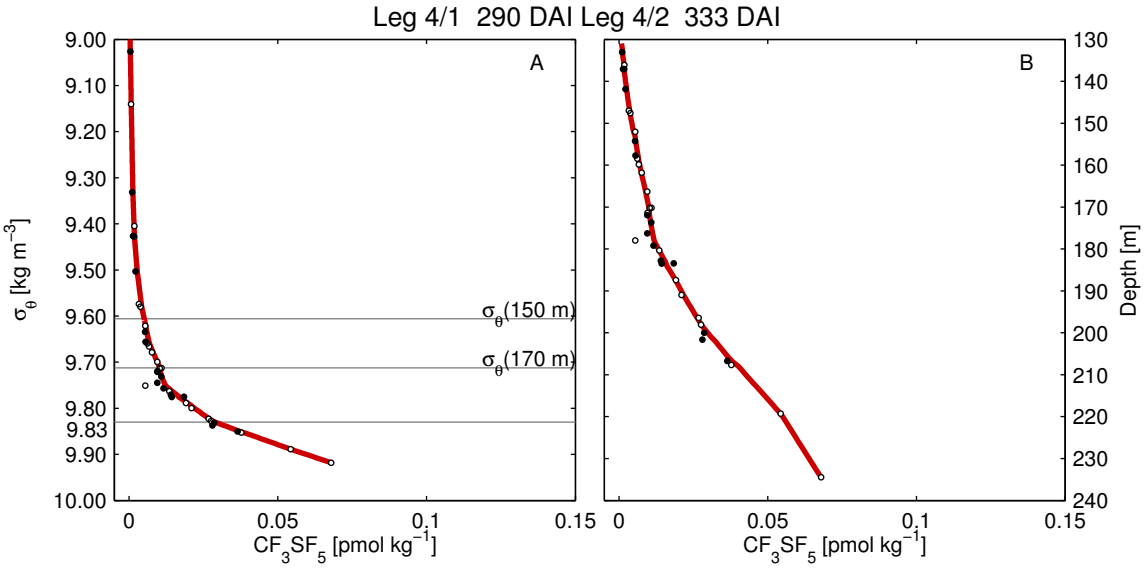

Figure 6.10.: As Fig. 6.8 but now for Leg 4. White circles show the tracer samples for Leg 4/1 (June 2008), black circles of Leg 4/2 (August 2008).

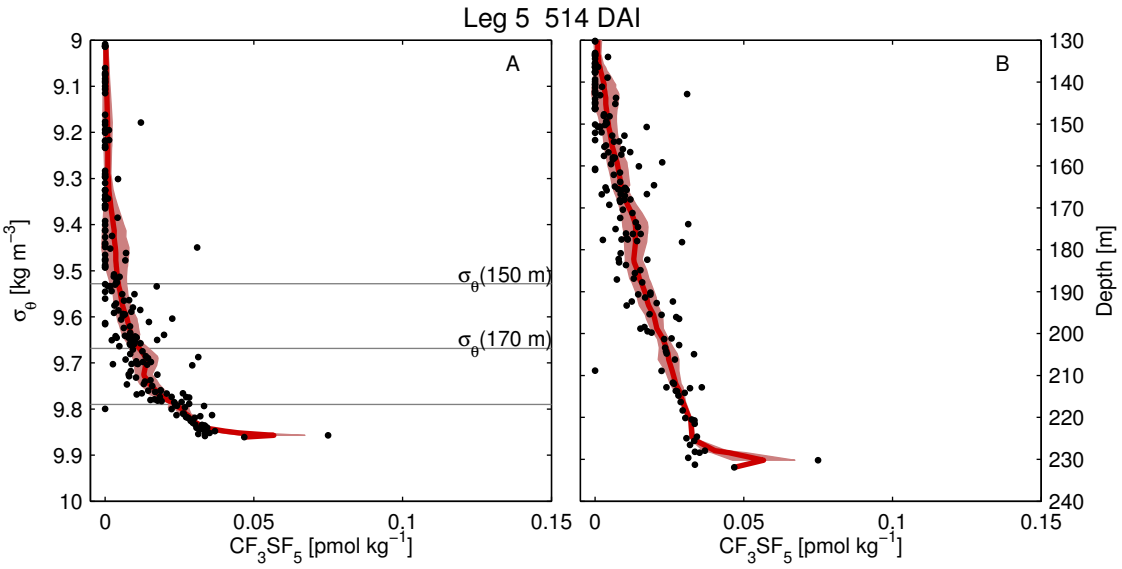

Figure 6.11.: As Fig. 6.8 but now for Leg 5.

example, the pseudo-trajectories at C1 and NW marked in grey suggest that the patch with the highest concentrations measured on 25 Oct 18:18 could have been advected southward during the following 2.9 days, and was re-sampled a second time, at least partly, on 28 Oct 16:46 approximately 5 km south-east (Fig. 6.13). Similarly, it is likely that the northern patch, first sampled on 26 Oct 23:09, was re-sampled 17 hours later on 27 Oct 16:16, a few kilometres south (the corresponding section of the trajectories is coloured in red). The implications of this double-counting for the construction of the basin-scale tracer budget will be discussed in more detail below (it should be noted in this context the possibility of double-counting also implies the possibility of missing tracer patches).

The tracer concentrations during the following Legs 3-5 (Figs. 6.9-6.11) reveal a strong reduction of isopycnal scatter compared to Leg 2, consistent with the comparably homogeneous lateral tracer distributions shown in Figs. 6.3 and 6.12. Already for Leg 3 (140 DAI), lateral dispersion and subsequent mixing have strongly reduced the initial patchiness of the tracer, suggesting, as a first important result, that lateral mixing occurs on a time scale of a few months. From these data it is also evident that from some point between Legs 2 and 3, the tracer was in permanent contact with the lateral slopes of the basin, pointing at a possible influence of boundary mixing processes. The tracer concentrations for Leg 4/1 and Leg 4/2 are, despite the low number of samples and the time difference of approximately 40 days between the cruises, in remarkable agreement (Fig. 6.10). This is consistent with Chap. 7, where we have investigated heat and salinity budgets from moored instrumentation, and concluded that mixing during the summer months is generally weak.

Overall, steadily decreasing tracer concentrations below 150 m depth are observed (Figs. 6.9-6.11), indicating a net loss of tracer from the deep, enclosed part of the basin. Fluid above this level is topographically almost unconstrained (see Fig. 6.1), suggesting that mixed upwards tracer is likely to be advected across a large area of the Baltic Sea, and will quickly be diluted below the detection limit.

The vertical concentration profiles shown in Figs. 6.9-6.11 reveal a number of features that are rather different from tracer experiments conducted in the open ocean. The presence of lateral boundaries leads to an symmetric vertical spreading around the tracer peak, and a gradual

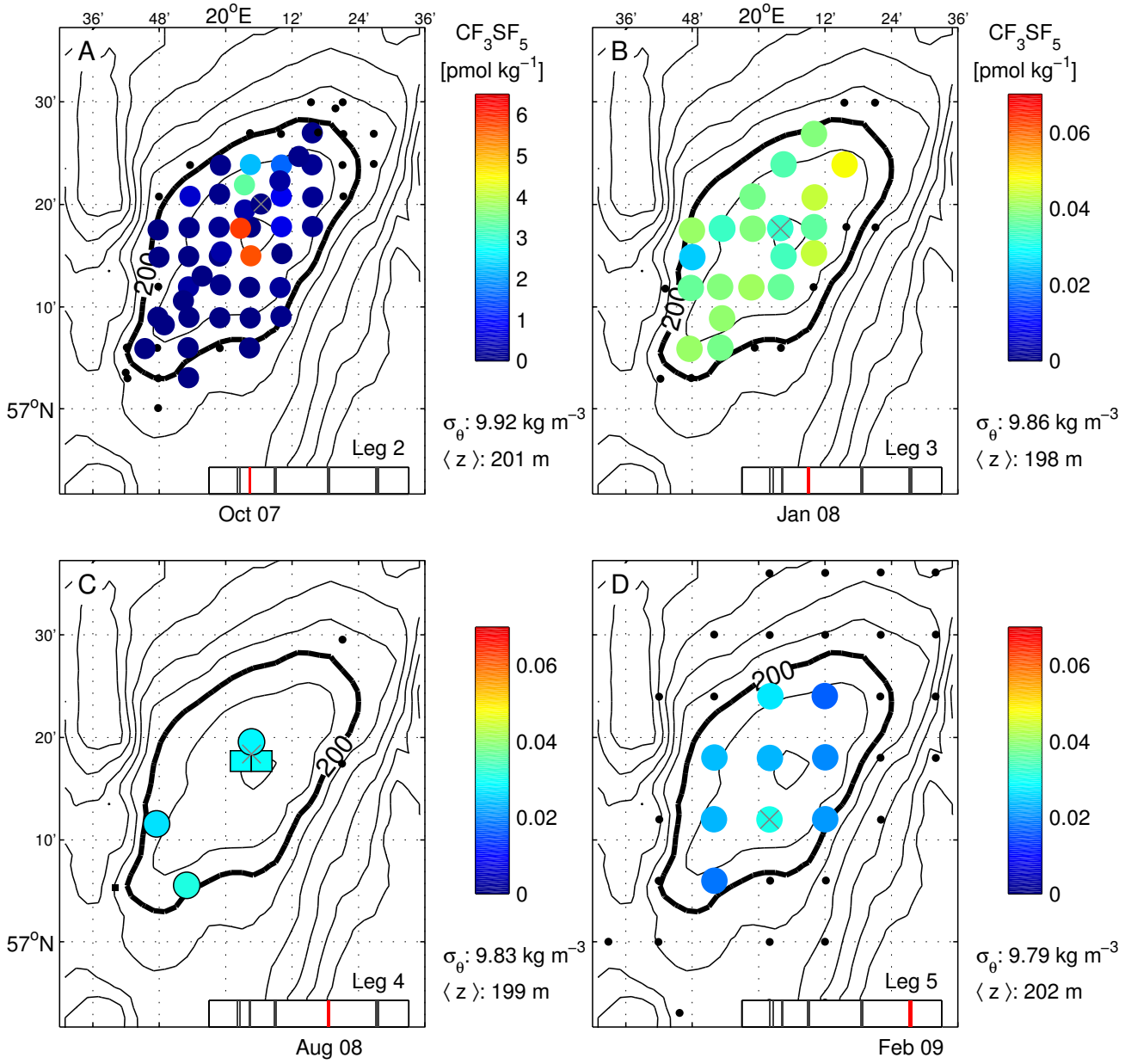

Figure 6.12.: As in Fig. 6.3, but now the tracer distribution on isopycnals located at approximately 200 depth are shown (corresponding values of σ_θ as indicated). Isopycnal positions in density space are marked in Figs. 6.8a-6.11a. Note the different scale in (a).

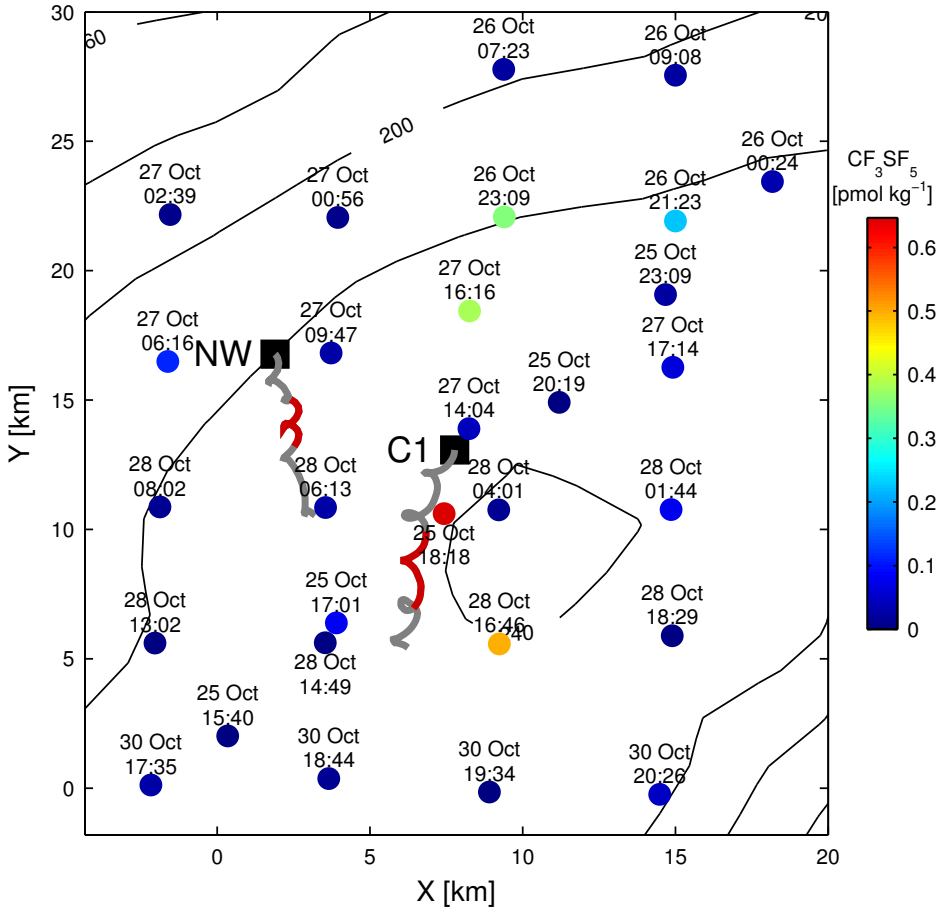

Figure 6.13.: Enlarged view of the central basin (area indicated in Fig. 6.3) with vertically averaged tracer concentrations during Leg 2 (exact sampling dates are indicated on top of each measurement). Positions of moorings NW and C1 are marked as black squares. Gray lines correspond to pseudo-trajectories at 200 m depth for 2.9 days between 25 Oct (18:18 UTC) and 28 Oct (16:46 UTC); marked in red are 0.7 days between 26 Oct 2007 (23:09 UTC) and 27 Oct (16:16 UTC).

sinking of both the injection isopycnal (potential density: 9.92 kg m^{-3}) and the tracer peak. As shown below, this sinking mirrors the reduction of deep-water density due to mixing rather than being related to any kind of vertical advection mechanism. After Leg 4, approximately 10 months after the injection, the injection isopycnal has reached the bottom, and cannot be found anymore on subsequent cruises. As a consequence, a transition is observed from tracer profiles with a well-defined peak near the injection isopycnal (Figs. 6.8 and 6.9) towards profiles with concentrations increasing monotonically with depth (Figs. 6.10 and 6.11).

6.4.2. Beyond the Gotland Basin

In order to investigate the propagation of tracer beyond our study site in the Gotland Basin, Leg 5 also included tracer samples from a number of neighbouring side basins, including the Fårö Deep (FD), the Landsort Deep (LD), the south-western side-basin (SB) of the Gotland Basin,

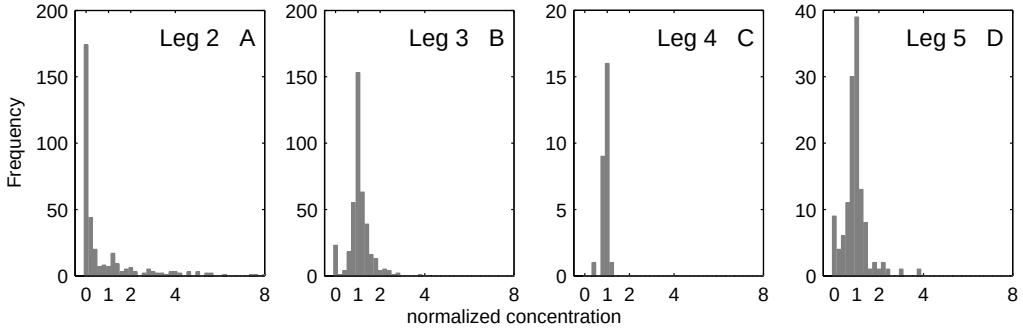

Figure 6.14.: Histogram of normalised tracer concentrations n_{ij} for Legs 2-5.

and an unnamed location south-west of the island of Gotland (Fig. 6.4). Tracer was detected in the deep water of all these stations, except south-west of Gotland, supporting the idea that deep-water transport of dissolved matter may occur over considerable distances even during a stagnation period with no major inflow events.

A comparison of tracer profiles from the Gotland Basin and the side-basin SB (Fig. 6.5) illustrates a nearly identical vertical distribution at overlapping depth intervals, suggesting a close communication between both basins. A likely mechanism explaining this similarity is that the frequently observed, strong isopycnal displacements (as described in Chap. 7) lift tracer from the Gotland Basin over the sill, where it subsequently intrudes in the form of dense gravity currents into the side basin. In spite of the shallower sill-depth, a similar mechanism may have transported tracer also to the Fårö Deep, where comparable tracer concentrations were found in the same depth range, as well as in the Landsort Deep (LD), where significant tracer concentrations could only be identified in the lowest sample close to the bottom (Fig. 6.5).

6.4.3. Tracer statistics

Following *Ledwell and Watson* (1991), some useful statistical characteristics of the tracer distribution can be obtained by normalising individual tracer samples, where c_{ij} are the local concentrations measured at depth z_i and lateral position $\boldsymbol{x}_j$, with the mean concentration $\langle c_i \rangle$ computed for the same depth: $n_{ij} = c_{ij}/\langle c_i \rangle$. Consistent with the discussion of lateral variability in the previous section, the distribution of the n_{ij} for Leg 2 is strongly skewed, with a dominance of empty tracer samples ($n_{ij} = 0$), and few very high concentrations with $n_{ij} \gg 1$ (Fig. 6.14a). This is contrasted by the histograms for Legs 3-5, exhibiting a symmetrical distribution around peak value near $n_{ij} = 1$ (Fig. 6.14b-d). Using the fact the these distributions are nearly Gaussian, we identify the uncertainty regions shown in Figs. 6.9-6.11 with the respective standard deviations. For the highly non-Gaussian histogram of Leg 2 (see Fig. 6.9), however, the uncertainty was computed based on the difference in profile shapes, as suggested by *Ledwell and Bratkovich* (1995).

6.5. Mixing rates

6.5.1. Budget of total deep-water tracer mass

The evolution of the total amount of tracer in the Gotland Basin is estimated here from the integral of the isopycnally averaged concentrations, taking the basin geometry into account:

$$M = \int_{z_b}^{z_t} \langle c \rangle A \, \mathrm{d}z \,, \tag{6.1}$$

where z_b denotes the position of the bottom, and z_t the upper integration limit, either $z_t = 170$ m or $z_t = 150$ m. In the latter case, the integration volume includes the side-basin (SB) but not the Fårö Deep (see Fig. 6.4). Recall that for Leg 2, tracer is found only in a few small patches, such that $\langle c \rangle$ is not representative for the whole basin area. In this case, the tracer mass M was calculated from the horizontal integral of the vertically integrated tracer concentrations. Uncertainties are computed from the standard deviations derived in the previous section, except for Leg 4, where the number of samples was not sufficient for reliable statistics.

As discussed in Section 6.4.1, it is quite likely that during Leg 2 advected small-scale tracer patches have been sampled twice at different grid points. To test the potential implications of this, the tracer mass for this cruise was estimated in two ways: (a) with the tracer concentrations as they were measured, and (b) with tracer concentrations excluding profiles from 25 Oct 18:18 and 27 Oct 16:16, corresponding to tracer patches that were possibly measured a second time at different positions (see Fig. 6.13 and discussion above). The estimated tracer masses for Legs 2-5 shown in Fig. 6.15 illustrate the gradual loss of tracer in the deep water of the Gotland Basin due to vertical mixing followed by lateral advection out of the study area. For Leg 2, realistic (i.e. smaller than injected) values of M are obtained only if double-counted profiles are excluded. The rate of tracer loss is seen to decrease with time, which should, however, not be misinterpreted as an indication for decreasing deep-water mixing. This is for example evident from the fact that the stagnation of the total deep-water tracer mass between Legs 3 and 4 is accompanied by a strong vertical tracer redistribution below 150 m depth (compare Figs. 6.10 and 6.11) that is indicative for deep-water mixing without a net tracer loss to higher layers.

At the end of the observation period (Leg 5, 514 DAI), approximately 2 of the injected 4.6 mol of CF_3SF_5 are still found in the study area below 150 m depth, including a small (7 percent) contribution from the south-western side-basin. Less than 5 percent of the tracer mass in the Gotland Basin is found in the Fårö Deep, which is, however, not included in the budget for the Gotland Basin. The exodus of tracer from the deep water is not approximated very well by an exponential decay law (Fig. 6.15). Nevertheless, an e-folding time scale for deep-water renewal of somewhat less than 2 years appears to be a useful first-order estimate.

6.5.2. Vertical diffusivities

From the lateral tracer distributions discussed in the context of Figs. 6.3 and 6.12 above, we know that during the initial phase of the experiment the tracer has not been in intense contact with the lateral slopes of the basin. While for this initial period we expect that the observed vertical tracer spreading results mainly from interior mixing processes, during all subsequent cruises boundary mixing processes have to be taken into account. This different behaviour is mirrored in different methods for the data analysis.

In the first case (interior mixing), the presence of lateral boundaries may be ignored, and the analysis becomes identical to that used for tracer experiments in the open ocean. Here, as discussed in *Ledwell and Watson* (1991), it is advantageous to work with a normalised tracer

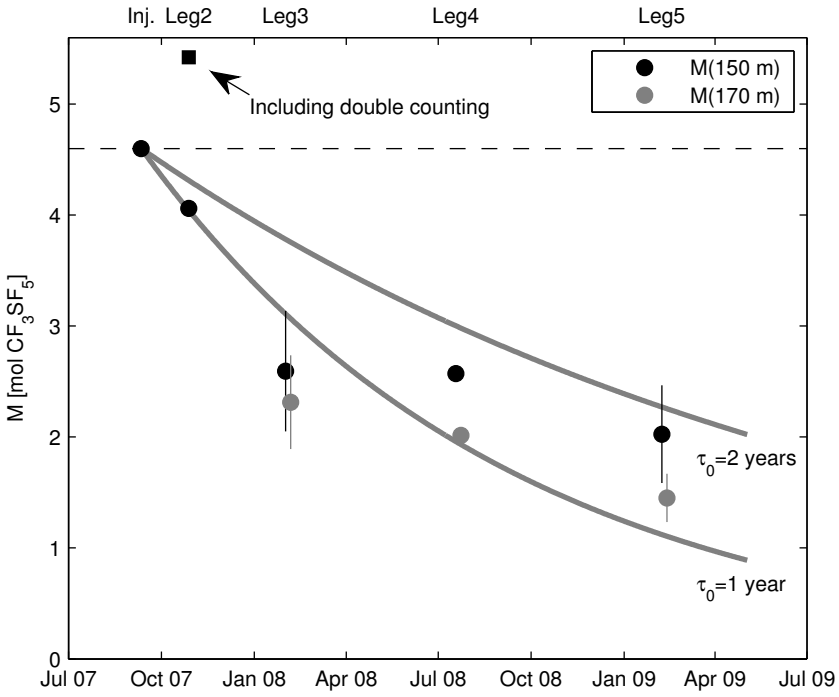

Figure 6.15: Total amount of tracer in the Gotland Basin below 170 m (grey) and below 150 m (black, including side basin). Gray curves correspond to exponential decay functions with time constants as indicated. The dashed line indicates the injected amount of 4.6 moles.

profile, $r(z) = \langle c \rangle(z) A/M$, where $\langle c(z) \rangle$ is the mean tracer concentration, and A an arbitrary but constant horizontal integration area, equal to or larger than the area with significant tracer concentrations. If isopycnal convergence is ignored (no lateral inflows), the normalised concentrations obey a diffusion equation of the form

$$\frac{\partial r}{\partial t} = \kappa_I \frac{\partial^2 r}{\partial h^2}\,, \tag{6.2}$$

where h is the distance from the tracer peak at the target density, and κ_I denotes the constant interior diffusivity. In discrete form, *Ledwell and Watson* (1991) suggest to compute $r_i = r(z_i)$ from the relation $r_i = \sum_j w_j c_{ij} / \sum_j I_j$, where I_j denotes the vertical tracer integral at position $\boldsymbol{x}_j$. The weighting function is defined as $w_j = I_j / \sum_j I_j$.

After isopycnal dispersion has brought the tracer in permanent contact with the lateral boundaries (this occurs at some time between Legs 2 and 3), boundary mixing processes cannot be ignored any longer. It can be shown that the transport equation describing the basin-scale vertical tracer transport in this case is of the form:

$$A \frac{\partial \langle c \rangle}{\partial t} = \frac{\partial}{\partial z} \left(A \kappa_{\mathrm{SF5}} \frac{\partial \langle c \rangle}{\partial z} - A \bar{w} \langle c \rangle \right) + c_{\mathrm{in}} \frac{\partial A \bar{w}}{\partial z}\,, \tag{6.3}$$

where $\kappa_{\mathrm{SF5}}(z)$ is the, not necessarily constant, effective basin-scale tracer diffusivity, including boundary processes, and $\bar{w}(z)$ the vertical advection velocity. The latter is used below to model the effect of lateral inflows (intrusions), where $c_{\mathrm{in}}(z)$ denotes the tracer concentration of intruding fluid (usually assumed to be zero). The basin geometry is taken into account with the help of the hypsographic relation for the basin area $A(z)$. Equations analogous to Eq. (6.3) describe the basin-scale vertical transport of salinity and temperature, where, for high-Reynolds number flows and in the absence of double diffusive effects, the corresponding effective diffusivities for temperature, κ_θ, and salinity, κ_S, are expected to coincide with κ_{SF5}. In all cases, a zero-flux boundary condition is applied at the bottom.

6.5.3. Interior mixing rates

For the period between the injection and Leg 2 (interior mixing only), modelled concentration profiles $r(z)$ are computed from Eq. (6.2) for varying κ_I, using a delta-distribution at $r(0)$ as the initial condition. The diffusion equation in Eq. (6.2) was discretised with a centred finite difference scheme with vertical resolution $\Delta z = 0.5$ m, and explicit time stepping. The "optimal" diffusivity was identified from these simulations as the value of κ_I minimising the cost function

$$\chi(\kappa_I) = \int (r - \hat{\mathbf{r}})^2 \mathrm{d}z \ , \tag{6.4}$$

where $\hat{\mathbf{r}}$ is the measured normalised tracer distribution during Leg 2. Following *Ledwell and Watson* (1991), we compute the uncertainty in $\hat{\mathbf{r}}(z_i)$ from the weighted standard deviation of the normalised tracer distribution: $\sigma_i = \sum_j w_j/(1-w_j)(r_{ij} - r_i)^2$, where $r_{ij} = c_{ij}/I_j$. This has been shown to be a useful estimate for non-Gaussian tracer distributions.

The results are summarised in Fig. 6.16. The optimal diffusivity according to Eq. (6.4) was found to be $\kappa_I = 1.1 \times 10^{-6}$ m^{2}s^{-1}, where the condition that the modelled profiles are within one standard deviation σ_i of the concentration at the tracer peak yields an uncertainty of 0.2×10^{-6} m^{2}s^{-1} for κ_I. A similar computation for the period between Leg 1 and Leg 2 (33 days) yields 1.0×10^{-6} m^{2}s^{-1}, where we have used the measured profile for Leg 1 as initial condition, instead of the delta distribution.

To check the stability of this result, we also tested an alternative method that is based on the well-known fact that for a diffusion problem of the form Eq. (6.2), the second moment σ_z^2 of the vertical tracer distribution $r(z)$ increases at a rate proportional to the diffusivity (e.g., *Kundu and Cohen*, 2008):

$$\frac{\mathrm{d}\sigma_z^2}{\mathrm{d}t} = 2\kappa_I \ . \tag{6.5}$$

With σ_z computed from the measured $\hat{\mathbf{r}}(z)$ for Leg 2, this approach yields $\kappa_I = 2.5 \times 10^{-6}$m^{2}s^{-1} for the time interval between the injection and Leg 2. Visual inspection of the modelled tracer profile suggests, however, that this value is an upper limit for κ_I because part of the variance results from the higher spreading rates at the lower edge of the peak (Fig. 6.8) that are indicative for the beginning impact of boundary mixing. We thus conclude that the interior diffusivity is close to 1×10^{-6} m^{2}s^{-1}, and unlikely to exceed the threshold of 2.5×10^{-6} m^{2}s^{-1}.

6.5.4. Basin-scale mixing rates

Basin-scale vertical diffusivities for the periods between Legs 3 and 4 (150 days), and Legs 4 and 5 (224 days) were estimated with the help of the transport equation in Eq. (6.3), including hypsography but assuming that lateral intrusions have no significant effect on the tracer spreading ($\bar{w} = 0$). The latter is confirmed by the long-term observations from moored instrumentation described in Chap. 7. The period between Leg 2 and 3 turned out to be more complex due to the transition from interior to boundary mixing as discussed in Section 6.5.5 below.

For the period between Legs 3 and 4, we solved Eq. (6.3) numerically for the tracer concentrations, as well as two analogous equations for the isopycnally averaged potential temperatures and salinities, assuming $\bar{w} = 0$ in all cases. A Dirichlet-type boundary condition at the top of the integration volume (150 m) was derived for each of these variables by linearly interpolating between the observed values at the start and end of the integration period, respectively. Identical basin-scale diffusivities were assumed: $\kappa_{\mathrm{SF5}} = \kappa_S = \kappa_\theta$, where, in contrast to the previous section, vertical variability in the diffusivities was allowed. Optimal diffusivity profiles were obtained by minimising the cost functions for T and S and tracer (with equal weights), now,

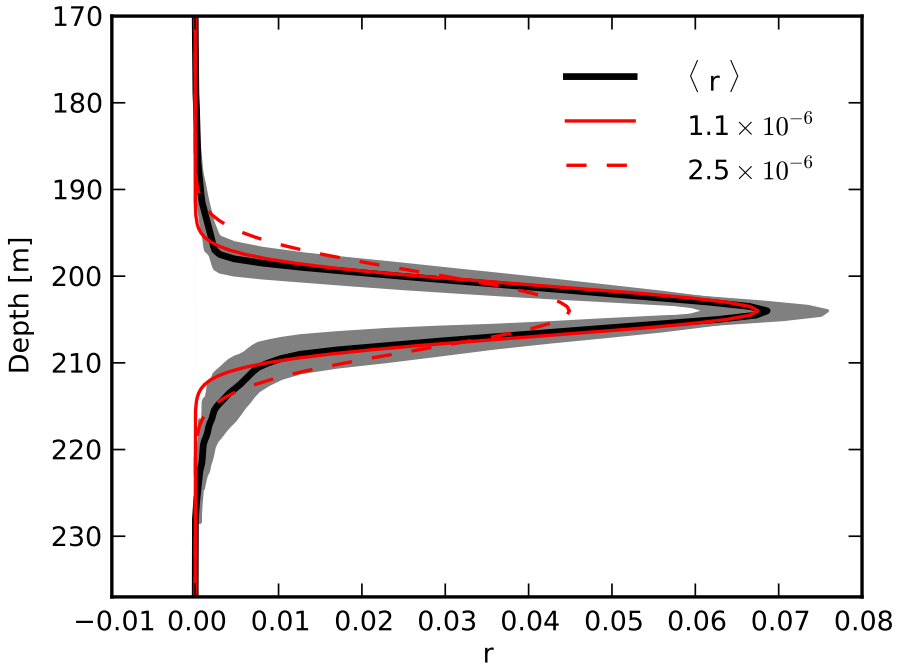

Figure 6.16.: Normalised mean tracer concentration r for Leg 2 (black) with grey-shaded area including one standard deviation around the mean. In red: profiles computed from the diffusion-model Eq. (6.2) with different diffusivities as indicated in the legend.

however, allowing for vertically variable diffusivities. The latter is realised by introducing 12 additional degrees of freedom by letting κ_S, κ_θ and κ_{SF5}, respectively, vary at 6 vertical positions (values between these positions are interpolated linearly onto the numerical grid). For the optimisation, we use the algorithm described in *Byrd et al.* (1995) to handle the large number of degrees of freedom in this problem efficiently.

The results of this analysis are depicted in Figs. 6.17 and 6.18. The solution of Eq. (6.3) with diffusivities optimised as described above is seen to lead to excellent agreement between observations and model results for all three variables. Diffusivities are of the order of 10^{-5} $\mathrm{m^2\ s^{-1}}$, and therefore approximately one order of magnitude larger than the interior diffusivities discussed in the previous section. This dramatic increase in mixing rates cannot be explained by differences in wind forcing because wind speeds between Legs 2 and 3 were on average substantially larger than those between Legs 3 and 4 (Chap. 7). It is, however, very likely that the strongly increased mixing rates reflect the effect of boundary mixing, consistent with the observation that during the whole period from Leg 3 to Leg 5 the tracer was in contact with the boundaries, whereas before Leg 2 this was not the case. This forms one of the main conclusion of this thesis.

It is worth pointing out that while the inclusion of hypsographic effects in Eq. (6.3) is essential to obtain acceptable fits between modelled and observed profiles, the vertical variability of the diffusivity is of secondary importance. Nevertheless, as visible in Figs. 6.17d and 6.18d, the diffusivity profiles exhibit a similar vertical structure with high values in the bottom boundary layer (BBL), a local minimum at 220-230 m depth, and increasing values in the layer above (note that the structure of the diffusivities inside and at the top of the BBL is not resolved with only 6 degrees of freedom in the vertical). This increase in diffusivities above 220 m is

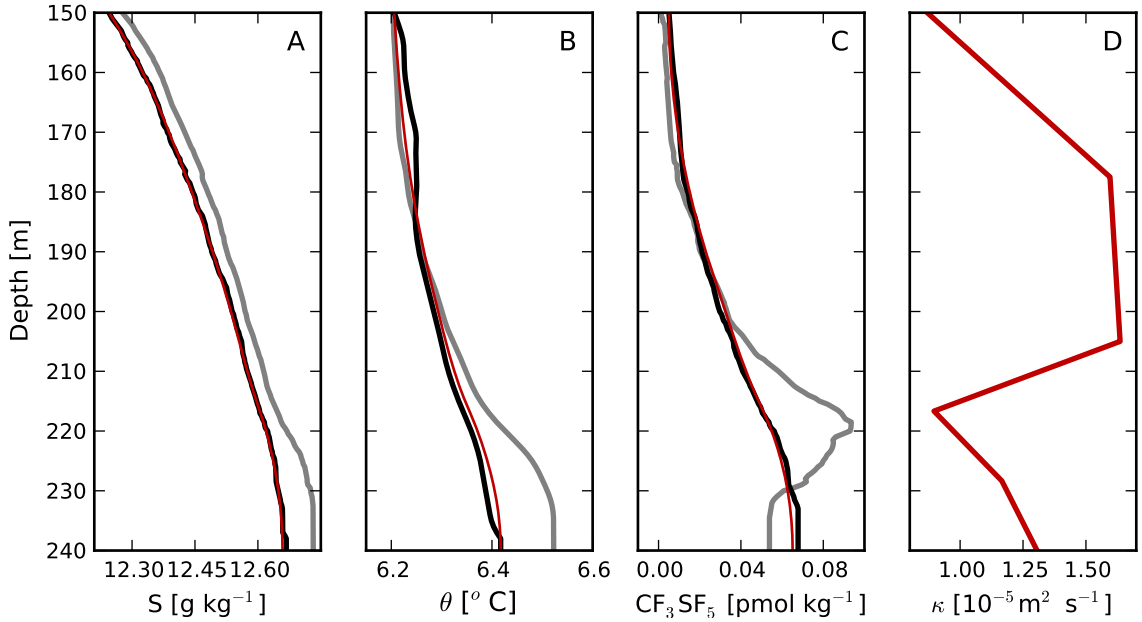

Figure 6.17.: Profiles of (a) salinity, (b) potential temperature , and (c) tracer concentration for Leg 3 (grey) and Leg 4 (black). In red: modelled profiles based on the diffusivity shown in (d).

also consistent with diffusivities computed from deep-water budgets for heat and salinity, using long-term moored CTD chains at C1 as discussed in more detail in Chap. 7. We have also optimised the diffusion problem with constant diffusivities (not shown), which still leads to very good fits. The corresponding values for the diffusivities are 1.3×10^{-5} m^2 s^{-1} for the period between Legs 3 and 4, and 1.9×10^{-5} m^2 s^{-1} for Legs 4 and 5.

6.5.5. Transition from interior to basin-scale mixing

While the results for Legs 3 to 5 suggest that the evolution of tracer, temperature, and salinity can be described rather accurately with the help of a one-dimensional diffusion model using identical diffusivities for all three variables, this was not the case for the period between Legs 2 and 3. This period was characterised by a transition from interior to boundary mixing during which additional processes may have affected the tracer spreading in different ways.

In order to illustrate the problem, we discard the assumption of identical diffusivities for all quantities, still assuming, however, that lateral intrusions are absent: $\bar{w} = 0$ in Eq. (6.3). In contrast to Legs 3 to 5 described above, now the tracer diffusivity κ_{SF5} is optimised independently of $\kappa_\theta = \kappa_S$ which are used to model the evolution of θ and S. Fig. 6.19a,b illustrates that with these additional assumptions, the diffusion model yields good agreement between measured and modelled profiles for temperature and salinity. The corresponding diffusivity κ_θ is a few times 10^{-5} m^2 s^{-1}, somewhat larger than the values found for Legs 3 to 5 but still plausible because the period between Legs 2 and 3 corresponds to the stormy winter months October-January (as shown in Chap. 7, diffusivities derived from the change of the salinity and temperature budgets predict a similar increase during the winter months). Again, the vertical structure of κ_θ, with a minimum at 220-230 m depth, is similar to the tracer profiles shown in Figs. 6.17d and 6.18d above.

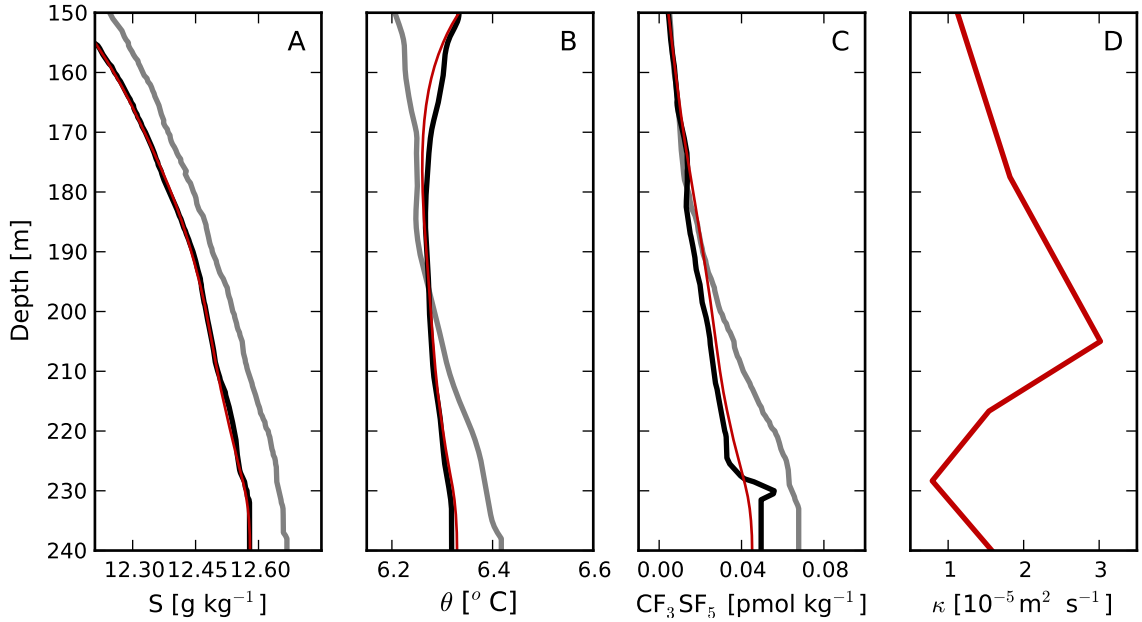

Figure 6.18.: As in Fig. 6.17 but now for the period between Leg 4 (grey) and Leg 5 (black).

However, as shown in Fig. 6.19d, the diffusivities κ_{SF5} and κ_θ exhibit completely different vertical structures, locally differing by more than an order of magnitude. As a result, using κ_{SF5} to model θ and S, or vice-versa κ_θ to model the tracer profile, completely unrealistic profiles are obtained (Fig. 6.19a-c). The problem can be traced back to the fact that between Legs 2 and 3 more than 40 percent of the tracer are lost through the upper boundary of the integration volume (at 150 m, see Fig. 6.15). Modelling this tracer loss as a diffusion process requires unrealistically high diffusivities at the upper boundary (Fig. 6.19d) because local tracer gradients are very small in this region. These results indicate that the description of the problem as a pure diffusion process is an over-simplification during the transition phase.

We have investigated several alternative processes that may have caused the strong vertical redistribution of tracer between Legs 2 and 3, and the associated tracer loss. The possibility of tracer loss due to particle adsorption and sinking to the sediment can be excluded because: (a) comparison of Figs. 6.8a and 6.9a shows no evidence for a relative motion between the tracer peak and the target isopycnal ($\sigma_\theta = 9.92$ kg m^{-3}), and (b) Fig. 6.9 suggests that tracer concentrations *decrease* towards the sediment, contrary to what would be expected if a large part of the tracer had sunk to the sediment surface. We have also examined the potential effect of deep-water renewal due to small lateral intrusions that may have remained undetected in temperature and salinity. This was motivated by the observation that interleaving of tracer-free fluid into layers above the tracer peak could have resulted in the observed strong reduction of concentrations, and in an advective tracer loss across the upper boundary of the control volume due to isopycnal divergence. For these investigations, we have solved equation Eq. (6.3), assuming different configurations with $\bar{w} \neq 0$ and $c_{\mathrm{in}} = 0$ in order to mimic the effect of intrusions. Observed tracer profiles could only be reproduced if the intruding fluid volume was of the order of the total deep-water volume, or, in other words, if a major deep-water inflow had occurred. It is highly unlikely that such an event would have remained unnoticed in both our CTD data and the BaTRE mooring array. If inflows would have had happened in such volumes they would

have been registered at the A1 upstream of the Gotland Basin but a comparison between the A1 and two uppermost C1 sensors did not show any hints (Chap. 6.6).

In the following, we suggest that the failure of the diffusion model during the transition phase is based on its inability to represent non-local transport effects. To this end, it should be recalled that "boundary mixing" involves a number of sub-processes essential for the overall basin-scale effect: (i) smoothing of cross-slope gradients inside the BBL (this is the actual mixing process); (ii) exchange of fluid between the BBL and the interior; and (iii) homogenisation of isopycnal tracer variability in the interior by meso-scale motions. If the time scales of processes (ii) and (iii) are small compared to (i), only small isopycnal concentration differences are expected between the interior and the BBL (Fig. 6.20a), implying that diapycnal gradients in the BBL and the interior are nearly identical. In this case, cross-slope mixing in the BBL determines the basin-scale vertical transport. Contrary, if upslope mixing in the BBL occurs much faster than the exchange processes (ii) and (iii), isopycnal concentrations gradients build up between the BBL and the interior. Via intrusions, these gradients drive an isopycnal tracer flux q_c between the BBL and the interior that may have no relation to the local vertical tracer gradient in the interior (Fig. 6.20b). The bottle-neck for basin-scale vertical transport in this case is the exchange between BBL and interior, rather than cross-slope mixing inside the BBL, which constitutes a *non-local* transport mechanism that cannot be described by a diffusion model based on *local* mean gradients. For example tracer may leave the basin via the BBL without being noticed in the interior, which may explain the strong tracer loss between Legs 2 and 3.

Support for this hypothesis comes from Fig. 6.9 (Leg 3), in which tracer samples taken within 2 m distance from the bottom are marked in green. BBL concentrations near the tracer peak are seen to be consistently smaller than the isopycnal average, whereas concentrations higher up in the water column show the opposite behaviour. In agreement with the schematic view in Fig. 6.20b, this suggests that tracer is lost from the interior towards the BBL near the tracer peak, diffused upslope inside the BBL, and finally injected into higher layers. The separation between the two regions is located around 210 m depth. The effect is even more pronounced for Leg 2 (Fig. 6.8), where data suggest that the asymmetric downward spreading of the tracer (higher concentrations below the peak than above) is an indication for the beginning influence of boundary mixing. It is therefore likely that isopycnal concentration differences between the BBL and the interior characterise the whole transition period between Legs 2 and 3.

6.5.6. Horizontal diffusivity

Following *Ledwell and Watson* (1991), an estimate of the lateral diffusivity may be obtained from the evolution of the lateral second moment, σ_H^2, relative to the centre of mass of the tracer distribution. If the lateral tracer spreading can be represented as a diffusion process, the increase of σ_H^2 is directly proportional to the corresponding diffusivity:

$$\frac{\mathrm{d}\sigma_H^2}{\mathrm{d}t} = 2\kappa_H \ , \tag{6.6}$$

which is analogous to Eq. (6.5) above. From the theory of diffusion processes, it is well-known that κ_H is scale-dependent (proportional to σ_H) unless the size of the tracer patch has grown much larger than the integral scale of the horizontal motions determining the spreading rates (e.g., *Kundu and Cohen*, 2008).

For Leg 2, before the tracer has touched the lateral slopes, we estimate $\sigma_H^2 = 92$ km^2 based on the vertically integrated tracer distribution shown in Fig. 6.3a. Using this value, and assuming that the lateral tracer variance during the injection is negligible compared to Leg 2, integration

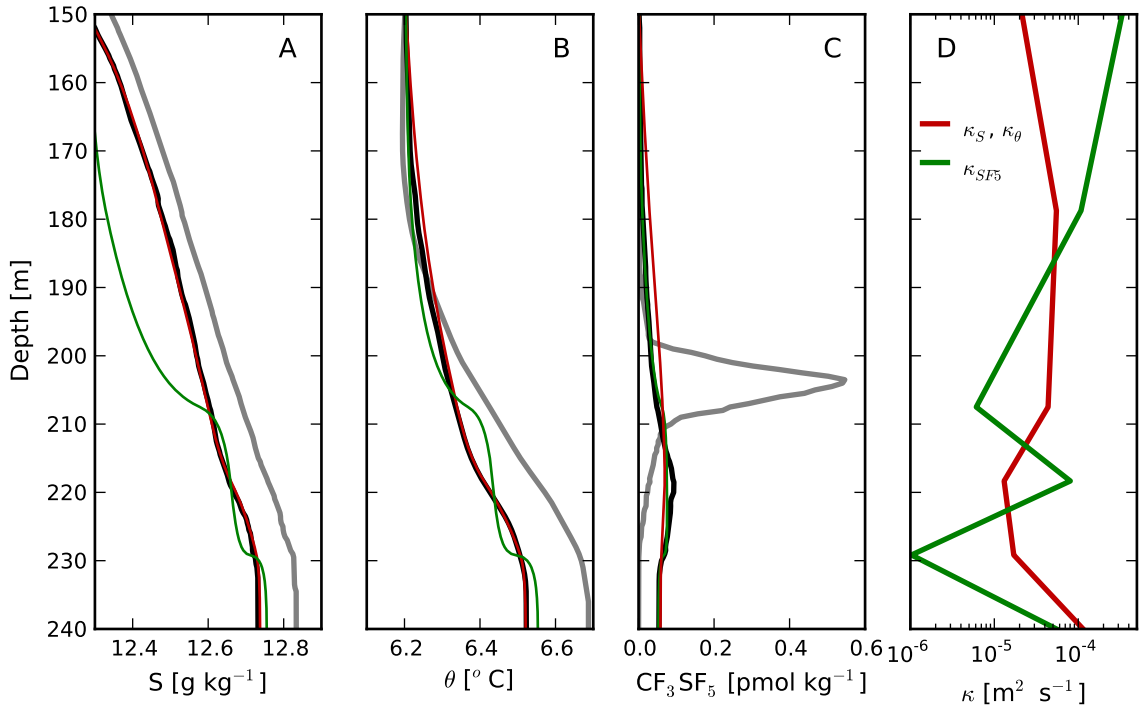

Figure 6.19.: Profiles of (a) salinity, (b) potential temperature, and (c) tracer for Leg 2 (grey) and Leg 3 (black). Red and green curves in (a)-(c), respectively, represent model results using the corresponding diffusivities shown in (d).

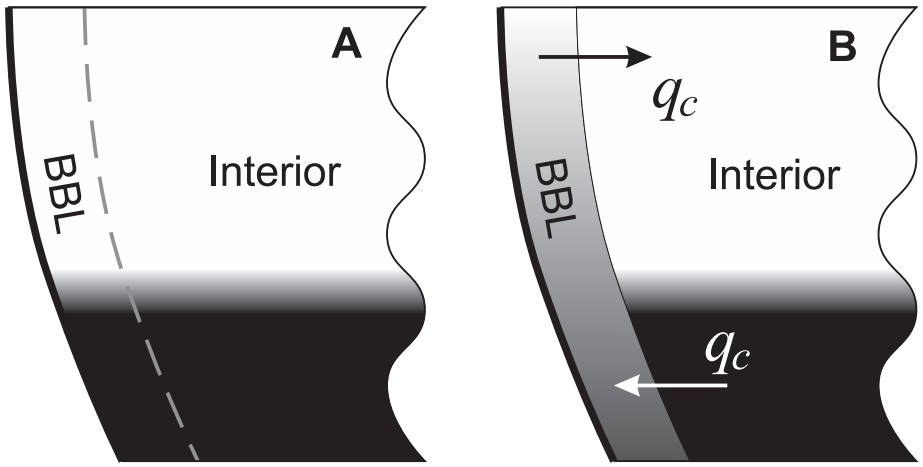

Figure 6.20.: Schematic view of tracer concentrations (in grey) in a stratified basin with (a) slow upslope mixing inside BBL, or rapid exchange between BBL and interior, and (b) rapid upslope mixing inside BBL, or slow exchange between BBL and interior.

of Eq. (6.6) yields $\kappa_H = 13$ m^2 s^{-1} if scale independence is assumed. This may be compared to $\kappa_H = 23$ m^2 s^{-1}, obtained if K_H is assumed to be proportional to σ_H. In view of the many uncertainties in the model and the method to estimate the second moments it does not seem justified to conclude much more than that the lateral diffusivities are of the order of 10 m^2 s^{-1} on scales of the order of 10 km. These values are comparable to the estimates obtained by *Ledwell and Watson* (1991) for the Santa Monica Basin, suggesting that comparable mesco-scale dispersion mechanisms are responsible for the lateral tracer spreading. *Reissmann* (2005) has emphasised the ubiquitous nature of meso-scale Baltic Sea eddies ("Beddies") in the Gotland Basin, but their impact on lateral mixing has not been studied in detail so far.

6.6. Inflows

The question if, and with what volume inflows happened during the BaTRE campaign can unfortunately not be answered in a complete satisfactory way. As mentioned in Chap. 6.5.5, the optimisation of the Leg2 – Leg 3 profiles of salinity, temperature and CF_3SF_5 profiles with a depth-dependent diffusivity and inflowing water gave reasonable fits for all three profiles but the inflow volumes needed for theses fits ranged between 100 and 300 km^3. These amounts are comparable or even larger than the basin volume of 150 km^3 below the 150 m isobath. Such amounts of water would be major inflows. In contrast to these results, the A1 mooring data, which measured velocity, T and S in 120 m depth upstream of the Gotland Basin (Fig. 5.1) shows that the salinity (and thus density) at the A1 mooring never exceeded the salinities in 167 m depth at the C1 mooring and only rarely the salinities in 147 m, Fig. 6.21a. Since inflows have to pass the A1 mooring, the measurements show that the water was simply not dense enough to penetrate the deeper Gotland Basin. This states that inflows as they have to be assumed by the optimisation problem have most likely not happened. The measurements indicate on the other hand, that small scale intrusions into the Gotland Basin might have happened above 170 m. Furthermore it can be seen in Fig. 6.21b that in May 2008 warm intrusions arrived at the A1 station but not the C1 station in 147 m. This water must have levelled in depths above 150 m, in agreement with the methane measurements in August 2008 of *Schmale et al.* (2010) who monitored a methane minimum (=inflowing water) between 80 and 140 m at the A1 and C1 locations.

6.7. Conclusions

Apart from the pilot study by *Ho et al.* (2008), the compound CF_3SF_5, on which our experiment was based, has not been previously used in TREs, and only limited knowledge exists about its performance in real-ocean applications. In our case, the tracer has proven to be long-term stable with no discernible sinking effects due to particle adsorption even under permanent anoxic conditions and high concentrations of H_2S, which forms a solid basis for future experiments.

As one of the key results of our study, the different spreading rates observed before and after the tracer was in contact with the lateral slopes of the basin provide strong evidence for the importance of boundary mixing. Similar to previous tracer experiments conducted in stratified lakes (*Goudsmit et al.*, 1997) and ocean basins (*Ledwell and Hickey*, 1995; *Ledwell and Bratkovich*, 1995), we find an order-of-magnitude difference between interior and basin-scale effective diffusivities. While this suggests a qualitative similarity between the different experiments, it should be noted that the diffusivities found in the Gotland Basin (interior: $\sim 10^{-6}$ m^2 s^{-1}, basin-scale: $\sim 10^{-5}$ m^2 s^{-1}) are an order of magnitude smaller than the corresponding values found by *Ledwell and Hickey* (1995) for the Santa Monica Basin. It is

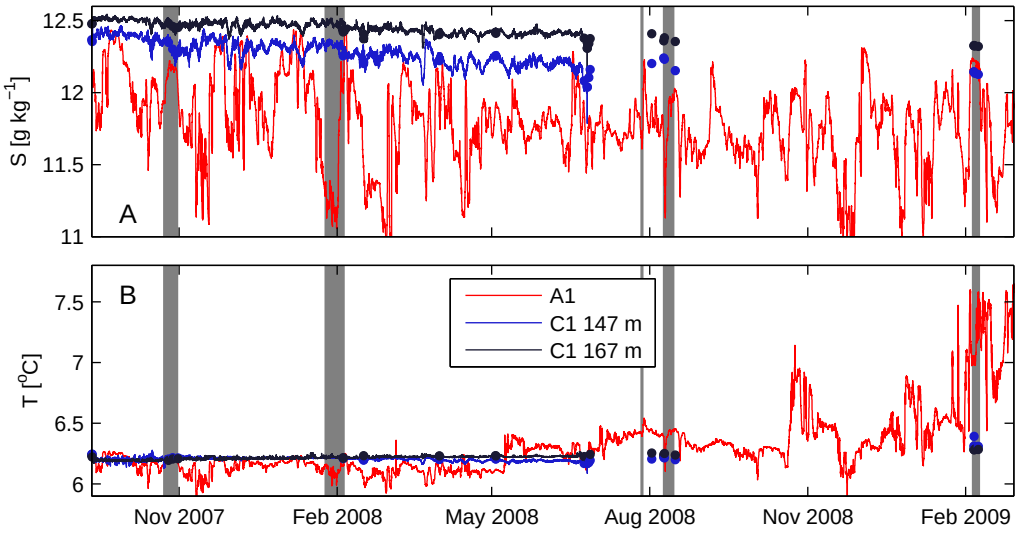

Figure 6.21.: Salinity (a) and temperature (b) from the A1 mooring, C1 moorings and CTD profiles (points) interpolated to the C1 depths. Gray areas indicate the BaTRE surveys.

likely that this discrepancy mirrors different mixing mechanisms and energy levels associated with the processes near the lateral slopes. *Ledwell and Hickey* (1995) speculate, e.g., that the critical reflection of internal tides at sloping topography may be an important energy source for boundary mixing, which is certainly not the case in the virtually tideless Baltic Sea. The analysis in Chap. 7 confirms the importance of boundary mixing from direct microstructure observations, and suggests basin-scale topographic waves as the primary energy source for this process.

Finally, it is important to note that the dominance of boundary mixing implies that the observed tracer spreading in the interior is a result of isopycnal motions associated with the exchange of boundary-layer and interior fluid. Our results have shown that the physical mechanisms governing these exchange processes may be crucial for the basin-scale vertical distribution of matter. However, they are not well understood at the moment, pointing at future work.

7. BaTRE Part II: Mixing Processes

7.0.1. Temporal variability of mixing

Previous studies (*Schneider et al.*, 2010; *Wieczorek et al.*, 2008; *Axell*, 1998; *Stigebrandt*, 1987) have used the budget method (Chap. 6.5.1) to estimate turbulent diffusivities in the Baltic Proper based on individual CTD profiles. In view of the strong fluctuations apparent in both salinity and temperature (see Fig. 5.5b,d), however, the low temporal resolution of this approach is likely to introduce aliasing effects. Here, we exploit the availability of long-term mooring data with high resolution in time, and estimate the volume-averaged salinity from

$$\langle S \rangle_V = \frac{1}{V} \int_{z_b}^{z_t} S(z) A(z) \, \mathrm{d}z \,, \tag{7.1}$$

where we integrate from the bottom, z_b, to the top, z_t, of the control volume, using the hypsographic relation for $A(z)$ suggested by *Hagen and Feistel* (2001). $S(z)$ was computed from the precision CTD loggers at station C1 in the centre of the basin (Fig. 6.1), assuming horizontally homogeneous properties. The heat budget was computed analogously, and, in a similar way, the first vertical moment of the density appearing in (Eq. (3.26)) was evaluated. As above, we identify the filtering operator $\langle \cdots \rangle_T$ with a 30-day low-pass filter to eliminate short-term reversible fluctuations from the time series. The time derivatives appearing in (Eq. (3.25)) and (Eq. (3.29)) are evaluated from the slopes of a straight-line fit, using a window of 70 days. These filtering windows are based on the results of the spectral analysis discussed in more detail below, and proved to be a reasonable compromise between high temporal resolution and sufficient damping of short-term reversible fluctuations.

Fig. 7.1 provides a composite view of wind forcing, deep water current fluctuations, and mixing parameters for the grey-shaded time interval in Fig. 5.6. Clearly visible is a strong correlation between wind forcing (Fig. 7.1a), and fluctuating kinetic energies, $|\tilde{\mathbf{u}}|^2$, at both central (Fig. 7.1b) and boundary stations (Fig. 7.1c). This correlation is evident from the seasonal scale with low energy levels in summer down to the scales of individual wind events. Also the turbulent diffusivities (Fig. 7.1d) and dissipation rates (Fig. 7.1e) follow the seasonal pattern of the forcing, confirming an earlier conclusion by *Axell* (1998) that deep water mixing in the Baltic Proper is stronger during the cold season. In spite of strong temporal fluctuations, turbulent diffusivities for temperature and salinity are within a factor of two everywhere (and often closer), which lends some credibility to the method we use. Diffusivities decrease with depth, and show a strong variability in time with maximum values around 6×10^{-5} m^2 s^{-1} during the windy periods in January and February, and a breakdown by almost one order of magnitude at the end of the winter period. These results are in excellent agreement with the values and the vertical structure of the basin-scale diffusivities inferred from a one-dimensional diffusion model of tracer, temperature, and salinity (Chap. 6).

Volume-averaged dissipation rates computed from Eq. (3.29) span a range from approximately 5×10^{-9} W kg^{-1} in winter down to a few times 10^{-10} W kg^{-1} in May. Note, however, that if most of the mixing takes place in the BBL, as suggested by the results discussed in Chap. 6, BBL dissipation rates are likely to be larger by at least one order of magnitude because (a) BBL dissipation occurs only in a fraction of the total basin volume, and (b) the mixing efficiency in

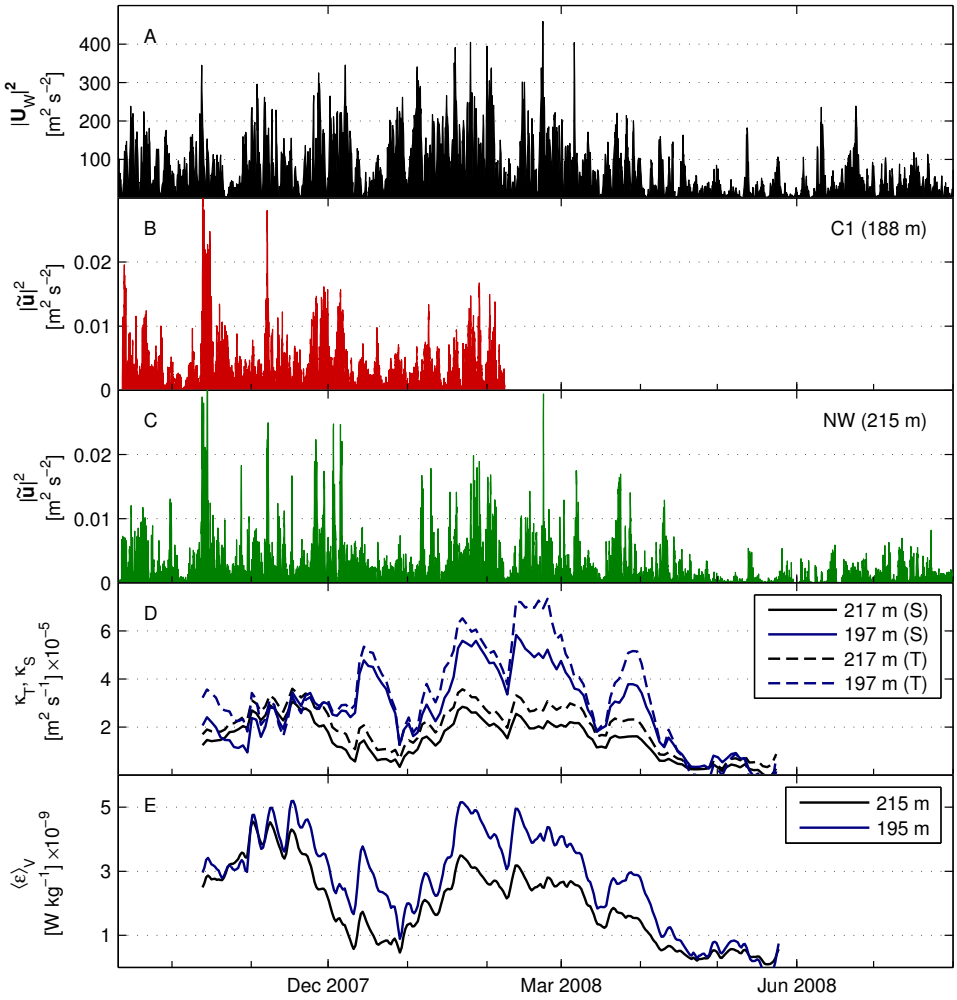

Figure 7.1.: Time series of (a) square of the wind speed; (b) fluctuating kinetic energy $|\tilde{\boldsymbol{u}}|^2$ (b) at position C1, and (c) at position NW; (d) turbulent diffusivities; and (e) volume-averaged dissipation rates. The time interval shown here corresponds to the grey-shaded area in Fig. 5.6.

the BBL is likely to be substantially smaller than $\gamma = 0.2$.

Beyond previous studies, our moored data also suggest a clear correlation between surface forcing, kinetic energy in deep-water motions, and deep-water mixing rates on time scales down to individual wind periods. Examples for this include the reduction of the wind stress during two calm periods in February and March 2008 (Fig. 7.1a), where the associated reduction of the deep-water kinetic energies (Fig. 7.1b,c) is accompanied by a collapse of the mixing parameters shown in Fig. 7.1d,e. These data suggest that the energy provided by the wind stress on the largest scales quickly passes to the smallest scales, where mixing occurs and energy is dissipated. The chain of processes involved in this energy transfer is examined in the following.

7.1. Analysis of deep-water motions

7.1.1. Spectral analysis

Key information about the physical processes dominating the deep-water motions can be inferred from the spectral decomposition of the fluctuating velocity records at C1 in the centre of the basin. Here, we focus on the more energetic winter period, corresponding to the full velocity record shown in Fig. 7.1b, where most of the seasonal mixing was found to occur.

Rotary spectra displayed in Fig. 7.2a reveal that the energy distribution is dominated by two fundamentally different types of motion, separated by a well-defined spectral gap at approximately 20 h: (a) subinertial motions with counter-clockwise rotating velocity vectors dominating the broad energy peak centred at approximately 100 h; and (b) internal-wave motions with clockwise rotating velocity vectors near the inertial frequency. The cumulative distribution of the total kinetic energy (Fig. 7.2b) reveals that most of the energy (64 percent) is contained in the subinertial motions, whereas the internal-wave band, energetically dominated by near-inertial motions, contributes about 27 percent.

Total kinetic energy levels in the centre (C1) and near the slope (NW) of the basin are compared to the canonical Garrett-Munk spectrum (GM79, *Munk*, 1981) in Fig. 7.3a. Spectra from the slope and central stations, respectively, are remarkably similar, except for intermediate frequencies in the internal wave band, where enhanced energy levels at NW point to a possible source of internal wave generation near the slope. Observed spectral slopes approximately correspond to GM79 (evaluated for the observed range of local buoyancy frequency) but energy levels are more than an order of magnitude lower.

Isopycnal displacements, $\zeta = \tilde{b}/\langle N^2\rangle_T$, were computed from local buoyancy fluctuations, $\tilde{b} = b - \langle b\rangle_T$, where the buoyancy is defined as $b = -g(\sigma_\theta - \rho_0)/\rho_0$. The low-pass filtered buoyancy frequency $\langle N^2\rangle_T$ (30 days) was obtained from central (for C1) or one-sided (for NW) vertical finite differencing of densities, depending on the availability and position of moored CTD loggers. Displacement spectra (Fig. 7.3b) illustrate substantially stronger isopycnal excursions near the slope at sub-inertial frequencies, which, similar to the observations made by *Hickey* (1991) in two deep basins off the Californian Coast, is likely to reflect the up- and downslope advection of salinity and temperature by sub-inertial motions (Fig. 7.3a). Spectral levels in the internal-wave band are similar at both locations (Fig. 7.3b), with spectral shapes closely corresponding to GM79 but, as for the kinetic energies, with energy levels reduced by approximately one order of magnitude.

Concluding, the spectral analysis suggests that motions in the frequency band between f and N are consistent with internal-wave motions with strongly reduced energy levels compared to the open ocean. The, by far, largest part of the kinetic and potential energies, however, was found to be contained in counter-clockwise polarised sub-inertial motions with a period of a few days. Since previous studies have either focused on the deep-water rim current (*Hagen and Feistel*, 2004, 2007) or on internal-wave breaking (*Axell*, 1998) as the primary energy sources for deep-water mixing, this is a key result suggesting further analysis of the role of sub-inertial motions for mixing.

7.1.2. Spatial coherence

In order to identify spatially coherent patterns in the two types of motions identified in the previous section, we performed an empirical orthogonal function (EOF) analysis of the observed velocities. For this method, the velocity field is written in complex notation, $U(\mathbf{x}, t) = u(\mathbf{x}, t) + \imath v(\mathbf{x}, t)$ ($\imath$ is the imaginary unit), and then decomposed into a set of complex orthogonal eigenvectors

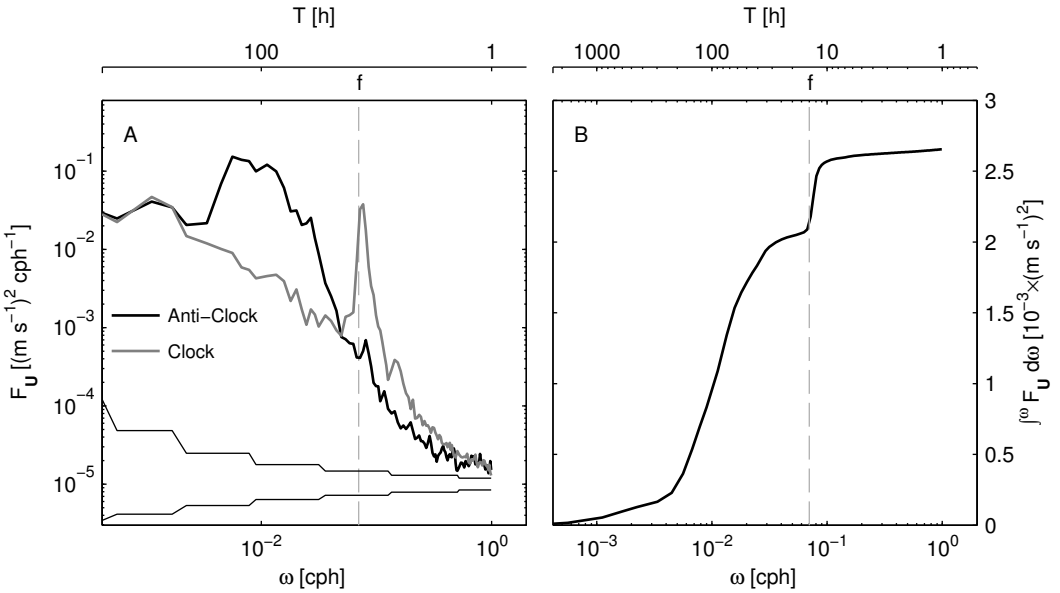

Figure 7.2.: (a) Clockwise and anti-clockwise rotary velocity spectra with 95-percent confidence limits, and (b) cumulative energy spectrum, both shown for position C1 (208 m depth). Time interval corresponds to that shown in Fig. 7.1b. Vertical line marks the inertial frequency. Frequencies near $N = 3$–4 cph are not resolved.

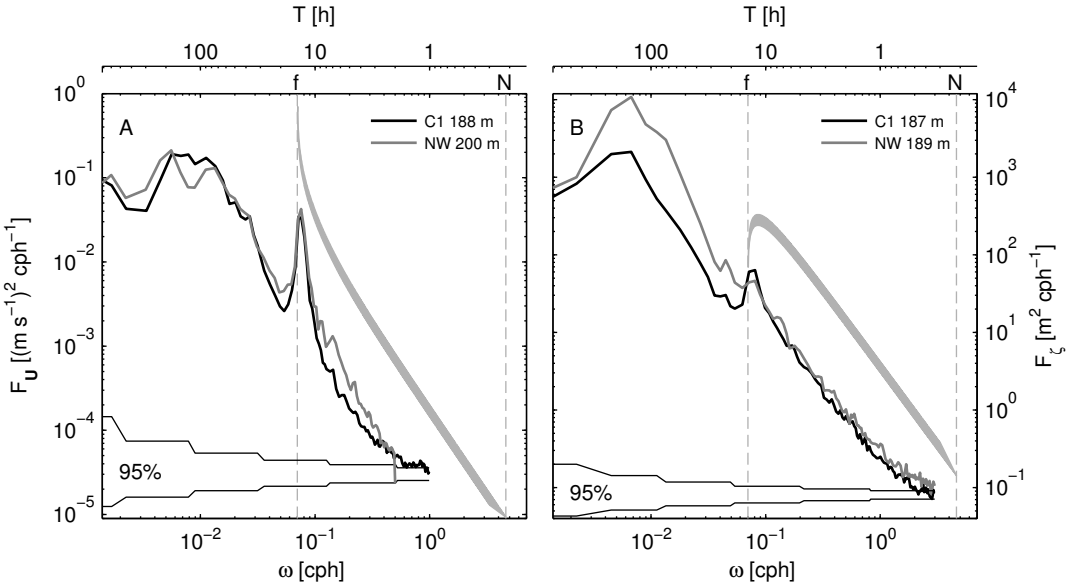

Figure 7.3.: Spectra of (a) horizontal velocity, and (b) isopycnal displacements for stations C1 and NW. Thick grey-shaded lines denote corresponding Garrett-Munk spectra (GM79) for the range of N observed during the total period. Vertical dashed lines mark the internal-wave band between f and N.

$\Phi_k(\mathbf{x})$, and corresponding complex amplitudes $a(t)$ (*Kundu and Allen*, 1976; *Kaihatu*, 1998). In discrete form, this yields

$$U(\mathbf{x}_i, t) = \sum_{k=1}^{n} a_k(t)\Phi_k(\mathbf{x}_i) \ , \tag{7.2}$$

where $\mathbf{x}_i = (x_i, y_i, z_i)$ denotes the positions of the i current meters, and n the total number of modes. For the following analysis, it is important to note that, although the absolute directions of the eigenvectors are only known within a constant factor, the *relative* direction of eigenvectors with respect to each other is uniquely determined by the method (*Kaihatu*, 1998).

Velocities at 4 moorings (C1, NE, NW, SW) are available from 11 September 2007 until 01 February 2008 at the depth levels given in Tab. 5.3 (ADCP data were averaged into 3 equally spaced bins). Using the results of the spectral analysis above, the complex velocity $U(\mathbf{x}_i, t)$ is band-pass filtered between 300 and 24 hours to extract the sub-inertial motions $U^{SI}(\mathbf{x}_i, t)$, and between 20 to 8 hours to isolate the near-inertial motions $U^{NI}(\mathbf{x}_i, t)$.

7.1.3. Sub-inertial motions

The structure of the complex eigenvector $\Phi_1^{SI}(\mathbf{x}_i)$ of the first mode is displayed in Fig. 7.4a. First, it is important to note from the local correlation coefficients specified in this figure that mode 1 exhibits about 90 percent correlation with the observed sub-inertial velocities at positions C1 and SW, about 80 percent at position NW, but only approximately 50 percent at position NE. Therefore, at least for C1, SW, and NW, mode 1 completely dominates the velocity field in this frequency band, such that it is unlikely that higher modes contain significant information. From the structure of the eigenvectors in Fig. 7.4a we conclude that there is virtually no directional (phase) difference, neither vertically nor laterally, and that amplitude differences are within a factor of two for all positions except NE. Mode 1 therefore describes a nearly slab-like motion of the deep-water volume with no discernible vertical shear.

The complex amplitude a_1^{SI} corresponding to mode 1 is shown in Fig. 7.5 together with the wind speed for the complete record length. This figure suggests that, in direct response to enhanced wind forcing, deep-water motions with anti-clockwise rotating velocity vectors and speeds of the order of 0.1 m s^{-1} are initiated. Combining this information with the spectral analysis discussed above we conclude that the sub-inertial deep-water variability is dominated by motions with anti-clockwise rotating velocity vectors that are highly correlated across the whole basin, except at position NE. These motions have a period of a few days, and appear to have a damping time scale of the same order, as evident from the fact that sub-inertial motions decay almost immediately at the end of individual wind events (Fig. 7.5a,b). An interesting special case, in which this strong damping is compensated by resonant wind forcing is shown in Fig. 7.6, focusing on period I at the beginning of the record as indicated in Fig. 7.5. During this time, the north component of the wind speed shows a clear periodicity with periods between 2 and 3 days, which is seen to be directly mirrored in correlated sub-inertial motions with the same frequency (Fig. 7.6b,c). Near-inertial waves generated at the sloping sides of the basin are seen to arrive with a phase shift in the centre, as seen most clearly in the period 17-21 September. After the 18 September sub-inertial motions increase to their maximum while near-inertial motions already start to decay (Fig. 7.6c,d).

These results can be used to draw some conclusions about the physical processes that determine the sub-inertial velocities. In this frequency band, meso-scale eddies (*Reissmann*, 2005), and Kelvin-type waves (e.g., *Umlauf and Lemmin*, 2005; *Appt et al.*, 2004) are frequently observed phenomena in stratified basins of comparable size. However, because the lateral scale of both types of processes is of the order of the internal Rossby radius (which is much smaller than

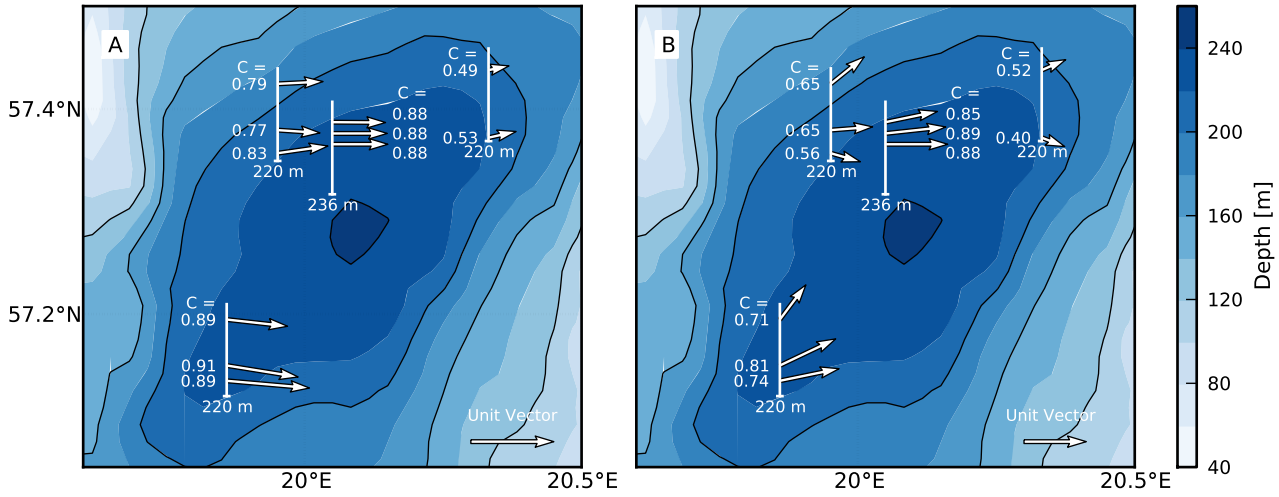

Figure 7.4.: Enlarged view of Gotland Basin (see Fig. 6.1) with results of the EOF analysis: Eigenvectors of first EOF-mode computed for (a) sub-inertial motions (Φ_1^{SI}), and (b) near-inertial motions (Φ_1^{NI}). Height above bottom corresponds to position on the white lines (their total length corresponds to 60 m). Phase angles are seen from top. Local correlation coefficients C (see text) are indicated to the left of the eigenvectors. The total time interval used for the analysis corresponds to that shown in Fig. 7.1b.

the lateral scale of the basin), neither can explain the observed basin-sale correlation. Eddies are not correlated over many Rossby radii, and Kelvin waves are confined to the lateral boundaries within one Rossby radius, and would therefore not cause a significant signal at position C1 in the centre, contrary to what is shown in Fig. 7.5.

In the absence of other periodic processes in this frequency band, we suggest that basin-scale topographic waves determine the sub-inertial deep-water variability. Such topographic modes show a basin-scale correlation, have typical periods of a few days, and exhibit counter-clockwise rotating velocity vectors (*Stocker and Hutter*, 1992; *LeBlond and Mysak*, 1978). In particular the observations and analysis of counter-clockwise rotating motions in Lake Michigan by *Saylor et al.* (1980) exhibit strong similarities with our study site because both basins are of comparable size. Indications for topographic basin-scale waves have also been found by *Hickey* (1991), who studied deep-water motions in two basins off the Californian coast. The strong damping mentioned above, and the period that is of the order of the meso-scale atmospheric variability, suggest, however, that we are observing strongly forced and damped motions rather than freely propagating basin-scale topographic waves. This may explain why our analysis did not show any hints for a phase propagation, e.g. along the boundary stations NE, NW, and SW.

7.1.4. Near-inertial motions

The structure of the first EOF for motions in the near-inertial wave band is illustrated in Fig. 7.4b. Also in this case, the first mode suggests a basin-scale correlation (explained variance: 65 percent), with local correlation coefficients, however, somewhat smaller than for the sub-inertial motions. Contrary to the latter, the mode-1 eigenvectors for the near-inertial frequency band (Fig. 7.4b) suggests a clear vertical phase shift at all moorings. Note that eigenvectors show

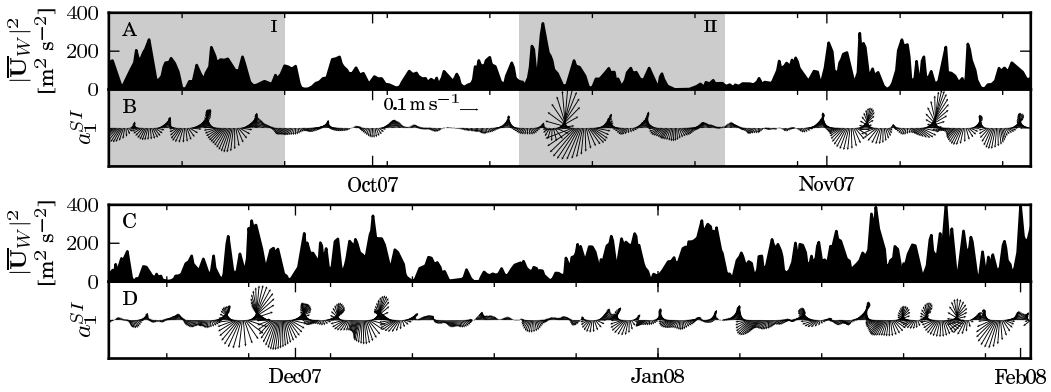

Figure 7.5.: Timeseries of (a) square of the wind speed, and (b) amplitude a_1^{SI} of first sub-inertial EOF mode (corresponding to eigenvectors in Fig. 7.4a). The grey-shaded areas indicate the periods shown in Figs. 7.6 and 7.7 below. Panels (c) and (d) are continuations of (a) and (b) respectively.

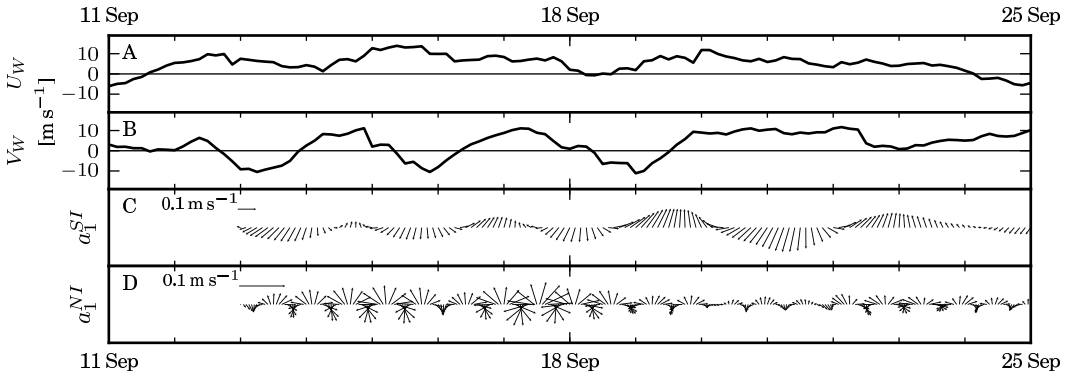

Figure 7.6.: Timeseries of (a) east-component and (b) north-component of wind velocity, amplitudes of (c) sub-inertial and (d) near-inertial first-mode EOF for period I shown in Fig. 7.5.

a clockwise veering towards deeper layers, which is indicative for upward phase propagation or downward energy propagation according to linear internal wave theory (*Gill*, 1982).

To investigate this aspect of near-inertial wave propagation in more detail, an enlarged view of the ADCP measurements for period II (see Fig. 7.5), is displayed in Fig. 7.7. While the wind event at the beginning of this period is seen to lead to an almost immediate generation of sub-inertial motions (Fig. 7.7a,b), the near-inertial signal arrives with a delay of 1-2 days (Fig. 7.7c). Available theory (*Kundu et al.*, 1983; *Fennel*, 1989) and some recent measurements in the Baltic Sea (*van der Lee and Umlauf*, 2011) suggest that these waves are generated at the lateral slopes during the wind event, and slowly travel downwards and towards the interior.

The observed motions have periods between 11 hours and the inertial period (Fig. 7.7d), and exhibit a phase shift of up to 2 hours over the ADCP sampling range (Fig. 7.7e). As pointed out above, this is consistent with the result of the EOF analysis, and indicative of a downward propagation of near-inertial energy. Previous authors, e.g. *Axell* (1998), have speculated that this mechanism provides the main energy source for deep-water mixing. From our measurements, we arrive at the following conclusions: (i) Near-inertial waves are unlikely to contribute significantly to frictional boundary mixing because their near-bottom velocities are much smaller compared than the sub-inertial motions and the rim current (see below); (ii) in contrast to this, internal-wave motions are a likely reason for the small-scale turbulent patches that were occasionally observed in our microstructure measurements. The importance of near-inertial waves for the interior mixing has been pointed out by *van der Lee and Umlauf* (2011) in a recent study of internal-wave mixing in the neighbouring Bornholm Basin, and it is likely that a similar process acts in the Gotland Basin as well. However, the results from the tracer experiment discussed in Chap. 6 have demonstrated that interior mixing is negligible compared to boundary mixing such that the role of wind generated near-inertial waves for mixing has probably been overestimated so far.

7.1.5. Internal wave properties

As pointed out in Chap. 3.4 the measured phase shifts and knowledge of the frequency can be used to calculate the vertical phase speed c_z. Fig. 7.7 depicts that the phase shift between the uppermost and lowermost (vertical distance of $\Delta z = 24$ m) valid ADCP bins does not exceed 2 hours. Observed phase velocities are thus $c_z \geq 24/(2 * 3600) = 0.003$ m s^{-1}. Using the measured kinetic energy, applying Eq. (3.43) where the total energy can be calculated from the kinetic energy by exploiting Eq. (3.31) and the vertical group speed by Eq. (3.41), yields a vertical energy flux F_z of the internal waves. To compare this energy flux with the measured budgets it is assumed that the total F_z dissipates in the volume below the measured flux and therefore $\varepsilon_{IW} = F_z A/V$. However, the results show that the energy flux strongly depends on the frequency (see also Fig. 3.5) and thus a precise knowledge of the frequency is necessary. The ε_{IW} is furthermore of the order of magnitude of the basin-scale dissipation rates, meaning that the internal wave flux alone would provide all the energy required for the observed mixing. This is doubtful since the more energetic sub-inertial motions certainly have their share on diapycnal mixing. We will thus discuss the drawback of the methods used and speculate about further studies with a different approach. The first remark is that only the easily measurable upward propagating phase shifts have been quantified. A possible reflection of internal waves is not considered at all. The estimation of ε_{IW} is therefore an upper limit. The second more general remark is about the limitations of the assumed WKB internal wave approach: The phases seen in the ADCP data are measured over the whole vertically resolved distance of 24 m, the vertical wavelengths of the internal waves are then at least 24 m; $l_m > 24$ m. The dispersion relation of internal waves together with c_z, N^2 and f as well as the frequency ω, gives the physically

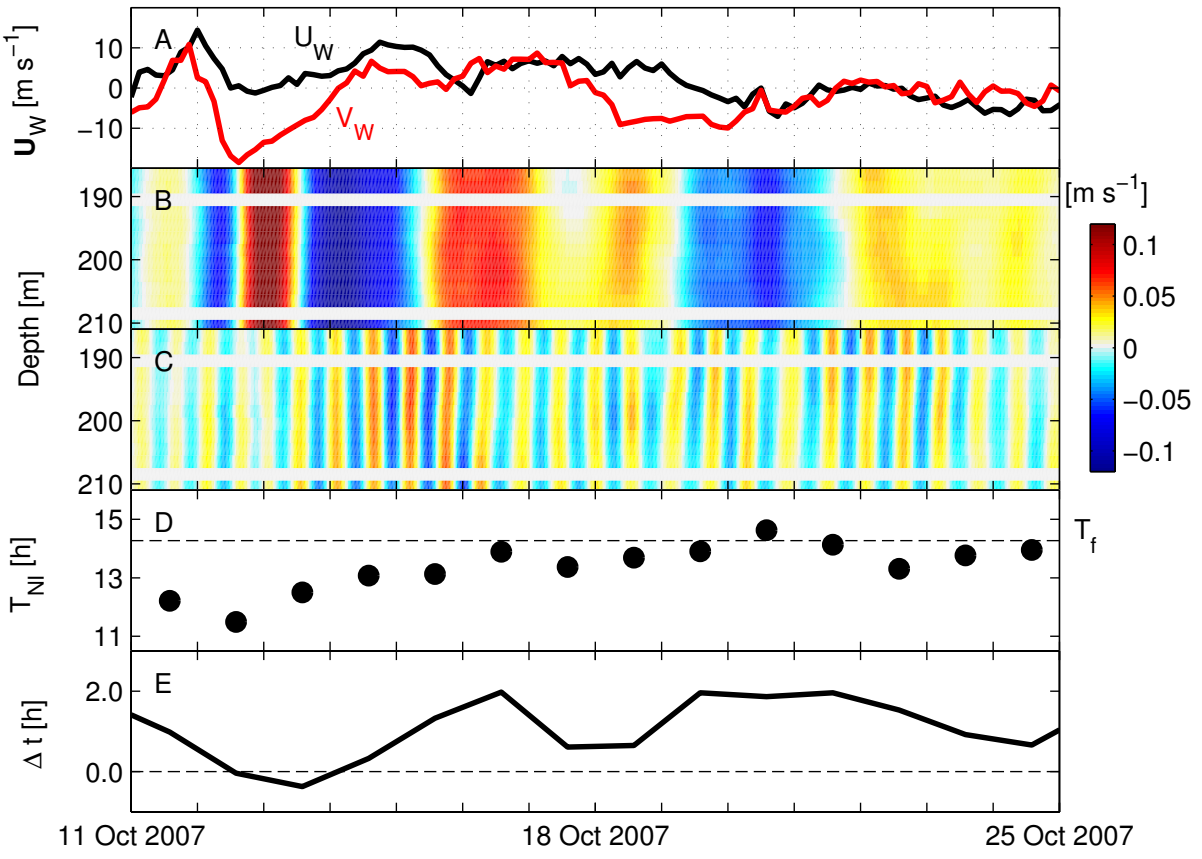

Figure 7.7.: Timeseries (position C1) of (a) east- and north-component of wind velocity (b) sub-inertial velocity u^{SI}, (c) near-inertial velocity u^{NI}; (d) local period of u^{NI} estimated from two-day segments of data in 210 m depth (see text); and (e) phase-lag in u^{NI} between lowermost and uppermost ADCP bin calculated from the phase shifts in first EOF eigenvectors for the same two-day segments. Dashed line in (d) indicates the inertial period T_f. Data correspond to period II shown in Fig. 7.5.

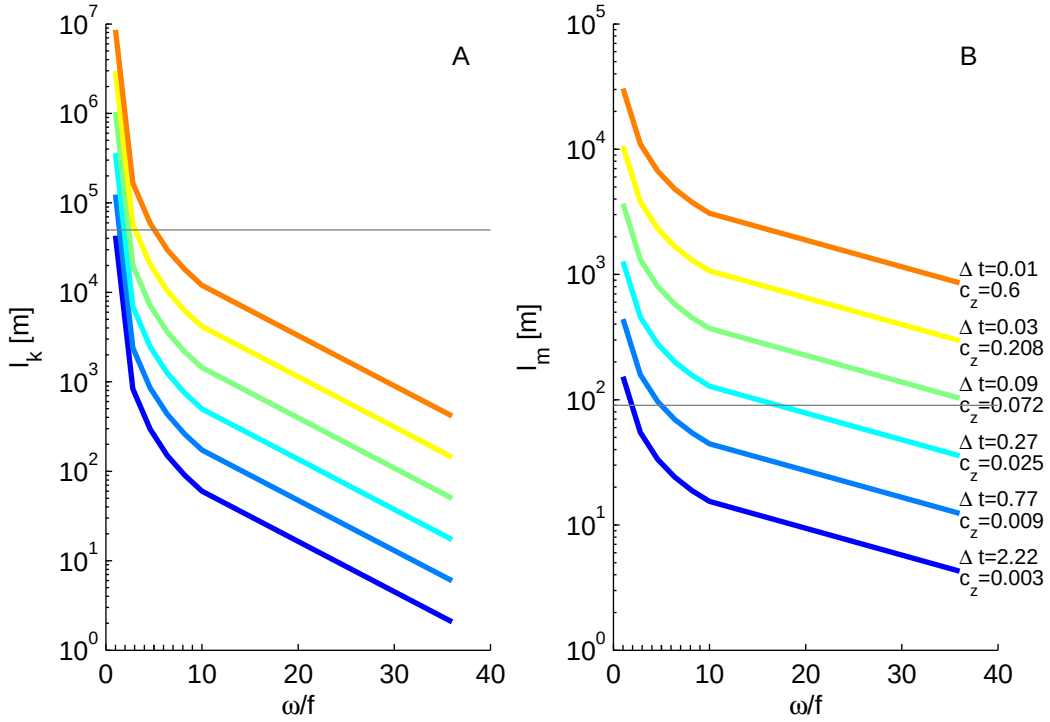

Figure 7.8.: Horizontal (a) and Vertical (b) wavelengths calculated from predefined vertical phase speed c_z, stratification $N^2 = 2.4 \times 10^{-5}$ s^{-2} and inertial frequency at 57°N. Numbers in (b) show the phase speeds and the phase lag Δt over 24 m in hours (for comparison with Fig. 7.7e). Grey lines indicate the approximate horizontal radius of the Basin in 150 m depth (50 km) and the vertical extension of the deeper basin (from 150 m to 240 m = 90 m).

possible horizontal and vertical wavelengths l_k, l_m. To get a general idea about the horizontal and vertical wavelengths that are possible in the Gotland Basin, especially in comparison with the basin size, theoretical wavelengths have been computed. These waves were given vertical phase speed between 0.003 m s^{-1} and 0.6 m s^{-1}, with varying frequencies ω and a typical stratification N^2 (Fig. 7.8). The vertical wavelengths in Fig. 7.8b, of the near inertial waves clearly show, that free internal waves with phase speeds larger than 0.025 m s^{-1} ($\Delta t = 0.27$h) have vertical wave lengths larger than 100 m. These waves simply do not fit into the basin and would, additionally violate the WKB criterion of vertical wavelengths being much smaller than the change of the stratification. Fig. 7.8a,b furthermore shows, that internal waves with frequencies above $10f$ and smaller than $c_z \approx 0.001$ m s^{-1} can be considered as free linear internal waves since the horizontal and vertical wavelength are small compared to the basin size and the change of stratification.

The importance of the near-inertial frequencies in terms of kinetic energy and their vertical wavelengths exceeding the depth of the basin make a WKB analysis dubious. An alternative is the modal analysis (Chap. 3.4.2). Here the modal analysis is limited to the calculation of the hydrostatic internal wave modes and a comparison with the ADCP data. As pointed out above, the phases of the measured near-inertial internal waves have vertical wavelengths longer than the range of the ADCP. The vertical range of the ADCP in comparison with the basin depth and the vertical extension of the internal wave modes is depicted in Fig. 7.9. Since the ADCP data did not show any zero crossings of the horizontal velocities within the ADCP range internal wave

modes showing a zero crossing within this range can be ruled out as dominant modes. These would be modes 5 and higher, Fig. 7.9e,f. This finding agrees with *van der Lee and Umlauf* (2011), who found, in their thorough analysis of internal wave modes in the Bornholm Basin, that the lowest three modes contained, on average, 81% of the total kinetic energy. Calculated "mode speed" and the derived Rossby radius of the mode $R_n = c_n/f$ also show that modes in the centre of the Basin are far away from the boundaries in terms of the R_n and are thus not influenced by them.

Summary and Outlook

The C1 ADCP data, as well as the EOF analysis, of all moorings show a tilting of internal wave phase lines, which is an indication of internal wave energy flux. Nevertheless, the small amount of available data restricted us to having to attempts to assess the vertical energy flux based on linear wave theory. A quantification of the internal-wave-induced energy flux as well as the shear-induced interior turbulence and the subsequent mixing makes internal wave investigations an interesting topic for future research. The majority of wave energy flux happens in frequency ranges in which the hydrostatic assumption can be applied, but it is probably wrong to assume free internal waves. Modal analysis suggests that the first 4 vertical modes are the dominant modes in the basin. Future field campaigns with the focus on internal waves should consider using the approach of writing the energy flux term in the form $\mathbf{F} = \langle p'\mathbf{u}' \rangle$, as described in Chap. 3.4. This would require continuous density measurements over the whole water column, but is less demanding in terms of velocity measurements compared to the phase shift method.

7.2. Bottom boundary layer mixing

Our analysis of BBL properties and mixing is based on CTD and shear-microstructure measurements with the MSS-90L profiler, performed during two of the tracer surveys described in Chap. 6. During Leg 2 234 profiles were obtained on 40 stations on 25 - 31 October 2007. During Leg 3 (28 January - 05 February 2008), we obtained 97 profiles on 23 stations. In both cases, microstructure measurements and tracer samples were taken on the same grid, with typically 4-5 full-depth microstructure casts measured within a period of approximately one hour.

7.2.1. Variability of boundary layer thickness

For each profile, we estimated the thickness of the well-mixed BBL from a simple criterion based on a threshold for density ($\Delta\sigma_\theta \leq 0.01$ kg m^{-3}) compared to the deepest point. These data allow us to estimate both the spatial distribution of BBL thickness and, by comparing maximum and minimum thicknesses at each station, the short-term variability of the BBL thickness (recall that station profiles are taken within only 60 minutes). The result of this analysis is shown in Fig. 7.10a,b. For both cruises, a systematic distribution is evident with large BBL heights in the flat central part of the basin, and thin BBLs on the slopes. Moreover, BBLs on the slope have a tendency for higher short-term variability. Since the above analysis of spatial patterns of the sub-inertial motions (which dominate near-bottom speeds) has not shown evidence for higher speeds in the centre, this points to a stronger tendency for BBL restratification on the slopes, and thus to a stronger exchange between the BBL and the interior. This is consistent with similar observations and modelling results for stratified lakes (*Gloor et al.*, 2000; *Becherer and Umlauf*, 2011; *Lorrai et al.*, 2011), with some important consequences for mixing as shown in the following.

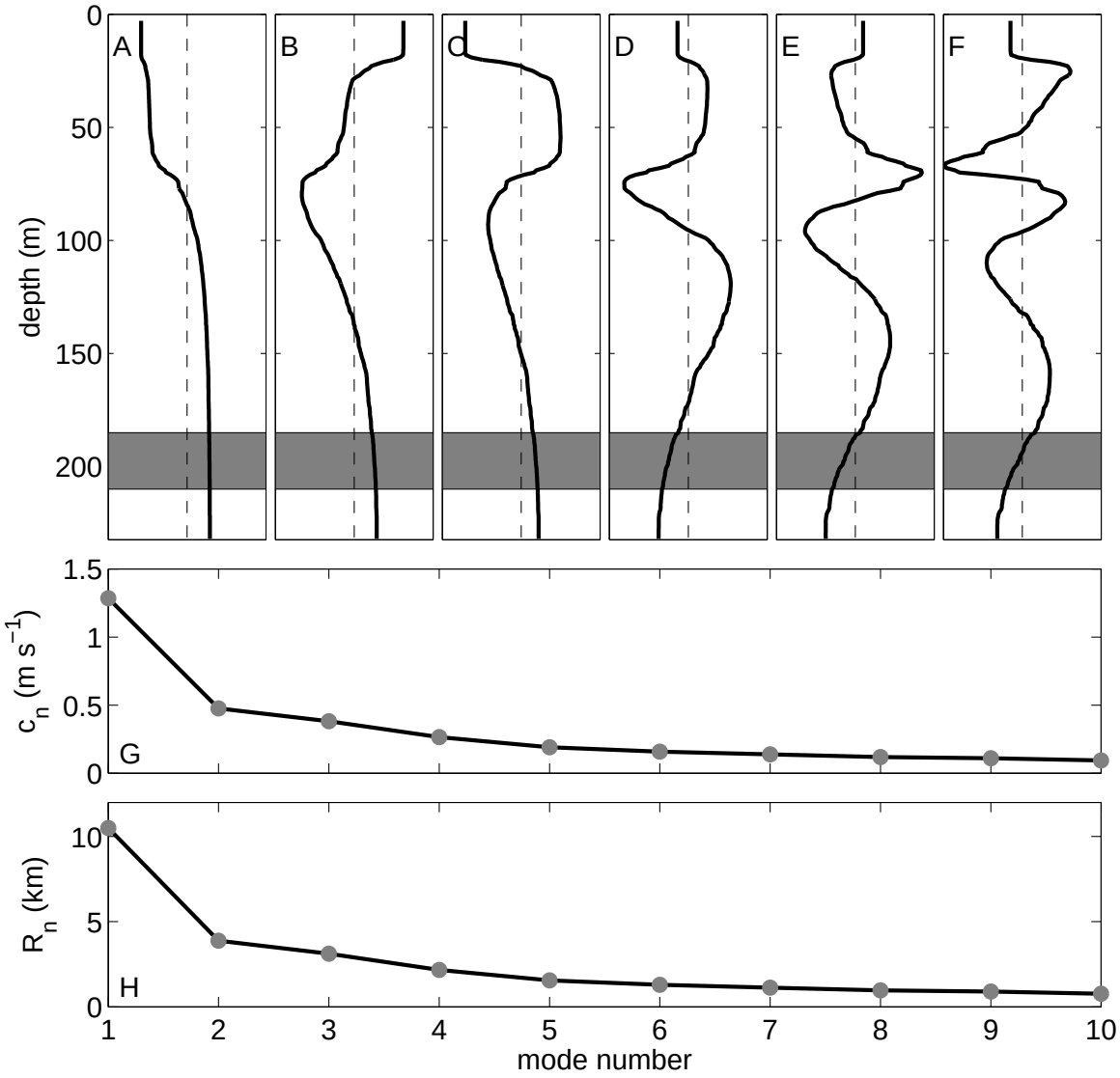

Figure 7.9.: First 6 hydrostatic internal wave modes (a-f) calculated from the stratification shown in Fig. 4.3. Shaded in grey the location of the C1 ADCP velocity measurements. Horizontal phase speeds c_n (g) in m s^{-1} and the Rossby radii $R_n = c_m/f$ for the first 10 modes (h). The modes are normalised such that $\int_{-H}^{0} \Psi_n^2 \mathrm{d}z = H$.

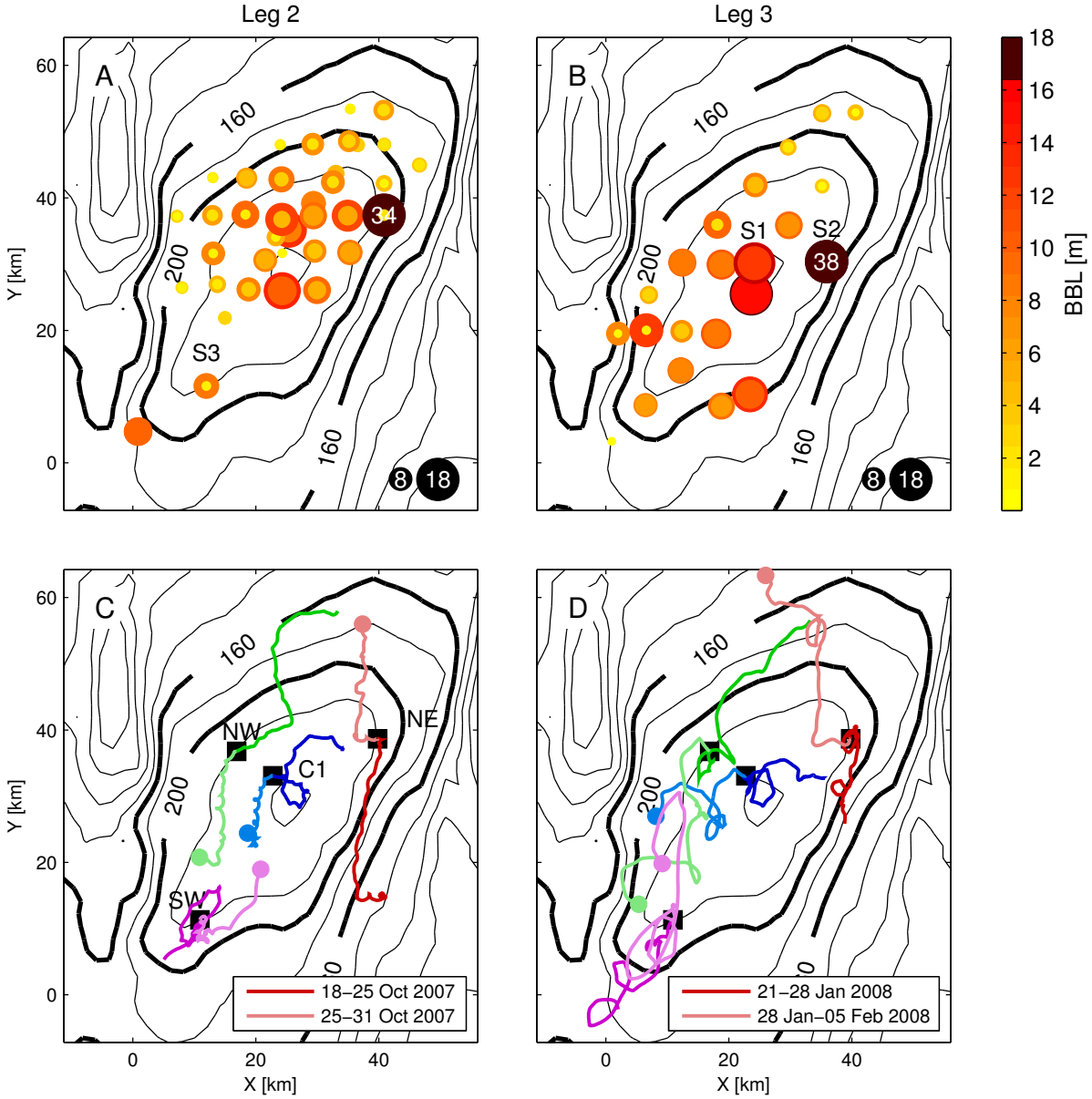

Figure 7.10.: Bottom boundary layer heights from MSS measurements for (a) Leg 2 and (b) Leg 3. Each circle represents a station with 4-5 casts taken within 1 hour. Inner and outer circles indicate minimum and maximum BBL heights among these casts. BBL heights are colour-coded and, for better visibility, proportional to the circle diameters (legend in the lower right, out-of-range values indicated as numbers). Panels (c) and (d) show pseudo-trajectories from the lowest current records at the mooring positions (dots indicate the end of the trajectories). Trajectories 7 days before and during the surveys are displayed in full and light colour shading, respectively.

7.2.2. Mixing processes

To identify differences in mixing processes in the flat and sloping parts of the basin, we analyse turbulence measurements from a number of selected stations that are representative for the different locations.

Basin centre

We start our investigations using data from station S1 (sampled during Leg 3), which is located in the relatively flat part of the basin near the deepest point (Fig. 7.10b). Comparison with other stations in the vicinity of S1 has shown that this station is representative for the entire region. The pseudo-trajectories from the lowest ADCP bin (15 m above the bottom) at the nearby mooring position C1 (Fig. 7.10d) suggest that the near-bottom currents in the central part of the basin before and during the survey are governed by a steady mean current towards the east with a superimposed counter-clockwise rotating contribution from sub-inertial motions that have been identified as topographic waves above. In contrast to Leg 2 (Fig. 7.10c), no signal of near-inertial waves can be identified during this period.

The impact of these near-bottom currents on BBL stratification and mixing parameters is illustrated in Fig. 7.11. Strongly enhanced near-bottom dissipation rates (Fig. 7.11d) have eroded a well-mixed boundary layer with a thickness of the order of 10 m (Fig. 7.11a). This entrainment process has created a sharp density interface that shows some variability in height above the bottom during the time of our measurements (40 minutes), presumably due to the effect of internal waves travelling along the interface. Averaging observed stratification and dissipation rates in a coordinate system referenced with respect to this interface removes this effect, illustrating the structure of the interface region more clearly (Fig. 7.11c). From $\varepsilon \approx 7 \times 10^{-9}$ W kg^{-1} and $N^2 \approx 2 \times 10^{-4}$ s^{-2} observed in the centre of the interface, we compute a vertical diffusivity of $\kappa_\rho = \gamma\varepsilon/N^2 \approx 7 \times 10^{-6}$ m^2 s^{-1}, assuming the canonical value $\gamma = 0.2$ for the mixing efficiency (*Osborn*, 1980). With this diffusivity, the time scale for the destruction of an interface of 2-3 m thickness (Fig. 7.11c) by mixing is of the order of 10 days. In view of the strong intermittency of the near-bottom currents on time scales of weeks (Fig. 7.5), this suggests a picture in which the BBL in the centre of the basin is created by a balance between generation by entrainment and destruction by turbulent diffusion. The slow times scales of entrainment and turbulent diffusion in the interface region are also mirrored in the tracer profile shown in Fig. 7.11b (tracer measurements are discussed in detail in Chap. 6). Consistent with the homogeneous density and high dissipation rates in the BBL, also the tracer is seen to be well-mixed. However, tracer concentrations inside the BBL are smaller by at least a factor of two compared to concentrations inside and just above the interface. This points to a weak exchange between the BBL and the interior in this part of the basin, which is consistent with the minimum in the basin-scale diffusivities found just above the interface level (see Chap. 6).

Boundary-layer destabilisation

An interesting phenomenon visible in Fig. 7.10a,b are the very thick BBLs (34 and 38 m, respectively) on the eastern slope of the basin. We investigated the structure of the BBL in this region, taking station S2 (Leg 3) as an example, to find a possible explanation for the extreme BBL heights. 4 consecutive MSS casts taken at S2 illustrate the presence of a perfectly well-mixed BBL below a region with nearly linear stratification (Fig. 7.12a). A more detailed view of the density structure inside the BBL (Fig. 7.12b-e) reveals extremely small density differences (1-2$\times 10^{-3}$ kg m^{-3}), and, most importantly, the presence of marginally unstable stratification. The corresponding dissipation rates in the bulk of the BBL are at least an order of magnitude

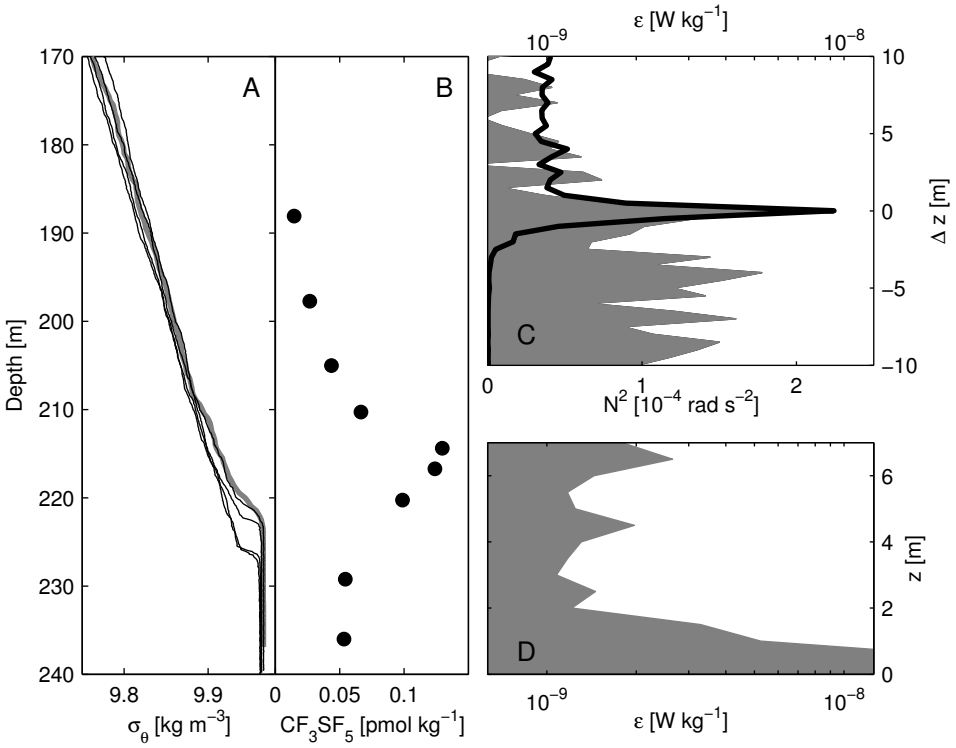

Figure 7.11.: Profiles of (a) potential density from 4 MSS casts (thin), and 1 CTD cast (thick grey); (b) tracer concentration; (c) stratification (black) and dissipation rates vertically referenced with respect to the stratification peak, and (d) dissipation rates vertically referenced with respect to the bottom. All profiles taken on 04 February 2008 (12:30-13:10 UTC) at station S1 (see Fig. 7.10b). Data in (c) and (d) are averages over 4 microstructure profiles. Note that $\Delta z = -10$ m in (c) does not coincide with the bottom.

larger than those observed at S1, and show a vertical structure that is not consistent with the expected z^{-1} decay for wall-bounded shear flows ("law of the wall").

A hint towards a possible mechanism for the destabilisation of the BBL comes from the trajectory of the nearby current meter at position NE. Fig. 7.10d illustrates that currents on the eastern flank of the basin are dominated by the persistent northward flow associated with the deep rim current with some super-imposed sub-inertial motions (the near-inertial signal is too weak to be visible in this plot). Northward flow, however, implies a downslope Ekman transport in the BBL, and therefore a downslope advection of less dense water from positions higher up the slope. The differential advection of less dense water inside the BBL underneath denser water has a tendency to destabilise the BBL, which may ultimately lead to unstable stratification and convection (*Weatherly and Martin*, 1978; *Garrett et al.*, 1993). Observations of this phenomenon on the Oregon continental shelf (USA) have been described by *Moum et al.* (2004), who report a similar vertical structure of dissipation rate profiles. In the absence of any other plausible mechanism for the destabilisation of the BBL over tens of meters and over time scales of one hour (and possibly longer), we believe that the advective effect of the downslope Ekman transport is responsible for the observed BBL convection also in the Gotland Basin. The large lateral pressure gradients built up in the presence of a nearly 40 m thick well-mixed water column adjacent to the strong stratified interior suggests a strong tendency for BBL restratification. This process promotes the exchange between well-mixed BBL fluid and the

interior via intrusions (and thus basin-scale mixing); however, it also suggests that BBLs of this size are not likely to be a permanent feature.

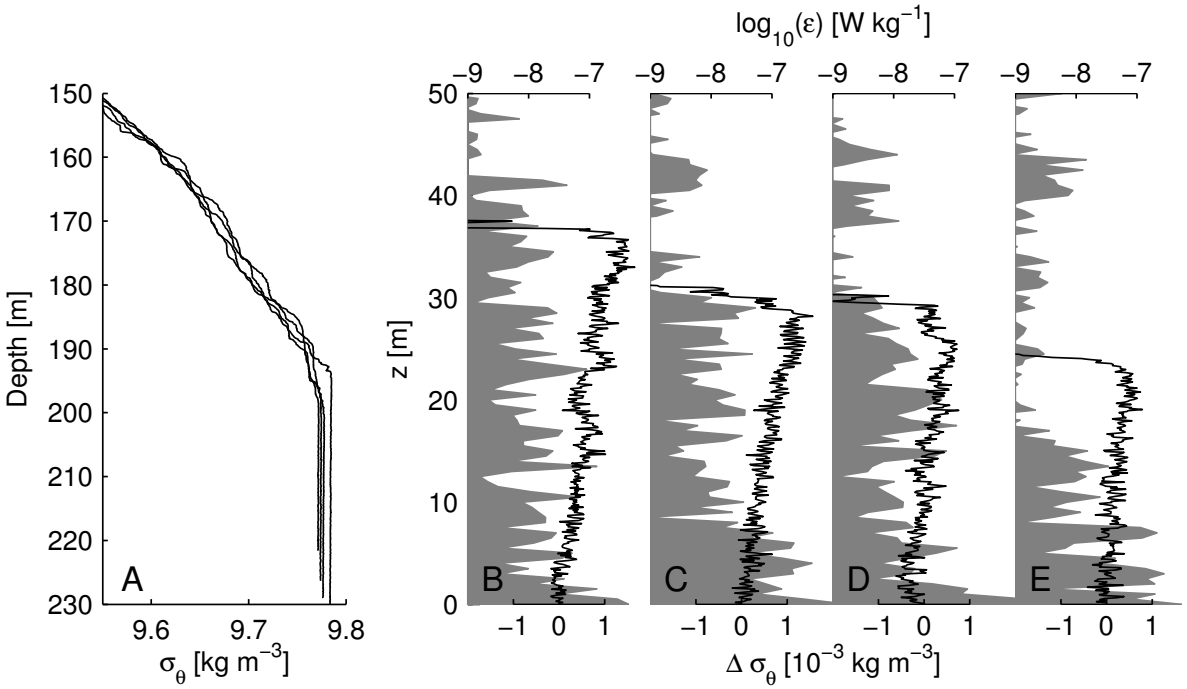

Figure 7.12.: (a) Potential density from 4 MSS casts (04 February 2007, 15:30-16:10 UTC) at station S2 (Leg 3). Panels (b-e) show the corresponding dissipation rates (areas) and density differences (lines,with respect to the density at the bottom) in bottom-referenced coordinates.

Boundary-layer mixing on sloping topography

The convection-driven mixing described above is a particular phenomenon only observed at a special location. A situation much more typical for the lateral slopes of the basin has been investigated at station S3 (Leg 2), located on the southern slope of the basin as indicated in Fig. 7.10. At this position, we performed a longer (compared to the other stations) time series of microstructure measurements (36 profiles over 8 hours) in order to investigate the temporal variability of the BBL on the slopes of the basin in more detail. Fig. 7.13a shows that the BBL at this location is much thinner compared to the central parts of the basin (Fig. 7.10a,b, Fig. 7.11), and exhibits a much larger variability. With thicknesses varying between approximately 1 and 10 m. Moreover, in contrast to the stable, nearly linear density gradients observed in the central stations above the BBL (Figs. 7.11, 7.12), at station S3 the overlying stratification is highly variable. Since the rim current is rather weak at this location (Fig. 7.10c), it is likely that this variability is caused by advection due to sub-inertial motions, and by the processes associated with restratification (intrusions, internal waves). It is worth noting that in their study of boundary-layer mixing, *Gloor et al.* (2000) found similar qualitative differences between stable, thick BBLs in the central part of a small lake, and thin, variable BBLs on the slopes.

An important difference in mixing between slope and central stations is revealed in Fig. 7.13b, comparing the time-averaged dissipation rates at S3 with those from the central part of the basin

(defined here as the region inside the 220 m isobath). For the interpretation of this figure, it is important to note that the averaged dissipation rate found for the central part ($\varepsilon \approx 10^{-9}$ W kg^{-1}) only mirrors the noise level of the profiler rather than the physical dissipation process. This is easily understood from the fact that the interior diffusivity, found from the initial tracer spreading rates after the injection, was around $\kappa_\rho = 1 \times 10^{-6}$ m^2 s^{-1}. Assuming a mixing efficiency of $\gamma = 0.2$ as above, we find that the averaged dissipation rate in the interior is $\varepsilon = \kappa_\rho N^2/\gamma \approx 2.5 \times 10^{-10}$ W kg^{-1}, four times smaller than the noise level. Keeping this number in mind, the data shown in Fig. 7.13b suggest that, on the slope, dissipation rates *above* the BBL are about one order of magnitude larger than the corresponding values observed at the same level in the centre. Since the region above the BBL is strongly stratified, there is no reason to believe that mixing is less efficient compared to the central part, and we conclude that slopes are an important region for mixing even *outside* the BBL.

The quantity $\gamma\varepsilon N^2$, which is the actual rate at which a fluid with different densities is mixed by *molecular* diffusion (assuming that production=destruction of buoyancy variance) was suggested by *Umlauf and Burchard* (2011) for the quantification of boundary mixing. It nicely shows the difference between the turbulent BBL (220 - 210 m) and the region above (210 - 200 m). The former is well-mixed and thus has lower N^2 and $\gamma\varepsilon N^2$ values than the latter which is less turbulent but more strongly stratified. Far above the BBL $\gamma\varepsilon N^2$ values of S3 and the interior become equal (Fig. 7.13c). It is worth to note that γ was always assumed to be 0.2. Since it is well known that γ can be an order of magnitude smaller in well-mixed BBLs the values in Fig. 7.13c can be considered as a maximum; emphasising the role of mixing directly above the BBL interface. A comparison of all MSS profiles, with the BBL part removed, grouped into inside versus outside the 220 m isobath showed a similar increase in the depth region between 210 - 190 m. Interestingly, the vertically resolved diffusivities derived from S,T and CF_3SF_5 profiles also show an increase in this region (Chap. 6) and let us speculate that the increased $\gamma\varepsilon N^2$ at the slopes might be the reason for increased basin scale diffusivities in these depths. Similar results have been found from the MSS profiles of Leg 3 but, due to the overall lower profile number, the average profile is noisier.

7.3. Conclusions

Gustafsson and Stigebrandt (2007) as well as *Schneider et al.* (2010) showed that, during anoxic conditions, the Gotland Basin becomes a source of phosphate, which leads to lower nitrogen-to-phosphate ratios than demanded by phytoplankton (*Nausch et al.*, 2008b). This favours nitrogen-fixating cyanobacteria growth and can cause massive spring blooms (*Wasmund et al.*, 2001). This example shall emphasise (i) that numerous chemical and biological processes are directly coupled to turbulent fluxes and (ii) the importance of understanding vertical fluxes of tracers as good as possible.

In this work we could refine the seasonal dependency of the basin scale mixing rates (*Axell*, 1998) to a coupling between single wind events and the subsequent increase of mixing. One key result of our investigations is the role of the sub-inertial motions, having at least a similar importance as the internal wave induced mixing. The basin rim current was found to have a more local (at the eastern flank) contribution to mixing. The measured energy dissipation rates showed values of 1×10^{-9} W kg^{-1}, the noise level of the profiler, in the interior of the basin. Most of the dissipation occurred in the flat central part of the basin, but, due to the stable and well mixed BBL in that area, with a rather low mixing efficiency. In contrast to that, the dissipation rates measured at the basin slopes, were lower, but also occurred outside the BBL in the strongly stratified interior region, leading to a much larger mixing efficiency of $\gamma = 0.2$. The

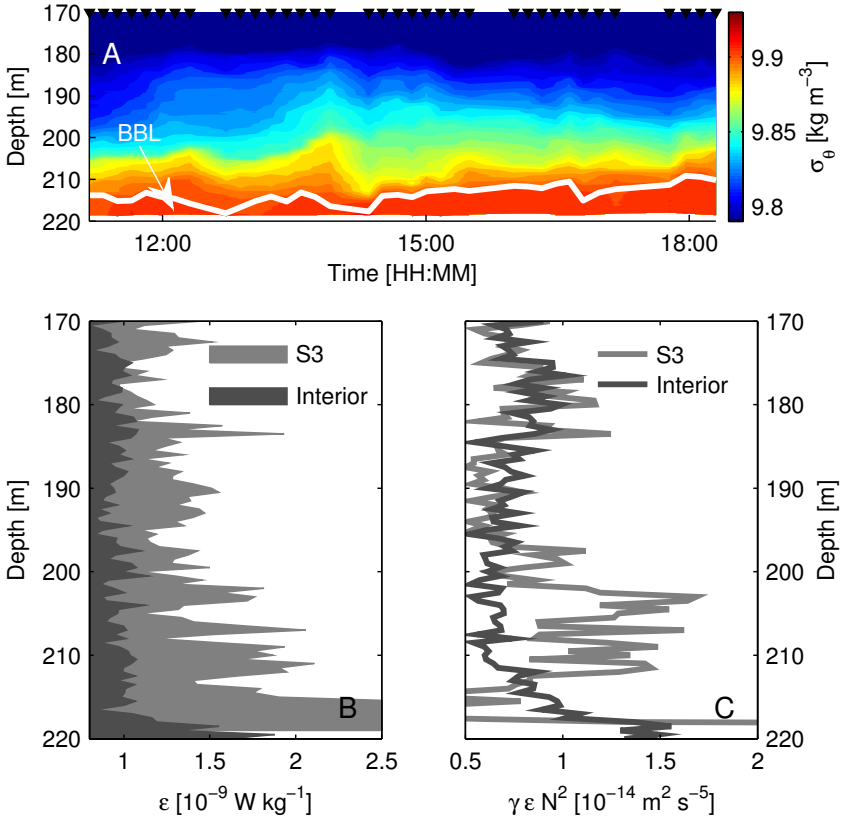

Figure 7.13: (a) Time series of potential density from 36 MSS casts (timing indicated by black triangles) at station S3 (Leg 2) on 31 October 2007; (b) comparison of averaged dissipation rates at S3 and in the interior region (defined here as the region inside the 220 m isobath); (c) same as panel (b) but now for the production(=destruction) of buoyancy variance.

mixing occurring in the stratified region might be generated, similar to the ocean, by internal waves and intrusions formed during the restratification process at the BBL. A more detailed investigation of this highly efficient mixing process is deserved. Both results, the importance of BBL and near-slope mixing, as well as the quiescence in the interior is backed up by the results of Chap. 6, where interior mixing rates are about ten times smaller than the basin scale mixing rates.

8. Summary and Conclusions of the BaTRE project

The Baltic Sea Tracer Release Experiment was designed to inject the tracer CF_3SF_5 into the deeper Gotland Basin in order to measure its dispersion and the mixing processes in the Gotland Basin. Useful additional information was to gain knowledge about the behaviour of CF_3SF_5 in anoxic conditions (e.g. particle adsorption) which has not been shown before (*Ho et al.*, 2008). The tracer CF_3SF_5 proved to be an inert tracer under anoxic conditions and the subsequent spreading has been successfully measured. It could thus be proven that CF_3SF_5 is a useful tool to study turbulent mixing in the Baltic Sea. The timing of the injection was, by lucky coincidence, such that the tracer was injected 3–4 months after a warm, salty inflow that renewed the water of the deeper Gotland Basin and created an optimal environment to study diapycnal mixing during a Baltic Sea stagnation period. The major results of the tracer release are observing the difference between boundary and interior mixing rates and finding a dominance of boundary mixing processes for basin scale mixing rates. This result is in good agreement with the findings from lakes and ocean basins. Furthermore the tracer results revealed that the commonly-used 1-dimensional isopycnally averaged diffusion model fails, even if the hypsography is included, when the modelled compound is inhomogeneously distributed on isopycnals. This result supports the boundary mixing hypothesis and elucidates the lack of understanding of boundary–interior exchange processes in the Gotland Basin. The strong loss of tracer between Leg 2 and Leg 3 suggests that the mixing processes within the bottom boundary layer are faster than the exchange processes between the interior and the boundary layer. An examination of these timescales will be an interesting task and might help to better assess fluxes of components that are produced at the boundaries, such as e.g. CO_2 during the remineralisation of organic matter.

Looking at the mixing from the basin-scale perspective showed that the increase of mixing is directly coupled to wind events. Also in phase with the wind events is an increase of the kinetic energy in the sub-inertial and higher frequency bands, to which the sub-inertial motions contribute roughly two-thirds and the near-inertial motions the other third. The Gotland Basin shows a resonance with wind events that have periods of approx. 4 days and lead to increased basin-scale mixing rates. Microstructure measurements show, in agreement with the results from the tracer experiments, a more or less quiescent interior and increased, but highly variable, dissipation rates at the basin boundaries. This is the second major finding of the BaTRE project: The proposed shear-induced internal wave breaking in the interior plays a small role for basin mixing rates compared to the boundary processes, which are dominated by the sub-inertial motions. A further interesting result is the finding of high, and partly unstable, BBL layers at the eastern flank of the basin. From these indications it can be argued that an Ekman transport, triggered by the basin rim current, is the origin for the observed instabilities. The role of the basin rim current for mixing rates in the Gotland Basin was discussed to some extent by *Hagen and Feistel* (2007), but the suggested physical process was the vertical shear due to bottom friction, which cannot explain the observed instabilities of the BBL, see Chap. 7.2.2.

9. Outlook

Lets recall the two main questions raised in the BaTRE project:

1. How large is the diapycnal mixing?
2. Where does diapycnal mixing occur?
3. What are the processes of diapycnal mixing?

As summarised in Chap. 8 the first two questions could be answered by the tracer spreading and the additional microstructure measurements. Depending on how detailed one wants to answer the third question, it can be stated that the processes, especially the boundary processes, of mixing in the deeper Gotland Basin need further investigation and quantification of their importance. The following questions emerged through the BaTRE project, and most of them are directly related to the boundary mixing processes and the interplay between the boundary and the interior water masses:

1. What is the role of near-inertial and sub-inertial motions in boundary mixing processes?
2. What are the exchange timescales between the boundary layer and the basin interior?
3. Does the basin rim current induce an Ekman transport? Can the Ekman transport explain the observed unstable BBLs?
4. How large is the energy flux of internal waves into the Gotland Basin?

The capabilities of today's numerical models in combination with the database of the BaTRE project make it possible to set up a meso-scale (defined as a model with a horizontal grid size resolving the internal Rossby radius) model of the Gotland Basin. This model, if it can properly model the bottom boundary layers as well as the evolution of the density field and the tracer dispersion, will add information to the in situ data that are limited in space and time. If the numerical model is simply seen as a further tool used to understand the processes of mixing in the Gotland Basin, then it is now the right moment to use this tool in the attempt to answer the questions listed above.

Future tracer release experiments in the Baltic Sea and in similar anoxic conditions will benefit from the experiences made during BATRE. Since BaTRE was an experiment during a Baltic Sea stagnation period, a further tracer release experiment might address the spreading of a Baltic Sea inflow. The spreading time scales of inflows are of the order of months and have horizontal scales of several hundreds of kilometres. Furthermore they do have no contact with the atmosphere. These scales and properties make CF_3SF_5 an optimal choice for marking such an inflow. The timing and more important, the entrainment of the inflow could be measured on its way through the Baltic Sea Basins. Technical challenges are the discovery of an inflow and the timely injection of the inflow.

A. Basin-scale budget of potential energy

To recall, the buoyancy is defined as

$$b = -\frac{g}{\rho_0}(\rho - \rho_r) \,, \tag{A.1}$$

where ρ_r denotes a *constant* reference density. Note that it is posssible to work with a vertically varying reference density as well but this introduces additional terms in the analysis below.

The potential energy *per unit mass* with respect to ρ_r is then defined as

$$E_p = \frac{g(\rho - \rho_r)(z - z_r)}{\rho_0} = -b\tilde{z} \,, \tag{A.2}$$

where z_r is a constant reference level, and we introduce $\tilde{z} = z - z_r$ for convenience.

The transport equation for the buoyancy used in the following is defined as

$$\frac{\mathrm{D}b}{\mathrm{D}t} = -\frac{\partial B}{\partial z} \,, \tag{A.3}$$

where $B =< w'b' >$ denotes the turbulent buoyancy flux, see also Eq. (3.12).

The change in time of the potential energy per unit mass can be derived from Eq. (A.3) by multiplying it with $\tilde{z}$, which yields

$$\frac{\mathrm{D}E_p}{\mathrm{D}t} = -\frac{\mathrm{D}b\tilde{z}}{\mathrm{D}t} = -bw - \tilde{z}\frac{\mathrm{D}b}{\mathrm{D}t} \,, \tag{A.4}$$

where we used the fact that $\mathrm{D}\tilde{z}/\mathrm{Dt} = w$. Inserting Eq. (A.3) then results in

$$\frac{\mathrm{D}E_p}{\mathrm{D}t} = -bw - B + \frac{\partial \tilde{z}B}{\partial z} \,, \tag{A.5}$$

where the last term can be interpreted as the divergence of the turbulent flux of potential energy. Note that we assumed above that the turbulent flux is strictly vertical, an assumption that is easily relaxed if necessary.

To derive a version that can be integrated over a fixed control volume, we use the definition of the material derivative and re-write Eq. (A.5) as

$$\frac{\partial E_p}{\partial t} = -bw - B + \frac{\partial \tilde{z}B}{\partial z} + \frac{\partial u_i \tilde{z} b}{\partial x_i} \,, \tag{A.6}$$

where the last term denotes the advective flux of potential energy.

Integrating Eq. (A.6) over a *fixed* control volume, and using Gauss' theorem, yields

$$\frac{\mathrm{d}}{\mathrm{d}t}\int_V E_p \,\mathrm{d}V = -\int_V bw \,\mathrm{d}V - \int_V B \,\mathrm{d}V + \int_A \tilde{z}Bn_z \,\mathrm{d}A + \int_A \tilde{z}bu_i n_i \,\mathrm{d}A \,, \tag{A.7}$$

where the n_i denote the components of the outward normal unit vector on the bounding surface with the convention $n_3 = n_z$. More specifically, if we identify the volume, V, with the lower

part of a laterally closed basin, bounded on the top, $z = z_t$, by a horizontal surface, A_t, then Eq. (A.7) becomes

$$\frac{\mathrm{d}}{\mathrm{d}t}\int_V E_p \,\mathrm{d}V = -\int_V bw \,\mathrm{d}V - \int_V B \,\mathrm{d}V + \int_{A_t} \tilde{z} B \,\mathrm{d}A + \int_{A_t} \tilde{z} bw \,\mathrm{d}A \;, \tag{A.8}$$

since the buoyancy flux through the lower boundary is zero. Further, identifying the reference level with the upper boundary, $z_t = z_r$, Eq. (A.8) simplifies to

$$\frac{\mathrm{d}}{\mathrm{d}t}\int_V E_p \,\mathrm{d}V = -\int_V bw \,\mathrm{d}V - \int_V B \,\mathrm{d}V \;, \tag{A.9}$$

without loss of generality. If, on the long-term average, no water enters the basin, the advective contribution to Eq. (A.9) will be mostly related to long internal and topographic waves, i.e. it will only cause reversible changes to the potential energy.

A.1. Interior and boundary-layer dissipation

The turbulent buoyancy flux, B, in Eq. (A.9) is the sum of mixing in the interior and near the boundaries. Ignoring the advective term in Eq. (A.9) for the moment, we can re-write this equation as

$$\frac{\mathrm{d}}{\mathrm{d}t}\int_V E_p \,\mathrm{d}V = \int_{V_i} \gamma_i \varepsilon \,\mathrm{d}V + \int_{V_b} \gamma_b \varepsilon \,\mathrm{d}V = \gamma_b \int_{V_b} \varepsilon \,\mathrm{d}V + \gamma_i \int_{V_i} \varepsilon \,\mathrm{d}V \;, \tag{A.10}$$

where V_b and V_i denote the volumes of the bottom boundary layer and the interior, respectively, such that $V = V_b + V_i$. The mixing efficiency is defined as $\gamma = -B/\varepsilon$, with $\gamma_b = 0.01 - 0.05$ and $\gamma_i \approx 0.2$ denoting some typical values in the BBL and the interior, respectively.

Using the definition of the volume-averaged dissipation rate,

$$\langle \varepsilon \rangle_V = \frac{1}{V}\int_V \varepsilon \,\mathrm{d}V \;, \tag{A.11}$$

we find

$$\langle \varepsilon \rangle_V = \langle \varepsilon \rangle_{V_b} \frac{V_b}{V} + \langle \varepsilon \rangle_{V_i} \frac{V_i}{V} \quad . \tag{A.12}$$

Using Eq. (A.12), Eq. (A.10) can be rewritten in the form

$$\begin{aligned} \frac{\mathrm{d}}{\mathrm{d}t}\int_V E_p \,\mathrm{d}V &= \gamma_t \langle \varepsilon \rangle_V V \\ &= \gamma_i \langle \varepsilon \rangle_{V_i} V_i + \gamma_b \langle \varepsilon \rangle_{V_b} V_b \\ &= \gamma_i \langle \varepsilon \rangle_{V_i} V_i + \gamma_b \langle \varepsilon \rangle_{V_b} A_b H_b \;, \end{aligned} \tag{A.13}$$

where γ_t denotes the total effective mixing efficiency for the entire volume, H_b the thickness of the BBL, and A_b the sediment area below z_t.

If interior mixing dominates we thus have

$$\frac{\mathrm{d}}{\mathrm{d}t}\int_V E_p \,\mathrm{d}V = \gamma_t \langle \varepsilon \rangle_V V = \gamma_i \langle \varepsilon \rangle_{V_i} V_i \;, \tag{A.14}$$

and, vice-versa, if boundary-layer mixing dominates

$$\frac{\mathrm{d}}{\mathrm{d}t}\int_V E_p\,\mathrm{d}V = \gamma_t\,\langle\varepsilon\rangle_V\,V = \gamma_b\,\langle\varepsilon\rangle_{V_b}\,V_b = \gamma_b\,\langle\varepsilon\rangle_{V_b}\,A_bH_b \quad . \tag{A.15}$$

If the efficiencies γ_i and γ_b, and the left hand side of Eq. (A.14) and Eq. (A.15), respectively, are known, these equations can be used to compute average dissipation rates in the interior and the boundary layer. If, on the other hand, the dissipation rates are known, e.g. from microstructure measurements, estimates for the mixing efficiencies can be derived.

Note that often it may be required to estimate the volume integral of E_p from the assumption of lateral homogeneity,

$$\int_{z_b}^{z_t} E_p(z)A(z)\,\mathrm{d}z\ , \tag{A.16}$$

where $z = z_b$ denotes the deepest of the basin, and $A(z)$ is known from the hypsography.

A.2. Numerical Integration

Some comments regarding the numerical integration of Eq. (A.16) are appropriate here. Consider a series of CTD loggers located at z_i with $z_{i+\frac{1}{2}} = (z_{i+1} + z_i)/2$ located in the middle between two loggers, and $\Delta_i = z_{i+\frac{1}{2}} - z_{i-\frac{1}{2}}$ denoting the thickness of the integration cell. A_i and $A_{i+\frac{1}{2}}$, respectively, denote the values of hypsographic areas at these locations, and b_i the buoyancy computed from the CTD logger at z_i. The contribution of one such interval to the integral in Eq. (A.16) is thus

$$-\int_{z_{i-\frac{1}{2}}}^{z_{i+\frac{1}{2}}} b(z)A(z)z\,\mathrm{d}z\ , \tag{A.17}$$

with an appropriate reference level chosen for z.

The simplest discretization of Eq. (A.17) assumes that both b and A are constant over each integration cell, which yields

$$\begin{aligned} -b_iA_i\int_{z_{i-\frac{1}{2}}}^{z_{i+\frac{1}{2}}} z\,\mathrm{d}z &= -\frac{1}{2}b_iA_i(z^2_{i+\frac{1}{2}} - z^2_{i-\frac{1}{2}}) \\ &= -\frac{1}{2}b_iA_i(z_{i+\frac{1}{2}} + z_{i-\frac{1}{2}})(z_{i+\frac{1}{2}} - z_{i-\frac{1}{2}}) \\ &= -\frac{1}{2}b_iA_i(z_{i+\frac{1}{2}} + z_{i-\frac{1}{2}})\Delta_i \quad . \end{aligned} \tag{A.18}$$

Because of the lack of supplementary data, there is clearly no alternative to assuming a constant b across the integration cell — but for the area, $A(z)$, there is. The area may vary substantially across the integration cell, and on the next level of complexity this should be taken into account. To this end, using integration by parts, we rewrite Eq. (A.17) as

$$-b_i\int_{z_{i-\frac{1}{2}}}^{z_{i+\frac{1}{2}}} A(z)z\,\mathrm{d}z = -b_i\,\frac{z^2}{2}A(z)\Big|_{z_{i-\frac{1}{2}}}^{z_{i+\frac{1}{2}}} + b_iA'_i\int_{z_{i-\frac{1}{2}}}^{z_{i+\frac{1}{2}}}\frac{z^2}{2}\,\mathrm{d}z\ , \tag{A.19}$$

where $A'_i = (A_{i+\frac{1}{2}} - A_{i-\frac{1}{2}})/\Delta_i$ denotes the slope of A. Integrating the second part, and inserting

the integration limits, this yields

$$-b_i \int_{z_{i-\frac{1}{2}}}^{z_{i+\frac{1}{2}}} A(z) z \, \mathrm{d}z = -\frac{1}{2} b_i (z_{i+\frac{1}{2}}^2 A_{i+\frac{1}{2}} - z_{i-\frac{1}{2}}^2 A_{i-\frac{1}{2}}) + \frac{1}{6} b_i A_i' (z_{i+\frac{1}{2}}^3 - z_{i-\frac{1}{2}}^3) \,, \tag{A.20}$$

which is seen to reduce to Eq. (A.18) for constant A inside the integration volume.

B. Scales in the Gotland Basin

As a reference for the order of magnitude of several, in ocean turbulence commonly used scales, the following length scales are calculated for typical stratifications and dissipations in the deeper Gotland Basin during the BaTRE project.

Corrsin scale Above which eddies are deformed by shear:

$$L_C = \sqrt{\varepsilon/S^3}\,. \tag{B.1}$$

Ozmidov scale Above which eddies are deformed by stratification:

$$L_O = \sqrt{\varepsilon/N^3}\,. \tag{B.2}$$

Kolmogorov scale Smallest scale of eddies:

$$L_K = \left(\nu^3/\varepsilon\right)^{\frac{1}{4}}\,. \tag{B.3}$$

The approximate largest scales of the dissipative subrange are $\approx 10 L_K$.

Batchelor scale Scale at which temperature/salinity variance is decreased by diffusion:

$$L_{B(T)} = \left(\kappa_m(T)\nu/\varepsilon\right)^{\frac{1}{4}}\,, \tag{B.4}$$

$$L_{B(S)} = \left(\kappa_m(S)\nu/\varepsilon\right)^{\frac{1}{4}}\,. \tag{B.5}$$

ε [W kg^{-1}]	L_K [cm]	L_O [cm]	L_C [cm]	$L_{B(T)}$ [cm]	$L_{B(S)}$ [cm]
5×10^{-10}	5.5	34	15	1.7	0.17
1×10^{-9}	4.7	49	21	1.5	0.15
5×10^{-9}	3.1	109	47	1.0	0.1
1×10^{-8}	2.6	155	67	0.8	0.08
5×10^{-8}	1.8	346	150	0.6	0.05

Table B.1.: Turbulent scales in the interior Gotland Basin for a typical stratification of $N^2 = 3 \times 10^{-5}$ s^{-2} or $N^{-1} = 1150$ s. Shear S is mean shear taken from the internal-wave-induced horizontal shear of the 2 m ADCP bins at the C1 mooring, Fig. 7.7b.

Bibliography

Appt, J., J. Imberger, and H. Kobus (2004), Basin-scale motion in stratified Upper Lake Constance, *Limnol. Oceanogr.*, *49*(4), 919–933, doi: 10.4319/lo.2004.49.4.0919.

Armi, L. (1978), Some evidence for boundary mixing in the deep ocean, *J. Geophys. Res.*, *83*(C4), 1971–1979, doi: 10.1029/JC083iC04p01971.

Astok, V. K., and R. V. Ozmidov (1972), Statistische Charakteristiken der Pulsationen eines Tracers aus momentanen Punktquellen (nach Versuchen in der Ostsee), *Beitr. Meereskd.*, *30–31*, 27–34.

Axell, L. B. (1998), On the variability of Baltic Sea deepwater mixing, *J. Geophys. Res.*, *103*(C10), 21667–21682, doi: 10.1029/98JC01714.

Axell, L. B. (2002), Wind-driven internal waves and Langmuir circulations in a numerical ocean model of the southern Baltic Sea, *J. Geophys. Res.*, *107*(C11), 3204, doi: 10.1029/2001JC000922.

Barber, C. B., D. P. Dobkin, and H. T. Huhdanpaa (1996), The Quickhull algorithm for convex hulls, *ACM T. Math. Software*, *22*(4), 469–483, doi: 10.1145/235815.235821.

Becherer, J., and L. Umlauf (2011), Boundary mixing in lakes. 1. Modeling the effect of shear-induced convection, *J. Geophys. Res.*, *116*, C10017, doi: 10.1029/2011JC007119.

Brosin, H. J. (1972), Untersuchungen zur horizontalen turbulenten Diffusion in den Gewässern um Rügen, *Beitr. Meereskd.*, *30–31*, 35–40.

Brosin, H. J. (1974), Untersuchungen zur mittelmasstäblichen horizontalen Diffusion mit Driftbojen in den Gewässern um Rügen, *Beitr. Meereskd.*, *34*, 5–8.

Brosin, H. J., A. N. Gezencvej, G. S. Karabašev, U. Kremser, L. K. Toai, S. S. Murav'ev, R. V. Ozmidov, and K. Viogt (1972), Das mittlere dreidimensionale Bild der Diffusion von Beimengungen aus momentanen Punktquellen im Meer, *Beitr. Meereskd.*, *30–31*, 41–53.

Bullister, J. L., and R. F. Weiss (1983), Anthropogenic Chlorofluoromethanes in the Greenland and Norwegian Seas, *Science*, *221*(4607), 265–268, doi: 10.1126/science.221.4607.265.

Bullister, J. L., and R. F. Weiss (1988), Determination of CCl_3F and CCl_2F_2 in seawater and air, *Deep-Sea Res. A*, *35*(5), 839–853, doi: 10.1016/0198-0149(88)90033-7.

Bullister, J. L., D. P. Wisegarver, and R. E. Sonnerup (2006), Sulfur hexafluoride as a transient tracer in the North Pacific Ocean, *Geophys. Res. Lett.*, *33*(18), L18603, doi: 10.1029/2006GL026514.

Burchard, H., F. Janssen, K. Bolding, L. Umlauf, and H. Rennau (2009), Model simulations of dense bottom currents in the Western Baltic Sea, *Cont. Shelf Res.*, *29*(1), 205–220, doi: 10.1016/j.csr.2007.09.010.

Burgess, A. B., R. G. Grainger, A. Dudhia, V. H. Payne, and V. L. Jay (2004), MIPAS measurement of sulphur hexafluoride (SF_6), *Geophys. Res. Lett.*, *31*(5), L05112, doi: 10.1029/2003GL019143.

Byrd, R. H., P. Lu, and J. Nocedal (1995), A Limited Memory Algorithm for Bound Constrained Optimization, *SIAM J. Sci. Stat. Comp.*, *16*(5), 1190–1208, doi: 10.1137/0916069.

Denman, K. L., and A. E. Gargett (1988), Multiple thermoclines are barriers to vertical exchange in the subarctic Pacific during SUPER, May 1984, *J. Mar. Res.*, *46*(1), 77–103, doi: 10.1357/002224088785113739.

Duda, T. F., and L. Rainville (2008), Diurnal and semidiurnal internal tide energy flux at a continental slope in the South China Sea, *J. Geophys. Res.*, *113*, C03025, doi: 10.1029/2007JC004418.

Feistel, R., G. Nausch, and E. Hagen (2003a), The Baltic inflow of autumn 2001, *Marine Science Reports*, *54*, 55–68.

Feistel, R., G. Nausch, V. Mohrholz, E. Lysiak-Pastuszak, T. Seifert, W. Matthäus, S. Krüger, and I. S. Hansen (2003b), Warm waters of summer 2002 in the deep Baltic Proper, *Oceanologia*, *45*(4), 571–592.

Feistel, R., G. Nausch, and E. Hagen (2006), Unusual Baltic inflow activity in 2002-2003 and varying deep-water properties, *Oceanologia*, *48*(S), 21–35.

Feistel, R., G. Nausch, and N. Wasmund (Eds.) (2008), *State and Evolution of the Baltic Sea, 1952-2005. A detailed 50-year survey of meteorology and climate, physics, chemistry, biology, and marine environment*, 703 pp., Wiley-Interscience, Hoboken, NJ, USA.

Fennel, W. (1989), Inertial waves and inertial oscillations in channels, *Cont. Shelf Res.*, *9*(5), 403–426, doi: 10.1016/0278-4343(89)90007-1.

Fennel, W., and H. U. Lass (1982), Phytoplankton patchiness and advection diffusion models, *Beitr. Meereskd.*, *47*, 95–103.

Gargett, A. E., T. R. Osborn, and P. W. Nasmyth (1984), Local isotropy and the decay of turbulence in a stratified fluid, *J. Fluid Mech.*, *144*, 231–280, doi: 10.1017/S0022112084001592.

Garrett, C., P. MacCready, and P. Rhines (1993), Boundary mixing and arrested Ekman layers: Rotating stratified flow near a sloping bottom, *Annu. Rev. Fluid Mech.*, *25*, 291–323, doi: 10.1146/annurev.fl.25.010193.001451.

Gill, A. E. (1982), *Atmosphere-Ocean Dynamics*, 677 pp., Academic Press, New York, NY, USA.

Gloor, M., A. Wüest, and D. M. Imboden (2000), Dynamics of mixed bottom layers and its implications for diapycnal transport in a stratified, natural water basin, *J. Geophys. Res.*, *105*(C4), 8629–8646, doi: 10.1029/1999JC900303.

Goodman, L., E. R. Levine, and R. G. Lueck (2006), On measuring the terms of the turbulent kinetic energy budget from an AUV, *J. Atmos. Ocean. Tech.*, *23*(7), 977–990, doi: 10.1175/JTECH1889.1.

Görtler, H. (1943), Über eine Schwingungserscheinung in Flüssigkeiten mit stabiler Dichteschichtung, *ZAMM-Z. Angew. Math. Me.*, *23*(2), 65–71, doi: 10.1002/zamm.19430230202.

Goudsmit, G.-H., F. Peeters, M. Gloor, and A. Wüest (1997), Boundary versus internal diapycnal mixing in stratified natural waters, *J. Geophys. Res.*, *102*(C13), 27903–27914, doi: 10.1029/97JC01861.

Gustafsson, B. G., and A. Stigebrandt (2007), Dynamics of nutrients and oxygen/hydrogen sulfide in the Baltic Sea deep water, *J. Geophys. Res. – Biogeosciences*, *112*, G02023, doi: 10.1029/2006JG000304.

Hagen, E., and R. Feistel (2001), Spreading of Baltic deep water: A case study for the winter 1997-1998, *Marine Science Reports*, *45*, 99–133.

Hagen, E., and R. Feistel (2004), Observations of low-frequency current fluctuations in deep water of the Eastern Gotland Basin/Baltic Sea, *J. Geophys. Res.*, *109*, C03044, doi: 10.1029/2003JC002017.

Hagen, E., and R. Feistel (2007), Synoptic changes in the deep rim current during stagnant hydrographic conditions in the Eastern Gotland Basin, Baltic Sea, *Oceanologia*, *49*(2), 185–208.

Hagen, E., and G. Plüschke (2009), Daily current series from the deep Eastern Gotland Basin (1993-2008), *Marine Science Reports*, *75*, 1–74.

Hickey, B. M. (1991), Variability in two deep coastal basins (Santa Monica and San Pedro) off southern California, *J. Geophys. Res.*, *96*(C9), 16689–16708, doi: 10.1029/91JC01375.

Ho, D. T., J. R. Ledwell, and W. M. Smethie (2008), Use of SF_5CF_3 for ocean tracer release experiments, *Geophys. Res. Lett.*, *35*, L04602, doi: 10.1029/2007GL032799.

Holloway, P. E. (1996), A Numerical Model of Internal Tides with Application to the Australian North West Shelf, *J. Phys. Oceanogr.*, *26*(1), 21–37, doi: 10.1175/1520-0485(1996)026<0021:ANMOIT>2.0.CO;2.

Holtermann, P., and L. Umlauf (2011), The Baltic Sea Tracer Release Experiment. Part II. Mixing processes, *J. Geophys. Res.*, submitted.

Holtermann, P., L. Umlauf, T. Tanhua, O. Schmale, G. Rehder, and J. Waniek (2011), The Baltic Sea Tracer Release Experiment. Part I. Mixing rates, *J. Geophys. Res.*, accepted.

Hughes, G. O., A. M. Hogg, and R. W. Griffiths (2009), Available potential energy and irreversible mixing in the meriodional overturning circulation, *J. Phys. Oceanogr.*, *39*(12), 3130–3146, doi: 10.1175/2009JPO4162.1.

Kaihatu, J. M. (1998), Empirical Orthogonal Function analysis of ocean surface currents using complex and real-vector methods, *J. Atmos. Ocean. Tech.*, *15*(4), 927–941, doi: 10.1175/1520-0426(1998)015<0927:EOFAOO>2.0.CO;2.

Ko, M. K. W., N. D. Sze, W. C. Wang, G. Shia, A. Goldman, F. J. Murcray, D. G. Murcray, and C. P. Rinsland (1993), Atmospheric Sulfur-Hexafluoride – Sources, Sinks and Greenhouse Warming, *J. Geophys. Res. – Atmospheres*, *98*(D6), 10499–10507, doi: 10.1029/93JD00228.

Kouts, T., and A. Omstedt (1993), Deep water exchange in the Baltic Proper, *Tellus A*, *45*(4), 311–324, doi: 10.1034/j.1600-0870.1993.t01-1-00006.x.

Krysell, M. (1992), Carbon-tetrachloride and methyl chloroform as tracers of deep-water formation in the Weddell Sea, Antarctica, *Mar. Chem.*, *39*(4), 297–310, doi: 10.1016/0304-4203(92)90015-3.

Kullenberg, G. E. B. (1972), Apparent horizontal diffusion in stratified vertical shear flow, *Tellus*, *24*(1), 17–28, doi: 10.1111/j.2153-3490.1972.tb01529.x.

Kullenberg, G. E. B. (1977), Observations of the mixing in the Baltic thermo- and halocline layers, *Tellus*, *29*(6), 572–587, doi: 10.1111/j.2153-3490.1977.tb00769.x.

Kundu, P. K., and J. S. Allen (1976), Some three-dimensional characteristics of low-frequency current fluctuations near the Oregon coast, *J. Phys. Oceanogr.*, *6*(2), 181–199, doi: 10.1175/1520-0485(1976)006<0181:STDCOL>2.0.CO;2.

Kundu, P. K., and I. M. Cohen (2008), *Fluid Mechanics*, 4$^{\text{th}}$ ed., 872 pp., Academic Press, London, UK.

Kundu, P. K., S.-Y. Chao, and J. P. McCreary (1983), Transient coastal currents and inertio-gravity waves, *Deep-Sea Res. A*, *30*(10), 1059–1082, doi: 10.1016/0198-0149(83)90061-4.

Kunze, E., L. K. Rosenfeld, G. S. Carter, and M. C. Gregg (2002), Internal Waves in Monterey Submarine Canyon, *J. Phys. Oceanogr.*, *32*(6), 1890–1913, doi: 10.1175/1520-0485(2002)032<1890:IWIMSC>2.0.CO;2.

Kunze, E., E. Riring, J. M. Hummon, T. K. Chereskin, and A. M. Thurnherr (2006), Global abyssal mixing inferred from lowered ADCP shear and CTD strain profiles, *J. Phys. Oceanogr.*, *36*(8), 1553–1576, doi: 10.1175/JPO2926.1.

Lass, H.-U., H. Prandke, and B. Liljebladh (2003), Dissipation in the Baltic Proper during winter stratification, *J. Geophys. Res.*, *108*(C6), 3187, doi:10.1029/2002JC001401.

Lass, H. U., V. Morhholz, and T. Seifert (2005), On pathways and residence time of salt-water plumes in the Arkona Sea, *J. Geophys. Res.*, *110*, C11019, doi:10.1029/2004JC002848.

Lass, H.-U., V. Mohrholz, M. Knoll, and H. Prandke (2008), Enhanced mixing downstream of a pile in an estuarine flow, *J. Mar. Sys.*, *74*(1–2), 505–527, doi: 10.1016/j.jmarsys.2008.04.003.

Law, C. S., and A. J. Watson (2001), Determination of Persian Gulf Water Transport and oxygen utilisation rates using SF_6 as a novel transient tracer, *Geophys. Res. Lett.*, *28*(5), 815–818, doi: 10.1029/1999GL011317.

LeBlond, P. H., and L. A. Mysak (1978), *Waves in the ocean*, 616 pp., Elsevier, Amsterdam, NL.

Ledwell, J. R., and A. Bratkovich (1995), A tracer study of mixing in the Santa Cruz Basin, *J. Geophys. Res.*, *100*(C10), 20681–20704, doi: 10.1029/95JC02164.

Ledwell, J. R., and T. F. Duda (2004), Mixing in a coastal environment: 1. A view from dye dispersion, *J. Geophys. Res.*, *109*, C10013, doi: 10.1029/2003JC002194.

Ledwell, J. R., and B. M. Hickey (1995), Evidence for enhanced boundary mixing in the Santa Monica Basin, *J. Geophys. Res.*, *100*(C10), 20665–20679, doi: 10.1029/94JC01182.

Ledwell, J. R., and A. J. Watson (1991), The Santa Monica Basin Tracer Experiment: A Study of Diapycnal and Isopycnal Mixing, *J. Geophys. Res.*, *95*(C5), 8695–8718, doi: 10.1029/91JC00102.

Ledwell, J. R., A. J. Watson, and C. S. Law (1998), Mixing of a tracer in the pycnocline, *J. Geophys. Res.*, *103(C10)*, 21499–21529, doi: doi:10.1029/98JC01738.

Ledwell, J. R., E. T. Montgomery, K. L. Polzin, L. C. St. Laurent, R. W. Schmitt, and J. M. Toole (2000), Evidence for enhanced mixing over rough topography in the abyssal ocean, *Nature*, *403*(6766), 179–182, doi: 10.1038/35003164.

Ledwell, J. R., L. C. St. Laurent, J. B. Girton, and J. M. Toole (2011), Diapycnal Mixing in the Antarctic Circumpolar Current, *J. Phys. Oceanogr.*, *41*(1), 241–246, doi: 10.1175/2010JPO4557.1.

Lorrai, C., L. Umlauf, J. Becherer, A. Lorke, and A. Wüest (2011), Boundary mixing in lakes. 2. Combined effects of shear-induced and convective turbulence on basin-scale mixing, *J. Geophys. Res.*, *116*, C10018, doi: 10.1029/2011JC007121.

Lueck, R. G., F. Wolk, and H. Yamazaki (2002), Oceanic velocity microstructure measurements in the 20th century, *J. Oceanogr.*, *58*(1), 153–174, doi: 10.1023/A:1015837020019.

Maas, L. R. M., and F.-P. A. Lam (1995), Geometric focusing of internal waves, *J. Fluid Mech.*, *300*, 1–41, doi: 10.1017/S0022112095003582.

MacCready, P. (1994), Frictional decay of abyssal boundary currents, *J. Mar. Res.*, *52*(2), 197–217, doi: 10.1357/0022240943077073.

Maiss, M., J. Ilmberger, A. Zenger, and K. O. Münnich (1994), A SF_6 tracer study of horizontal mixing in Lake Constance, *Aquatic Sciences*, *56*(4), 307–328, doi: 10.1007/BF00877179.

Matthäus, W. (1977), Mittlere vertikale Wärmeaustauschkoeffizienten in der Ostsee, *Acta Hydrophys.*, *22(2)*, 73–92.

Matthäus, W. (1990), Mixing across the primary Baltic halocline, *Beitr. Meereskd.*, *61*, 21–31.

Messias, M.-J., A. J. Watson, T. Johannessen, K. I. C. Oliver, K. A. Olsson, E. Fogelqvist, J. Olafsson, S. Bacon, J. Balle, N. Bergman, G. Budéus, M. Danielsen, J.-C. Gascard, E. Jeansson, S. R. Olafsdottir, K. Simonsen, T. Tanhua, K. Van Scoy, and J. R. Ledwell (2008), The Greenland Sea tracer experiment 1996–2002: Horizontal mixing and transport of Greenland Sea Intermediate Water, *Prog. Oceanogr.*, *78*(1), 85–105, doi: 10.1016/j.pocean.2007.06.005.

Moum, J. N., M. C. Gregg, R.-C. Lien, and M. E. Carr (1995), Comparison of turbulent kinetic energy dissipation rate estimates from two ocean microstructure profilers, *J. Atmos. Ocean. Tech.*, *12*(2), 346–366, doi: 10.1175/1520-0426(1995)012<0346:COTKED>2.0.CO;2.

Moum, J. N., D. M. Farmer, W. D. Smyth, L. Armi, and S. Vagle (2003), Structure and generation of turbulence at interfaces strained by internal solitary waves propagating shoreward over the continental shelf, *J. Phys. Oceanogr.*, *33*(10), 2093–2112, doi: 10.1175/1520-0485(2003)033<2093:SAGOTA>2.0.CO;2.

Moum, J. N., A. Perlin, K. Klymak, M. D. Levine, and T. Boyd (2004), Convectively-driven mixing in the bottom boundary layer, *J. Phys. Oceanogr.*, *34*(10), 2189–2202, doi: 10.1175/1520-0485(2004)034<42189:CDMITB>2.0.CO;2.

Mowbray, D. E., and B. S. H. Rarity (1967), A theoretical and experimental investigation of the phase configuration of internal waves of small amplitude in a density stratified liquid, *J. Fluid Mech.*, *28*, 1–16, doi: 10.1017/S0022112067001867.

Munk, W., and C. Wunsch (1998), Abyssal recipes II: Energetics of tidal and wind mixing, *Deep-Sea Res. I*, *45*(12), 1977–2010, doi: 10.1016/S0967-0637(98)00070-3.

Munk, W. H. (1966), Abyssal recipes, *Deep-Sea Res.*, *13*(4), 707–730, doi: 10.1016/0011-7471(66)90602-4.

Munk, W. H. (1981), Internal waves and small-scale processes, in *Evolution of Physical Oceanography*, edited by B. A. Warren and C. Wunsch, pp. 264–291, The MIT Press, Cambridge, MA, USA.

Nash, J. D., M. H. Alford, E. Kunze, K. Martini, and S. Kelly (2007), Hotspots of deep ocean mixing on the Oregon continental slope, *Geophys. Res. Lett.*, *34*, L01605, doi: 10.1029/2006GL028170.

Nausch, G., W. Matthäus, and R. Feistel (2003), Hydrographic and hydrochemical conditions in the Gotland Deep area between 1992 and 2003, *Oceanologia*, *45*(4), 557–569.

Nausch, G., R. Feistel, L. Umlauf, K. Nagel, and H. Siegel (2008a), Hydrographisch-chemische Zustandseinschätzung der Ostsee 2007, *Marine Science Reports*, *72*, 1–93.

Nausch, G., D. Nehring, and K. Nagel (2008b), Nutrient concentrations, trends and their relation to eutrophication, in *State and Evolution of the Baltic Sea 1952-2005*, edited by R. Feistel, G. Nausch, and N. Wasmund, pp. 337–366, John Wiley & Sons, Hoboken, New Jersey, USA.

Okubo, A. (1971), Oceanic diffusion diagrams, *Deep-Sea Res.*, *18*(8), 789–802, doi: 10.1016/0011-7471(71)90046-5.

Olsson, K., E. Jeansson, L. Anderson, B. Hansen, T. Eldevik, R. Kristiansen, M. Messias, T. Johannessen, and A. Watson (2005a), Intermediate water from the Greenland Sea in the Faroe Bank Channel: spreading of released sulphur hexafluoride, *Deep-Sea Res. II*, *52*, 279–294, doi: 10.1016/j.dsr.2004.09.009.

Olsson, K. A., E. Jeansson, T. Tanhua, and J.-C. Gascard (2005b), The East Greenland Current studied with CFCs and released sulphur hexafluoride, *J. Mar. Sys.*, *55*(1–2), 77–95, doi: 10.1016/j.jmarsys.2004.07.019.

Osborn, T. R. (1980), Estimates of the local rate of vertical diffusion from dissipation measurements, *J. Phys. Oceanogr.*, *10*(1), 83–89, doi: 10.1175/1520-0485(1980)010<0083:EOTLRO>2.0.CO;2.

Ozmidov, R. V. (1995), The role of boundary effects in the deepwater exchange in the Baltic Sea, *Oceanology*, *34*(4), 440–444.

Palmer, M. R., T. P. Rippeth, and J. H. Simpson (2008), An investigation of internal mixing in a seasonally stratified shelf sea, *J. Geophys. Res.*, *113*, C12005, doi: 10.1029/2007JC004531.

Pingree, R. D., G. T. Mardell, and A. L. New (1986), Propagation of internal tides from the upper slopes of the Bay of Biscay, *Nature*, *321*(6066), 154–158, doi: 10.1038/321154a0.

Pope, S. B. (2000), *Turbulent Flows*, 806 pp., Cambridge University Press, Cambridge, UK.

Rahm, L. (1985), On the diffusive salt flux of the Baltic proper, *Tellus A*, *37A*(1), 87–96, doi: 10.1111/j.1600-0870.1985.tb00272.x.

Raudsepp, U., D. Beletsky, and D. J. Schwab (2003), Basin-Scale Topographic Waves in the Gulf of Riga, *J. Phys. Oceanogr.*, *33*(5), 1129–1140, doi: 10.1175/1520-0485(2003)033<1129:BTWITG>2.0.CO;2.

Reissmann, J., H. Burchard, R. Feistel, E. Hagen, H.-U. Lass, V. Mohrholz, G. Nausch, L. Umlauf, and G. Wieczorek (2009), Vertical mixing in the Baltic Sea and consequences for eutrophication – A review, *Progr. Oceanogr.*, *82*(1), 47–80, doi: 10.1016/j.pocean.2007.10.004.

Reissmann, J. H. (2005), An algorithm to detect isolated anomalies in three-dimensional stratified data fields with an application to density fields from four deep basins of the Baltic Sea, *J. Geophys. Res.*, *110*, C12018, doi: 10.1029/2005JC002885.

Reynolds, O. (1883), An Experimental Investigation of the Circumstances Which Determine Whether the Motion of Water Shall Be Direct or Sinuous, and of the Law of Resistance in Parallel Channels, *Philos. T. R. Soc. Lond.*, *174*, 935–982.

Rhein, M. (1991), Ventilation rates of the Greenland and Norwegian Seas derived from distributions of the chlorofluoromethanes F11 and F12, *Deep-Sea Res. A*, *38*(4), 485–503, doi: 10.1016/0198-0149(91)90048-K.

Rhein, M., J. Fischer, W. M. Smethie, D. Smythe-Wright, R. F. Weiss, C. Mertens, D.-H. Min, U. Fleischmann, and A. Putzka (2000), Labrador sea water: Pathways, CFC inventory, and formation rates, *J. Phys. Oceanogr.*, *32*(2), 648–665, doi: 10.1175/1520-0485(2002)032<0648:LSWPCI>2.0.CO;2.

Rhein, M., M. Dengler, J. Sültenfuß, R. Hummels, S. Hüttl-Kabus, and B. Bourles (2010), Upwelling and associated heat flux in the equatorial Atlantic inferred from helium isotope disequilibrium, *J. Geophys. Res.*, *115*, C08021, doi: 10.1029/2009JC005772.

Rudnick, D. L., T. J. Boyd, R. E. Brainard, G. S. Carter, G. D. Egbert, M. C. Gregg, P. E. Holloway, J. M. Klymak, E. Kunze, C. M. Lee, M. D. Levine, D. S. Luther, J. P. Martin, M. A. Merrifield, J. N. Moum, J. D. Nash, R. Pinkel, L. Rainville, and T. B. Sanford (2003), From Tides to Mixing Along the Hawaiian Ridge, *Science*, *301*(5631), 355–357, doi: 10.1126/science.1085837.

Saylor, J. H., J. C. K. Huang, and R. O. Reid (1980), Vortex Modes in Southern Lake Michigan, *J. Phys. Oceanogr.*, *10*(11), 1814–1823, doi: 10.1175/1520-0485(1980)010<1814:VMISLM>2.0.CO;2.

Schmale, O., J. Schneider von Deimling, W. Gülzow, G. Nausch, J. J. Waniek, and G. Rehder (2010), Distribution of methane in the water column of the Baltic Sea, *Geophys. Res. Lett.*, *37*, L12604, doi: 10.1029/2010GL043115.

Schneider, B., G. Nausch, H. Kubsch, and I. Petersohn (2002), Accumulation of total CO_2 in Baltic Sea deep water and its relationship to nutrient and oxygen concentrations, *Mar. Chem.*, *77*(4), 277–291, doi: 10.1016/S0304-4203(02)00008-7.

Schneider, B., G. Nausch, and C. Pohl (2010), Mineralization of organic matter and nitrogen transformations in the Gotland Sea deep water, *Mar. Chem.*, *119*(1–4), 153–161, doi: 10.1016/j.marchem.2010.02.004.

Schott, F., and D. Quadfasel (1979), Lagrangian and Eulerian measurements of horizontal mixing in the Baltic, *Tellus*, *31*(2), 138–144, doi: 10.1111/j.2153-3490.1979.tb00890.x.

Schuert, E. A. (1970), Turbulent Diffusion in the Intermediate Waters of the North Pacific Ocean, *J. Geophys. Res.*, *75*(3), 673–682, doi: 10.1029/JC075i003p00673.

Shih, L. H., J. R. Koseff, J. H. Ferziger, and C. R. Rehmann (2000), Scaling and parameterization of stratified homogeneous turbulent shear flow, *J. Fluid Mech.*, *412*, 1–20.

Shih, L. H., J. R. Koseff, G. N. Ivey, and J. H. Ferziger (2005), Parameterization of turbulent fluxes and scales using homogenous sheared stably stratified turbulence simulations, *J. Fluid Mech.*, *525*, 193–214, doi: 10.1017/j.csr.2006.07.004.

Shilo, E., Y. Ashkenazy, A. Rimmer, S. Assouline, P. Katsafados, and Y. Mahrer (2007), Effect of wind variability on topographic waves: Lake Kinneret case, *J. Geophys. Res.*, *112*, C12024, doi: 10.1029/2007JC004336.

Shilo, E., Y. Ashkenazy, A. Rimmer, S. Assouline, and Y. Mahrer (2008), Wind Spatial Variability and Topographic Wave Frequency, *J. Phys. Oceanogr.*, *38*(9), 2085–2096, doi: 10.1175/2008JPO3886.1.

Smart, P. L., and I. M. S. Laidlaw (1977), An evaluation of some flourescent dyes for water tracing, *Water Resour. Res.*, *13*(1), 15–33, doi: 10.1029/WR013i001p00015.

Smethie, W., and R. A. Fine (2001), Rates of North Atlantic Deep Water formation calculated from chlorofluorocarbon inventories, *Deep-Sea Res. I*, *48*(1), 189–215, doi: 10.1016/S0967-0637(00)00048-0.

Smyth, W. D., and J. N. Moum (2000a), Length scales of turbulence in stably stratified mixing layers, *Phys. Fluids*, *12*(6), 1327–1342, doi: 10.1063/1.870385.

Smyth, W. D., and J. N. Moum (2000b), Anisotropy of turbulence in stably stratified mixing layers, *Phys. Fluids*, *12*(6), 1343–1362, doi: 10.1063/1.870386.

Stigebrandt, A. (1987), A model for the vertical circulation of the Baltic deep water, *J. Phys. Oceanogr.*, *17*(10), 1772–1785, doi: 10.1175/1520-0485(1987)017<1772:AMFTVC>2.0.CO;2.

Stocker, T., and K. Hutter (1992), *Topographic Waves in Channels and Lakes on the f-Plane.*, *Lecture Notes on Coastal and Estuarine Studies*, vol. 21, 173 pp., Springer.

Strady, E., C. Pohl, E. V. Yakushev, S. Krüger, and U. Hennings (2008), PUMP-CTD-System for trace metal sampling with a high vertical resolution. A test in the Gotland Basin, Baltic Sea, *Chemosphere*, *70*(7), 1309–1319, doi: 10.1016/j.chemosphere.2007.07.051.

Tanhua, T., K. A. Olsson, and E. Fogelqvist (2004), A first study of SF_6 as a transient tracer in the Southern Ocean, *Deep-Sea Res. II*, *51*(22–24), 2683–2699, doi: 10.1016/j.dsr2.2001.02.001.

Tanhua, T., D. W. Waugh, and D. W. R. Wallace (2008), Use of SF_6 to estimate anthropogenic CO_2 in the upper ocean, *J. Geophys. Res.*, *113*, C04037, doi: 10.1029/2007JC004416.

Thorpe, S. A. (2005), *The Turbulent Ocean*, 439 pp., Cambridge University Press, Cambridge, UK.

Thorpe, S. A., T. R. Osborn, J. F. E. Jackson, A. J. Hall, and R. G. Lueck (2003), Measurements of turbulence in the upper-ocean mixing layer using autosub, *J. Phys. Oceanogr.*, *33*(1), 122–145, doi: 10.1175/1520-0485(2003)033<0122:MOTITU>2.0.CO;2.

Umlauf, L., and L. Arneborg (2009a), Dynamics of rotating shallow gravity currents passing through a channel. Part I: Observation of transverse structure, *J. Phys. Oceanogr.*, *39*(10), 2385–2401, doi: 10.1175/2009JPO4159.1.

Umlauf, L., and L. Arneborg (2009b), Dynamics of rotating shallow gravity currents passing through a channel. Part II: Analysis, *J. Phys. Oceanogr.*, *39*(10), 2402–2416, doi: 10.1175/2009JPO4164.1.

Umlauf, L., and H. Burchard (2011), Diapycnal transport and mixing efficiency in stratified boundary layers near sloping topography, *J. Phys. Oceanogr.*, *41*(2), 329–345, doi: 10.1175/2010JPO4438.1.

Umlauf, L., and U. Lemmin (2005), Interbasin exchange and mixing in the hypolimnion of a large lake: The role of long internal waves, *Limnol. Oceanogr.*, *50*(5), 1601–1611, doi: 10.4319/lo.2005.50.5.1601.

Umlauf, L., T. Tanhua, J. J. Waniek, O. Schmale, P. Holtermann, and G. Rehder (2008), Hunting a new tracer, *EOS, Transactions American Geophysical Union*, *89*(43), 419–419.

Vahtera, E., D. J. Conley, B. Gustafsson, H. Kuosa, H. Pitkänen, O. P. Savchuk, T. Tamminen, M. Viitasalo, M. Voss, N. Wasmund, and F. Wulff (2007), Internal ecosystem feedbacks enhance nitrogen-fixing cyanobacteria blooms and complicate management in the Baltic Sea, *AMBIO*, *36*(2), 186–194, doi: 10.1579/0044-7447(2007)36[186:IEFENC]2.0.CO;2.

van der Lee, E. M., and L. Umlauf (2011), Internal-wave mixing in the Baltic Sea: Near-inertial waves in the absence of tides, *J. Geophys. Res.*, *116*, C10016, doi: 10.1029/2011JC007072.

Vasholz, D. P., and L. J. Crawford (1985), Dye dispersion in the seasonal thermocline, *J. Phys. Oceanogr.*, *15*(6), 695–712, doi: 10.1175/1520-0485(1985)015<0695:DDITST>2.0.CO;2.

Victor, D. G., and G. J. MacDonald (1999), A model for estimating future emissions of sulfur hexafluoride and perfluorocarbons, *Climatic Change*, *42*(4), 633–662, doi: 10.1023/A:1005427905524.

Wåhlin, A. K., and C. Cenedese (2006), How entraining density currents influence the stratification in a one-dimensional ocean basin, *Deep-Sea Res. II*, *53*(1–2), 172–193, doi: 10.1016/j.dsr2.2005.10.019.

Wanninkhof, R. (1992), Relationship between wind-speed and gas-exchange over the ocean, *J. Geophys. Res.*, *97*(C5), 7373–7382, doi: 10.1029/92JC00188.

Wasmund, N., M. Voss, and K. Lochte (2001), Evidence of nitrogen fixation by non-heterocystous cyanobacteria in the Baltic Sea and re-calculation of a budget of nitrogen fixation, *Mar. Ecol. Prog. Ser.*, *214*, 1–14, doi: 10.3354/meps214001.

Watson, A. J., and J. R. Ledwell (2000), Oceanographic tracer release experiments using sulphur hexafluoride, *J. Geophys. Res.*, *105*(C6), 14325–14337, doi: 10.1029/1999JC900272.

Weatherly, G. L., and P. J. Martin (1978), On the structure and dynamics of the oceanic bottom boundary layer, *J. Phys. Oceanogr.*, *8*(4), 557–570, doi: 10.1175/1520-0485(1978)008<0557:OTSADO>2.0.CO;2.

Wieczorek, G., E. Hagen, and L. Umlauf (2008), Eastern Gotland Basin case study of thermal variability in the wake of deep water intrusions, *J. Mar. Sys.*, *74*(S1), S65–S97, doi: 10.1016/j.jmarsys.2008.07.008.

Winters, K. B., and E. A. D'Asaro (1996), Diascalar flux and the rate of fluid mixing, *J. Fluid Mech.*, *317*, 179–193, doi: 10.1017/S0022112096000717.

Winters, K. B., P. N. Lombard, J. J. Riley, and E. A. D'Asaro (1995), Available potential energy and mixing in density-stratified fluids, *J. Fluid Mech.*, *289*, 115–128, doi: 10.1017/S002211209500125X.

Wisegarver, D. P., and R. H. Gammon (1988), A New Transient Tracer: Measured Vertical-distribution of CCl_2FCClF_2 (F-113) in the North Pacific Subarctic Gyre, *Geophys. Res. Lett.*, *15*(2), 188–191, doi: 10.1029/GL015i002p00188.

Woods, J. D. (1968), Wave-induced shear instability in the summer thermocline, *J. Fluid Mech.*, *32*, 791–800.

Wüest, A., and A. Lorke (2003), Small-scale hydrodynamics in lakes, *Annu. Rev. Fluid Mech.*, *35*, 373–412, doi: 10.1146/annurev.fluid.35.101101.161220.

Wüest, A., G. Piepke, and D. Van Senden (2000), Turbulent kinetic energy balance as a tool for estimating vertical diffusivity in wind-forced stratified waters, *Limnol. Oceanogr.*, *45*(6), 1388–1400, doi: 10.4319/lo.2000.45.6.1388.

Wunsch, C., and R. Ferrari (2004), Vertical mixing, energy, and the general circulation of the oceans, *Annu. Rev. Fluid Mech.*, *36*, 281–314, doi: 10.1146/annurev.fluid.36.050802.122121.

Wunsch, C., and R. Hendry (1972), Array measurements of the bottom boundary layer and the internal wave field on the continental slope, *Geophys. Astro. Fluid*, *4*(1), 101–145, doi: 10.1080/03091927208236092.

Zhurbas, V. M., and V. T. Paka (1997), Mesoscale thermohaline variability in the Eastern Gotland Basin following the 1993 major Baltic inflow, *J. Geophys. Res.*, *102*(C9), 20917–20926, doi: 10.1029/97JC00443.